Search for VHE γ-ray Emission from the Direction of the two Millisecond Pulsars PSR J0437−4715 and PSR J1824−2452 and the composite Supernova Remnant Kes 75 with H.E.S.S.

D I S S E R T A T I O N

zur Erlangung des akademischen Grades

Dr. rer. nat.
im Fach Physik

eingereicht an der
Mathematisch-Naturwissenschaftlichen Fakultät I
Humboldt-Universität zu Berlin

von
Dipl.-Phys. Matthias Füßling
Berlin

Präsident der Humboldt-Universität zu Berlin:
Prof. Dr. Jan-Hendrik Olbertz

Dekan der Mathematisch-Naturwissenschaftlichen Fakultät I:
Prof. Dr. Stefan Hecht

Gutachter:
1. Prof. Dr. Thomas Lohse
2. Prof. Dr. Christopher van Eldik
3. Prof. Dr. Alexander Kappes

eingereicht am: 09. August 2012
Tag der mündlichen Prüfung: 12. Dezember 2012

Abstract

This work reports on the search for pulsed and steady very-high energy (VHE) γ-ray emission in the energy range extending from 100 GeV up to 100 TeV from the direction of three pulsars with the High Energy Stereoscopic System (H.E.S.S.).

Pulsars are highly magnetized neutron stars, which rotate with spin periods ranging from milliseconds to seconds. These objects are known sources of relativistic particles and non-thermal radiation, which is produced both near the pulsar within its magnetosphere and farther out in the extended pulsar wind nebula (PWN) region. The non-thermal radiation from within the magnetosphere is emitted in a beam of radiation, which can be observed as a characteristic pattern of short and periodic pulses due to the pulsar's rotation (lighthouse effect). Pulsed γ-ray radiation with energies beyond 100 GeV was found thus far only for the young and energetic Crab pulsar. Various models have been put forward to explain the acceleration and radiation mechanisms in the pulsar's magnetosphere. Some of them predict that millisecond pulsars are able to emit pulsed γ-ray radiation with energies above 100 GeV. PWNe constitute by now the most abundant class of Galactic VHE γ-ray emitters. The radiating nebulae often extend over a large region. For only a handful of PWNe, which are powered by very young and energetic pulsars, the VHE γ-ray emission region appears point-like. A special class among them are PWNe associated with composite supernova remnants (SNRs) where the PWN is centered in an expanding SNR shell. A clear identification of the PWN or SNR shell as the source of the VHE γ-ray emission is in these cases difficult.

In the first part of this thesis, the results on the search for pulsed and steady VHE γ-ray emission from the two millisecond pulsars, PSR J0437−4715 and PSR J1824−2452, are presented. Parts of the observations were conducted in a special trigger setup (the topological trigger with convergent pointing) to reduce the energy threshold of the instrument. No signal of pulsed or steady emission is found and upper limits on the pulsed and steady γ-ray flux are derived. The upper limits on the pulsed γ-ray flux are compared to existing model predictions and, in the case of PSR J1824−2452, allow the range of possible viewing geometries in some models to be constrained.

In the second part of this work, results on the search for pulsed and steady VHE γ-ray emission from the direction of the composite SNR Kes 75 are presented. The PWN in the center of Kes 75 is powered by a very young and powerful pulsar, PSR J1846−0258, that has an exceptionally high magnetic field. While no hint for pulsed emission is found, steady VHE γ-ray emission is detected with a statistical significance of 10 σ from a point-like source. The VHE γ-ray emission is spatially coincident with the PWN and the SNR shell. Both are discussed as a possible origin for the observed emission. The pulsar of Kes 75 would be the youngest pulsar known to date to power a VHE PWN.

Kurzfassung

Diese Arbeit berichtet über die Suche nach gepulster und ungepulster hochenergetischer (VHE) Gammastrahlung mit dem High Energy Stereoscopic System (H.E.S.S.) im Energiebereich von 100 GeV bis 100 TeV aus der Richtung von drei Pulsaren.

Pulsare sind stark magnetisierte Neutronensterne, die mit Spinperioden im Bereich von Millisekunden bis Sekunden rotieren. Diese Objekte sind bekannte Quellen relativistischer Teilchen und nichtthermischer Strahlung, die sowohl in der Nähe des Pulsars in seiner Magnetosphäre als auch weiter entfernt in der ausgedehnten Region des Pulsarwindnebels (PWNs) entsteht. Die nichtthermische Strahlung aus der Magnetosphäre wird als Strahl ausgesandt, der durch die Rotation des Pulsars ein charakteristisches Muster von kurzen, periodischen Pulsen erzeugt (Leuchtturmeffekt). Gepulste Gammastrahlung mit Energien groesser als 100 GeV wurde bisher nur fuer den jungen und energetischen Krebspulsar gefunden. Diverse Modelle wurden vorgeschlagen, um die Mechanismen der Teilchenbeschleunigung und Strahlung in der Pulsarmagnetosphäre zu erklären. Einige von ihnen sagen voraus, dass Millisekundenpulsare dazu in der Lage sind, gepulste Gammastrahlung mit Energien von mehr als 100 GeV zu emittieren. PWN stellen inzwischen die zahlreichste Klasse galaktischer Quellen von VHE Gammastrahlung dar. Der abstrahlende Nebel erstreckt sich oft über eine grosse Region. Nur für eine Handvoll von PWN, die von sehr jungen und energetischen Pulsaren angetrieben werden, erscheint die Emissionsregion der VHE Gammastrahlung punktförmig. Eine besondere Gruppe unter ihnen sind die zusammengesetzten Supernovaüberreste (SNR), bei denen sich ein PWN im Zentrum einer expandierenden Schale eines SNR befindet. Eine eindeutige Identifizierung des PWN oder der Schale des SNR als Quelle der VHE Gammastrahlung ist in diesen Fällen schwierig.

Die Resultate der Suche nach gepulster und ungepulster VHE Gammastrahlung von zwei Millisekundenpulsaren, PSR J0437−4715 und PSR J1824−2452, werden im ersten Teil dieser Arbeit vorgestellt. Teile der Beobachtungen wurden in einer speziellen Triggerkonfiguration (dem Topologischen Trigger mit konvergenter Ausrichtung) durchgeführt, um die Energieschwelle des Instruments zu senken. Kein Hinweis auf gepulste oder ungepulste Emission wurde gefunden und obere Grenzen auf den gepulsten und ungepulsten Fluss wurden bestimmt. Die oberen Grenzen auf den gepulsten Fluss werden mit bestehenden Modellvorhersagen verglichen und erlauben für PSR J1824−2452 den Bereich möglicher Geometrien in einigen Modellen einzuschränken.

Die Resultate der Suche nach gepulster und ungepulster VHE Gammastrahlung aus der Richtung des zusammengesetzten SNR Kes 75 werden im zweiten Teil dieser Arbeit präsentiert. Der PWN im Zentrum von Kes 75 wird von einem sehr jungen und energiereichen Pulsar, PSR J1846−0258, angetrieben, der ein aussergewöhnlich starkes Magnetfeld besitzt. Während kein Hinweis auf gepulste Strahlung gefunden wurde, kon-

nte ungepulste Emission von VHE Gammastrahlung von einer Punktquelle mit einer statistischen Signifikanz von 10 σ nachgewiesen werden. Die VHE Gammastrahlung ist räumlich koinzident mit dem PWN und mit der SNR Schale. Beide werden als mögliche Quelle für die beobachtete Emission diskutiert. Der Pulsar von Kes 75 wäre der jüngste bisher bekannte Pulsar, der einen Pulsarwindnebel antreibt.

Contents

List of Figures

List of Tables

Abbreviations

CM	Convergent observation mode
CMB	Cosmic microwave background radiation
CR	Curvature radiation
CSM	Circumstellar matter
eV	Electronvolt, 1.602×10^{-19} J
GeV	Gigaelectronvolt, 10^9 eV
GC	Globular cluster
HE	High energy range, 30 MeV$<E<$100 GeV
IC	Inverse Compton scattering
IR	Infrared
ISM	Insterstellar matter
keV	Kiloelectronvolt, 10^3 eV
LC	Light cylinder
NS	Neutron star
MeV	Megaelectronvolt, 10^6 eV
MSP	Millisecond pulsar
OG	Outer gap
PC	Polar cap
PSPC	Pair-starved polar cap
PFF	Pair formation front
PWN	Pulsar wind nebula
SCLF	Spage-charge limited flow
SM	Standard observation mode
SN	Supernova
SNR	Supernova remnant
SR	Synchrotron radiation
SSC	Synchrotron self-Compton
TeV	Teraelectronvolt, 10^{12} eV
TPC	Two-pole caustic
TT	Convergent observation mode with a topological trigger
VHE	Very-high energy range, 100 GeV$<E<$100 TeV

1 Introduction

The way that we look at and understand our universe has changed dramatically within the last hundred years. For the longest part of human history, our knowledge of the universe has been shaped primarily by observations of the night sky with the bare human eye and aiding instruments in the optical waveband, with wavelengths ranging from 300 nm to 700 nm and photon energies in the order of eV. This part of the electromagnetic spectrum is dominated by thermal radiation of stars. First references to phenomena that cannot be explained by thermally emitting stars have been made already during the early epochs of optical astronomy. One of these phenomena was that of the so-called guest stars [1], referring to stars that are visible on the firmament for only a short period of time and that are now known to be connected to the supernova explosion of stars at the end of their lifetime. Within the last decades, the study of the leftovers of such catastrophic events, i.e. supernova remnant (SNR) shells as well as pulsars and pulsar wind nebulae (PWNe), became one of the most important research topics in astrophysics, both from the theoretical and observational point of view. These objects are able to accelerate particles up to energies of at least 10^{15} eV and are sources of non-thermal radiation emitted over the entire electromagnetic spectrum up to photon energies of at least 10^{12} eV.

A view of the non-thermal universe has become accessible within the last century with various developments of technologies and techniques of astronomical observations. The available wavelength range now spans more than 20 orders of magnitude in wavelength and reaches from the lowest-frequency radio waveband, corresponding to a wavelength of about 100 cm, through the millimeter, infrared, optical, ultraviolet and X-ray waveband up to the waveband of γ-ray radiation with wavelengths smaller than 10^{-13} cm. The γ-ray waveband represents the most energetic part of the electromagnetic spectrum, starting at an energy of about 100 keV, and is conventionally further subdivided into the high-energy (HE, 30 MeV$<E<$100 GeV) and the very-high-energy (VHE, 100 GeV$<E<$100 TeV) γ-ray range. Each spectral range provides specific information about phenomena in the universe that are not or not entirely accessible within the other spectral ranges. While the universe is largely transparent for γ-ray photons of such high energies [2], the Earth's atmosphere is not and the incident primary γ-ray photons are fully absorbed in a cascade of secondary particles and electromagnetic radiation, a so-called extensive air shower. Thus, two general fields of detection techniques for γ-ray photons have been developed: direct detection of the photons with satellite-based observatories as well as indirect detection of the photons with ground-based instruments.

[1] First recordings of such events by Chinese astronomers date back almost 2000 years.

[2] Absorption of the high-energy photons on extragalactic background light limits the distance up to which astrophysical sources can be seen.

1 Introduction

The current space-borne γ-ray observatories *AGILE* and *Fermi*, launched in 2007 and 2008, use pair-conversion instruments to detect photons in the HE range. The effective detection area of such satellites is limited to some m^2 due to size and weight limitations. As the number of emitted photons from non-thermal astrophysical sources typically decreases rapidly with increasing energy, large detection areas in the order of $\sim 10^5\,\mathrm{m}^2$ are needed to detect a sufficient number of photons with energies beyond some tens of GeV in a reasonable interval of time. In the VHE range, indirect detection techniques of ground-based instruments are used that use the Earth's atmosphere as an integral part of the detector. The breakthrough for VHE γ-ray astronomy came with the development of the ground-based Imaging Atmospheric Cherenkov Technique (IACT). This technique uses imaging telescopes to record the Cherenkov light which is emitted by the photon-induced extensive air showers. From the recorded shower images, the properties of the incident photon such as its energy and direction can be reconstructed. Within the last decade, VHE γ-ray astronomy has taken its place alongside the radio, optical and X-ray domains of astronomy. About 100 VHE γ-ray sources are now known and a large number of them has been discovered with the High Energy Stereoscopic System (H.E.S.S.), an array of four Imaging Atmospheric Cherenkov Telescopes with large 12 m-diameter reflectors and 5° wide-field cameras located in the Khomas Highland of Namibia.

Most of the galactic VHE γ-ray sources discovered by H.E.S.S. are connected to the remains of supernovae, i.e. SNR shells and PWNe. Pulsars are neutron stars which rotate with periods ranging from several milliseconds to seconds and are able to generate strong magnetic fields in the order of $10^{10}\,\mathrm{G}$. In the rotating pulsar's magnetosphere, regions with strong electric fields form where particles are accelerated to relativistic energies and beamed non-thermal radiation originates that can be observed with a characteristic pattern of periodic pulses due to the pulsar's rotation (lighthouse effect). Various competing models exist that try to explain the details of the formation of the accelerating region as well as the acceleration and radiation mechanisms. From model predictions, it is expected that some of the pulsars have their peak luminosities of pulsed emission in the beyond-GeV energy range. Observations with the recently launched *Fermi* satellite showed that pulsars are indeed γ-ray emitters up to at least several GeV. A significant fraction of them are millisecond pulsars, i.e. very old ($10^6 - 10^9$ years) pulsars with spin periods in the order of milliseconds. Despite various efforts, pulsed VHE γ-ray radiation from pulsars has not been detected with ground-based IACT experiments with one remarkable exception, the young (1000 years) and energetic Crab pulsar as seen by Magic and VERITAS up to at least 400 GeV [3]. Some models predict that millisecond pulsars, are able to emit pulsed γ-ray radiation beyond 100 GeV, a range accessible by current IACTs such as H.E.S.S.

A significant fraction of the accelerated particles leaves the pulsar's magnetosphere as a relativistic wind that, in interaction with the ambient medium, forms a stationary shock front where the ram pressure of the wind is balanced by the pressure of the sur-

[3] Unfortunately, the Crab pulsar is located in the northern hemisphere and cannot be observed with H.E.S.S. at low zenith angles, leading to a comparatively high energy threshold for the observations.

rounding medium and particles are accelerated to at least TeV energies. The resulting region of a hot and magnetized plasma, the pulsar wind nebula, is observable throughout the electromagnetic spectrum from radio to TeV energies. Pulsar wind nebulae form by now the most abundant class of galactic VHE γ-ray emitting sources. The morphology and spectrum of the steady VHE γ-ray emission allows to estimate important physical properties of the nebula region and the powering pulsar. The large population of PWNe seen at VHE and X-ray energies allowed for the first correlation studies connecting the observed emission with properties of the pulsar.

This thesis reports on the search for steady and pulsed VHE γ-ray emission from the direction of three pulsars, the millisecond pulsars PSR J1824−2452 and PSR J0437−4715 as well as the very young and energetic pulsar PSR J1846−0258, located in the center of the composite SNR Kes 75, using data taken with the H.E.S.S. experiment. This work is structured as follows:

- Chapter 2 gives an overview of the physics of pulsars and PWNe. The structure of neutron stars and the properties of pulsars and millisecond pulsars are presented together with the main models for particle acceleration and production of pulsed γ-ray emission within the pulsar's magnetosphere. In addition, the structure and evolution of pulsar wind nebulae are described and the models for acceleration of particles and production of non-thermal VHE γ-ray emission within the nebula region are briefly discussed. The chapter concludes with a short description of recent studies correlating the X-ray and VHE γ-ray emission of PWNe.
- Chapter 3 describes the principles of the Imaging Atmospheric Cherenkov Technique and gives an overview of the H.E.S.S. experiment. The standard H.E.S.S. data analysis to search for steady VHE γ-ray emission and the timing analysis to search for pulsed VHE γ-ray emission are summarized. Furthermore, a special trigger setup to lower the energy threshold of the H.E.S.S. instrument, the topological trigger with convergent pointing, is presented.
- Chapter 4 reports on the search for steady and pulsed VHE γ-ray emission from the direction of the millisecond pulsars PSR J1824−2452 and PSR J0437−4715.
- Chapter5 reports on the search for steady and pulsed VHE γ-ray emission from the direction of the composite SNR Kes 75 and its pulsar PSR J1846−0258.

2 Pulsars and Pulsar Wind Nebulae

One of the most fundamental research objects in astrophysics are pulsars and their winds of highly relativistic particles. These astrophysical phenomena allow the study of acceleration and radiation mechanisms in the vicinity of these compact objects where matter is exposed to ultra-strong electromagnetic fields. Pulsars, created in supernova explosions of massive stars as rapidly spinning neutron stars, induce high potentials in their strong magnetosphere where particle acceleration takes place. These objects are known to produce beams of radiation which are visible with a distinct pattern of short and periodic pulses that are created when the beams sweep the line of sight to the observer, analogous to the effect of a lighthouse beam. A large fraction of the pulsar's rotational energy leaves the pulsar magnetosphere as a magnetized wind of highly relativistic particles. The pulsar wind is confined by its environment and a wind termination shock front is formed where the wind particles are accelerated and isotropized. An extended region of a hot relativistic gas results beyond the termination shock, known as the pulsar wind nebula (PWN), which is the source of steady emission throughout the electromagnetic spectrum.

In this chapter, a review of the physics of pulsars and pulsar wind nebulae is given. First, the general properties of pulsars are presented, including on overview on the structure of neutron stars and on the main models for production of pulsed magnetospheric VHE γ-ray emission. The second part of this chapter is dedicated to the structure and evolution of pulsar wind nebulae together with the main models for production of VHE γ-rays. Each part concludes with a short census on the observational status of the field.

2.1 Pulsars

Pulsars were discovered serendipitously in 1967 by Bell and Hewish [Hewish et al., 1968] at the Mullard Radio Astronomy Observatory in Cambridge during scintillation measurements of quasi stellar radio sources. A pulsed signal with an extremely stable periodicity of 1.337 s emerged in the data from an object later named PSR B1919+21. Soon after the discovery, Gold [Gold, 1968] and Pacini [Pacini, 1968] identified these objects as rapidly rotating neutron stars whose existence as leftovers from supernova explosions had been predicted already in 1934 by Baade and Zwicky [Baade and Zwicky, 1934]. Gold and Pacini suggested that the observable emission stems from charged particles that have been accelerated to relativistic energies at the expense of the rotational energy of the neutron star causing the neutron star to slow down. Further discoveries at radio energies in 1968 of a pulsar of 33 ms period in the Crab nebula [Staelin and Reifenstein, 1968] and a pulsar of 89 ms period in the core of the Vela supernova remnant [Large et al.,

1968] established the pulsar phenomenon and its connection with supernovae.

2.1.1 Neutron Stars

Neutron stars are the end product of the stellar evolution when the core of the massive progenitor star ($> 8\,M_\odot$) collapses gravitationally. The core stabilizes itself as a neutron star when the star's interior supports the star from further collapse into a black hole by nuclear forces and neutron degeneracy pressure. These compact stellar remnants have a radius of about $\sim 10\,\mathrm{km}$, smaller by a factor of 10^5 of that of the sun and masses in the range of about 1 to $3\,M_\odot$. Assuming a canonical value for the neutron star mass of $1.4\,M_\odot$, neutron stars have a resulting overall density of about $10^{15}\,\mathrm{g\,cm^{-3}}$ (the density of the sun is $1.4\,\mathrm{g\,cm^{-3}}$). For such high densities, the nuclear matter in the neutron star's interior is believed to consist largely of a degenerate gas of neutrons, hence the name neutron star.

The structure of a neutron star is, however, uncertain and various theoretical models exist that attempt to describe the equation of state of ultra-dense matter. Figure 2.1 shows the structure of a neutron star for different configurations of the neutron star matter. The standard picture for the structure of a neutron star (labeled 'traditional neutron star' in Fig. 2.1) consists of five major regions which, going from the outer to the inner layer, are:

- A gaseous atmosphere of typically hydrogen or helium which is less than 0.1 m thick and is with typical densities in the range of $10^{-3}\,\mathrm{g\,cm^{-3}}$ to $10^{4}\,\mathrm{g\,cm^{-3}}$ of negligible amount of mass.

- An envelope of a thin and electrically conductive outer layer, about 300 m thick, containing nuclei in a rigid lattice and a sea of free and relativistic degenerate electrons. The density in this region is less than about $10^{6}\,\mathrm{g\,cm^{-3}}$. The chemical composition of the envelope layer is largely unknown, but is believed to mainly consist of heavy nuclei such as ^{56}Fe.

- A crust, about 600 m thick, which consists of a lattice of neutron-rich nuclei and a sea of degenerate neutrons and relativistic degenerate electrons. The mass of the crust is about 1% to 2% of the total neutron star mass. The density varies within the crust from about $10^{6}\,\mathrm{g\,cm^{-3}}$ in the outer crust layer to about $10^{14}\,\mathrm{g\,cm^{-3}}$ near the interface of the crust to the neutron star core. When the density and pressure become sufficiently large within the crust, the relativistic electrons penetrate the nuclei and recombine with protons to form neutrons in inverse beta decay. Thus, the dominant nuclei vary with density, ranging from ^{56}Fe in the outer layer to heavy neutron-rich nuclei in the inner layer of the crust. At densities above the neutron drip density of about $4 \times 10^{11}\,\mathrm{g\,cm^{-3}}$, neutrons escape the nuclei and form a superfluid of neutrons.

- A core with a density greater than $10^{14}\,\mathrm{g\,cm^{-3}}$ and which comprises up to 99% of the neutron star's mass. The outer core layer consists mainly of a superfluid

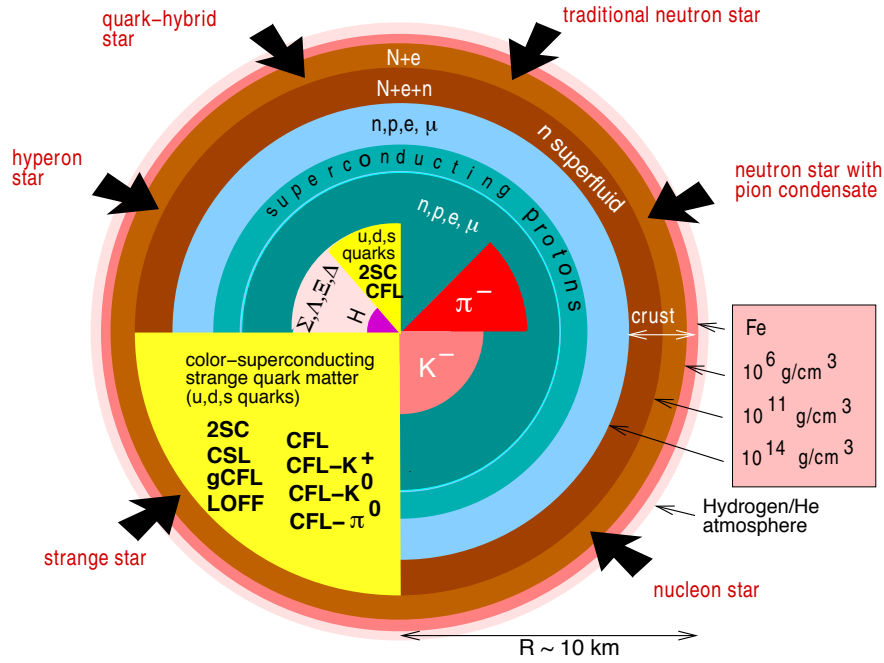

Figure 2.1 Schematic view of competing models for the structure of neutron stars. More details on the traditional neutron star model are given in the text. Taken from Weber [2005].

of neutrons with a small concentration of protons and electrons. The composition of matter in the inner core of the neutron star is of uncertain nature. As the central density may become larger than several times the nuclear matter density of $4 \times 10^{14}\,\mathrm{g\,cm^{-3}}$, the matter may consist of free quarks or be in some exotic state.

More details on the formation of neutron stars can be found in Lattimer and Prakash [2004] and Weber [2005].

While a large fraction of energy is carried away by neutrinos and ejected matter during the supernova explosion, the magnetic flux and angular momentum of the progenitor star are largely conserved. Thus, high magnetic fields at the surface of the neutron star of typically $10^{12}\,\mathrm{G}$ and short rotation periods of a fraction of a second result for neutron stars.

2.1.2 General Properties

A simplified description of the main properties of pulsars that allows to derive important physical parameters used throughout the thesis is that of a rotating magnetic dipole [Ostriker and Gunn, 1969]. A pulsar of period P rotates with an angular frequency $\Omega = 2\pi/P$. While the period increases with a rate $\dot{P}$, a fraction of the rotational kinetic

energy $E_{\rm rot} = \frac{1}{2} I \Omega^2$ of the pulsar is transferred to observable emission. Here, I denotes the stellar moment of inertia $I \approx (2/5) M R^2$ of the pulsar and has a typical value of $10^{45}\,\mathrm{g\,cm^2}$ for a pulsar with a canonical radius $R_{\rm NS} = 10\,\mathrm{km}$ and mass $M = 1.4\,\mathrm{M}_\odot$. The current loss of rotational kinetic energy $\dot{E} = \mathrm{d}E_{\rm rot}/\mathrm{d}t$, dubbed spin-down power of a pulsar, is related to the pulsar's period and period derivative via

$$\dot{E} = I \Omega \dot{\Omega} = -(2\pi)^2 I \left(\frac{\dot{P}}{P^3} \right). \tag{2.1}$$

The most energetic pulsars have a spin-down power of about $10^{35-38}\,\mathrm{erg\,s^{-1}}$. It is found that the observed luminosity of pulsed emission from pulsars $L_{\rm obs}$ scales with the pulsar's spin-down power $\dot{E}$, but accounts only for a fraction of the current spin-down power of the pulsar. Typical conversion efficiencies $\eta = L_{\rm obs}/\dot{E}$ for pulsed emission are in the range of 10^{-7} to 10^{-5} in the radio and optical waveband and increase to $10^{-2} - 10^{-1}$ for the high-energy γ-ray waveband. A significant fraction of the pulsar's spin-down power $\dot{E}$ is not converted to pulsed emission, but is carried away by a wind of relativistic charged particles and magnetic field and will be discussed in more detail in Section 2.2.

The total rotational kinetic energy released by the pulsar since its birth with a birth period P_0 and birth angular frequency Ω_0 is

$$E_{\rm rot,tot} = \frac{1}{2} I \left(\Omega_0^2 - \Omega^2 \right) = \frac{(2\pi)^2}{2} I \left(\frac{1}{P_0^2} - \frac{1}{P^2} \right). \tag{2.2}$$

Typical values for the rotational kinetic energy which has been released over the pulsar's lifetime are in the order of $10^{49}\,\mathrm{erg}$ [Gaensler and Slane, 2006].

In the canonical model for magnetic dipole radiation, the pulsar spins down due to braking by its magnetic field with $\dot{\Omega} = -k\Omega^n$ where n is the magnetic braking index. The value of n depends on the slow-down mechanism and is $n = 3$ for pure magnetic dipole radiation. The braking index has been measured for a few pulsars and the values range from 1.4 to 2.9 Livingstone et al. [2006], suggesting that the magnetic braking is not pure dipolar and/or that n evolves with time (see also Livingstone et al. [2007] for a review).

Under the assumption of a constant magnetic braking index, the pulsar's spin-down relation $\dot{\Omega} = -k\Omega^n$ can be used to estimate the age of the pulsar τ. The time span required to spin down from the birth spin period P_0 to the current value P is

$$\tau = \frac{P}{(n-1)\dot{P}} \left(1 - \frac{P_0}{P}^{(n-1)} \right), \tag{2.3}$$

where $n \neq 1$ is assumed. It is conventional to derive a characteristic age $\tau_{\rm c}$ of the pulsar by setting $n = 3$ and $P_0 \ll P$ that leads to

$$\tau_{\rm c} = \frac{P}{2\dot{P}}. \tag{2.4}$$

The model of a rotating magnetic dipole allows to estimate the strength of the magnetic field within the pulsar's magnetosphere. The magnetosphere can be divided into the inner magnetosphere, which co-rotates with the pulsar and extends up to the so-called light cylinder $R_{\rm LC}$, and the outer magnetosphere beyond the light cylinder. The light cylinder thereby denotes the radius within the pulsar's magnetosphere where the velocity of the co-rotating particles reaches the speed of light and can be written as

$$R_{\rm LC} = \frac{c\,P}{2\pi} \approx 5 \times 10^4 \left(\frac{P}{1\,\rm s}\right) \rm km. \tag{2.5}$$

Millisecond pulsars, i.e. pulsars that rotate with spin periods of $P \sim 10\,\rm ms$ thus have magnetospheres that are much more compact than those of normal pulsars. While the dipole radiation depends on the assumed inclination angle α between the pulsar's rotation axis and the magnetic axis, it is conventional to assume that the pulsar is an orthogonal rotator, i.e. $\alpha = 90°$. In this case, the magnetic field strength at the neutron star surface, i.e. at the typical neutron star radius of $R_{\rm NS} = 10\,\rm km$, is

$$B_{\rm S} = 3.2 \times 10^{19} \sqrt{P\dot{P}}\,\rm G. \tag{2.6}$$

and the magnetic field strength at the light cylinder is

$$B_{\rm LC} = B_{\rm S} \left(\frac{R_{\rm NS}}{R_{\rm LC}}\right)^3. \tag{2.7}$$

2.1.3 Pulsar Population

About 40 years after the discovery of the pulsar phenomenon more than 2000 rotation-powered pulsars are known from various radio surveys [Manchester et al., 2005].

The population of radio pulsars with known period P and period derivative $\dot{P}$ is illustrated in Fig. 2.2 along with lines of constant characteristic age, surface dipole magnetic field strength and spin-down power. The majority of the pulsars are found with pulse periods between 0.1 s and several seconds which increase at rates $10^{-17}\,\rm s\,s^{-1} < \dot{P} < 10^{-13}\,\rm s\,s^{-1}$, the island of the so-called *normal* or *canonical* pulsars. The most energetic canonical pulsars ($\dot{E} > 10^{36}\,\rm erg\,s^{-1}$) are also relatively young ($\tau_{\rm c} < 10^5\,\rm years$).

A few rotation-powered pulsars, the so-called high-B pulsars (see also Ng and Kaspi [2011]), have magnetic fields larger than $10^{13}\,\rm G$ and are in the transitional regime to magnetars, transient astrophysical sources that are believed to be slowly-rotating neutron stars and whose outbursts are powered by the decay of their ultra-strong magnetic fields of $> 10^{14}\,\rm G$ [Duncan and Thompson, 1992].

A second island in the lower left corner of the diagram is populated by the millisecond pulsars (MSPs) with short ($P < 30\,\rm ms$) [1] and highly stable ($\dot{P} \leq 10^{-17}\,\rm s/s$) periods. Currently, more than 200 MSPs are known at radio frequencies [Manchester et al., 2005] among them the most rapidly rotating neutron star with a spin period of $P \sim 1.396\,\rm ms$,

[1] The limit to distinguish the millisecond pulsars from the canonical pulsars is rather arbitrary. The limit applied here excludes the young and energetic Crab pulsar ($P = 33\,\rm ms$) from the MSP population.

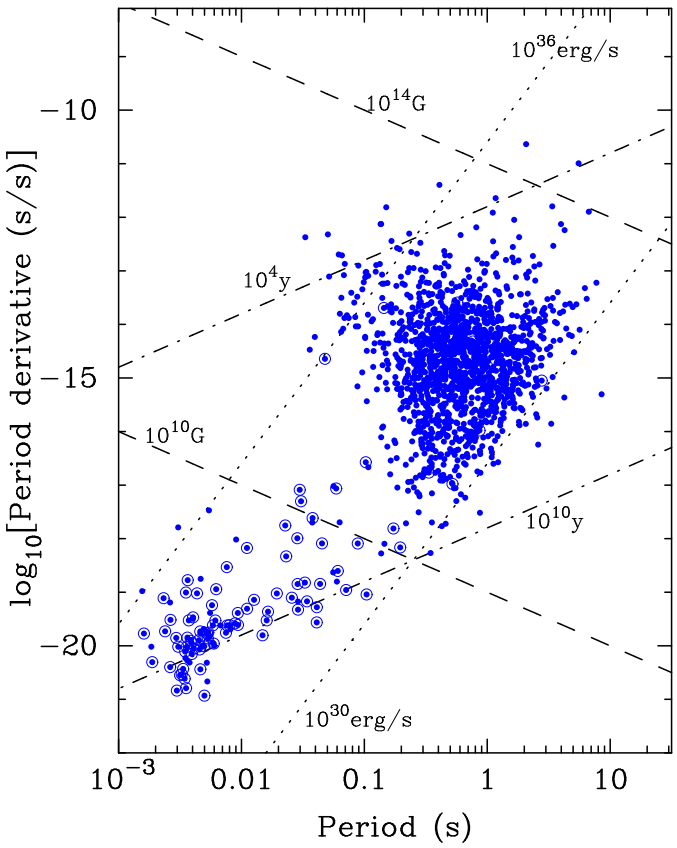

Figure 2.2 Distribution of rotation-powered pulsars in period and period derivative ($P - \dot{P}$-diagram). Shown are pulsars detected at radio wavelengths (blue dots). Pulsars in a binary system are additionally indicated with a blue circle. Lines of constant characteristic age τ_c (dash-dotted line), surface dipole magnetic field strength B_S (dashed line) and spin-down power $\dot{E}$ (dotted line) are also shown. Taken from Lorimer [2008].

PSR J1748−2446ad, which was found in the globular cluster Terzan 5 [Hessels et al., 2006]. The canonical and millisecond pulsars have quite distinct properties. Whereas the normal pulsars are relatively young ($\sim 10^7$ years) with strong surface magnetic fields ($\sim 10^{12}$ G), the MSPs are much older ($\sim 10^9$ years) with weaker surface magnetic fields ($\sim 10^8$ G). However, some of MSPs can be as energetic as the most energetic canonical pulsars with $\dot{E} > 10^{36}\,\mathrm{erg\,s^{-1}}$.

From the population of rotation-powered radio pulsars, the young and energetic pulsars as well as the most energetic millisecond pulsars are prime candidates for being observable as γ-ray pulsars.

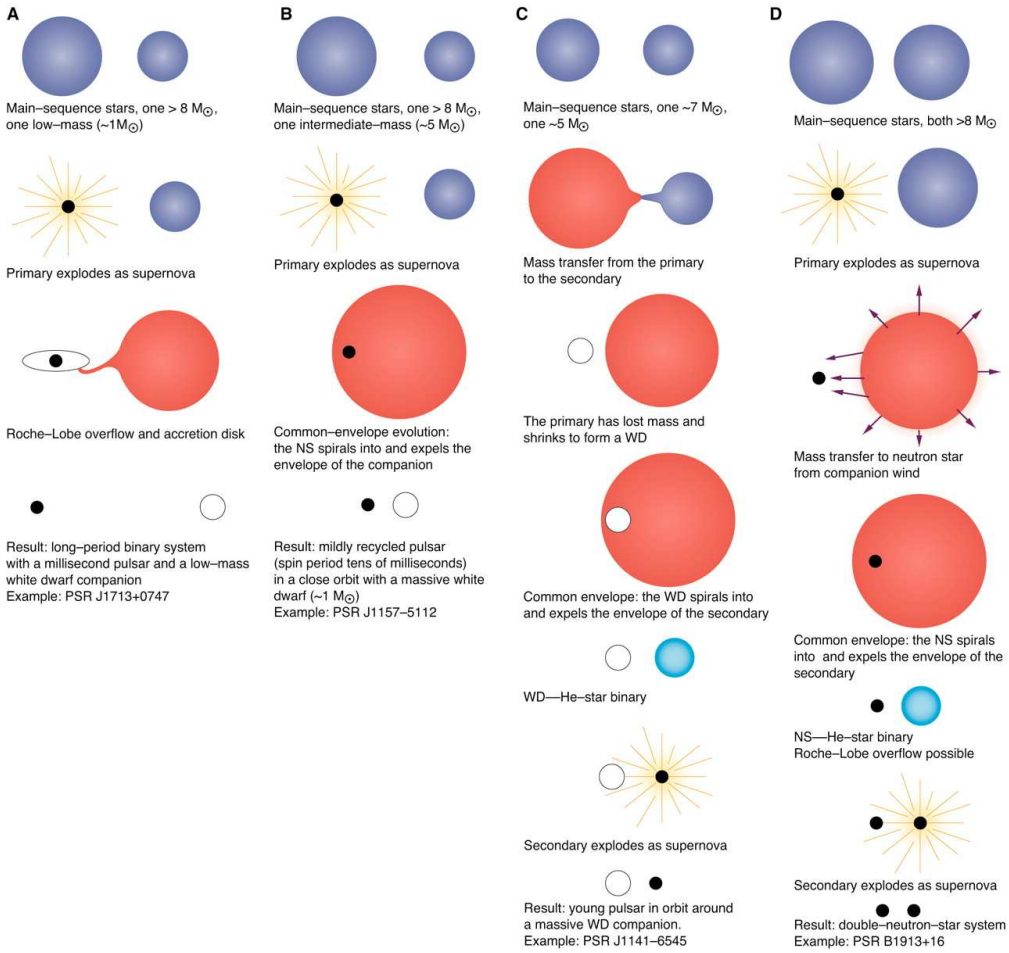

Figure 2.3 Overview on possible evolutionary scenarios to form a pulsar in a binary system (taken from Stairs [2004]). The standard scenario for the formation of a millisecond pulsar with a low-mass companion is shown in **A**.

2.1.4 Formation of Millisecond Pulsars

While only a small fraction of the total pulsar population is in a binary system (indicated by blue circles in Fig. 2.2), the majority of MSPs have a companion and/or are found in globular clusters. These observational evidences are believed to be connected to the formation of MSPs. A sketch of the standard principles of the evolution of pulsars in a binary system is depicted in Fig. 2.3.

The formation of MSPs starts with two main-sequence stars where the initially more massive star evolves faster and finally explodes in a supernova to form a neutron star [Bhattacharya and van den Heuvel, 1991]. Most of the binary systems disrupt during this process, but for favorable conditions the neutron star remains bound to its companion and spins down as a normal pulsar. When the remaining star comes to the end of its

main-sequence lifetime, it enters the red giant phase. The strong gravitational field of the neutron star then attracts matter from the red giant, causing it to overflow its Roche lobe which represents the gravitational equipotential between the two companions. An accretion disk around the neutron star is formed. During the accretion of matter from the massive companion, angular momentum is transferred to the neutron star and it spins up to shorter periods. This phenomenon is known as recycling of pulsars. Additionally, the magnetic field is greatly reduced [Alpar et al., 1982], though the cause of the field reduction is not well understood.

During the phase of accretion, the system may be visible as an X-ray binary due to its thermal X-ray emission. Two main categories are known for the X-ray binaries, low-mass X-ray binaries (LMXB) and high-mass X-ray binaries (HMXB), depending on the initial mass of the secondary star. The final state of the binary system and their constituents largely depends on the initial mass of the secondary star and the orbital parameters. For high-mass binaries ($M > 1\,\mathrm{M}_\odot$), the companion evolves rather quickly, leaving the neutron star to spin up to spin periods $P > 30\,\mathrm{ms}$ (Panel 'B' and 'D' in Fig. 2.3). When the spin-up of the neutron star is interrupted by the supernova explosion of the massive companion, the system is either disrupted or forms a double neutron star system with one mildly recycled pulsar orbiting a normal pulsar. For binaries with a low-mass companion ($M < 0.5\,\mathrm{M}_\odot$), the accretion phase is longer and the neutron star spins up to millisecond periods (Panel 'A' in Fig. 2.3). The companion evolves to form a white dwarf on a rather circular orbit around the millisecond pulsar with an eccentricity in the range from 10^{-5} to 10^{-1}. When the mass transfer generating the X-ray emission ceases, the radio emission of the MSP becomes visible. This scenario is supported by the detection of a radio MSP within a binary system for that an accretion disk has been observed prior to the detection of the radio MSP [Archibald et al., 2009].

The formation of isolated MSPs, i.e. recycled pulsars that are not in a binary system, is still under debate. It is suggested that the companion gets destroyed via the strong relativistic winds of the MSP [Ruderman et al., 1989] or that the system gets tidally disrupted after the formation of the MSP. For isolated MSPs in globular clusters, the high density of stars allows for numerous interaction and accretion phases and the neutron star to spin up to millisecond periods.

2.1.5 Gamma-Ray Emission from the Magnetosphere

Even 40 years after the discovery of the pulsar phenomenon, the exact mechanisms of how the observable pulsar emission is generated in the pulsar's magnetosphere are not yet fully understood. It is commonly believed that rotating neutron stars with their high magnetic fields create regions within the magnetosphere, so-called magnetospheric gaps, where charged particles are accelerated to relativistic energies by high electric fields. Thus far, no consensus on a model has been found as to how and where the high energy γ-ray emission is created within the pulsar's magnetosphere. The main emission models are the *Polar Cap* model, the *Outer Gap* model and the *Slot Gap* or *Two-Pole Caustic* model. In all models, the charged particles produce a beam of radiation within the strong pulsar's magnetosphere and the processes relevant for the observable radiation

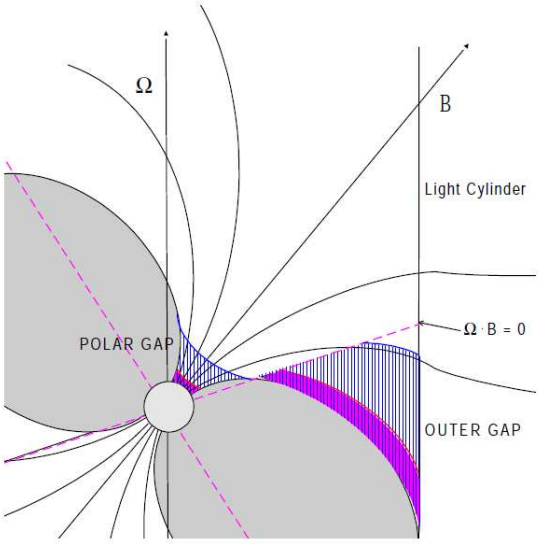

Figure 2.4 Schematic overview of the pulsar magnetosphere together with the regions of polar cap and outer gap activity. The co-rotating magnetosphere with closed field lines is indicated by the gray area. Dark pink regions indicate the regions of the polar cap and outer gap acceleration regions for young pulsars. Hatched blue regions indicate the polar cap and outer gap acceleration regions for older pulsars.

from radio to GeV and, possibly, TeV energies are curvature radiation (CR), synchrotron radiation (SR) and radiation due to inverse Compton scattering (IC). Recent reviews on these models can be found in Harding [2007] and in Hirotani [2008].

Goldreich-Julian model

The case of a rotating and perfectly conducting neutron star whose magnetic dipole moment is aligned with the rotation axis and that is surrounded by a force-free and plasma-filled magnetosphere was examined by Goldreich and Julian [1969]. A magnetic dipole rotating in vacuum will induce electric fields both parallel and perpendicular to the magnetic field lines [Deutsch, 1955]. For surface magnetic field strengths in the order of $B_{\mathrm{S}} \sim 10^{12}\,\mathrm{G}$, the induced electric force parallel to the magnetic field lines exceeds the gravitational force by many orders of magnitude. In the model of Goldreich and Julian [1969], charges can be pulled from the neutron star surface and it follows that a vacuum cannot exist outside a pulsar. The charges can freely move along the magnetic field lines in a force-free magnetosphere and redistribute themselves so that the component of the electric field parallel to the magnetic field $E_{||}$ is canceled. The induced electric field inside and outside of the neutron star, rotating with an angular velocity Ω, is

$$\mathbf{E} = -\frac{1}{c}\left((\Omega \times \mathbf{r}) \times \mathbf{B}\right) \tag{2.8}$$

and obeys the condition $\mathbf{E}\cdot\mathbf{B} = 0$ in a force-free magnetosphere which co-rotates with the pulsar. The co-rotating magnetosphere is then filled with a charge density ρ_{GJ} that reads

$$\rho_{\mathrm{GJ}} = \frac{\nabla\cdot\mathbf{E}}{4\pi} \approx -\frac{\Omega\cdot\mathbf{B}}{2\pi c}. \tag{2.9}$$

Co-rotation of the magnetosphere must break down at the light cylinder, where the orbital velocity reaches the speed of light.

Figure 2.4 shows a schematic overview of a neutron star and its magnetosphere for the general case of a rotator for which the rotation axis and the magnetic axis are not aligned. The boundary of the co-rotating magnetosphere, indicated as a gray shaded area in Fig. 2.4, is defined by the last magnetic field line that closes within the light cylinder. Its footprints on the stellar surface form the rim of the so-called polar cap, the region on the neutron star surface where all magnetic field lines pass through that do not close within the light cylinder. The radius of the polar cap is

$$R_{\mathrm{PC}} \approx R_{\mathrm{NS}} \times \sqrt{\frac{R_{\mathrm{NS}}}{R_{\mathrm{LC}}}} \approx 0.2 \left(\frac{P}{1\,\mathrm{s}}\right)^{-1/2} \mathrm{km}, \tag{2.10}$$

with R_{NS} as the radius of the neutron star. Charges can escape the pulsar's magnetosphere along the open field lines, forming the pulsar wind, and ρ_{GJ} is not retained everywhere in the magnetosphere. The regions where $\mathbf{E}\cdot\mathbf{B} \neq 0$ and the local charge density deviates from ρ_{GJ} are the regions where the magnetospheric gaps with a non-vanishing electric field $E_{||}$ are believed to form and particle acceleration takes place.

Polar-Cap Model

In the *polar cap* model, the acceleration region is located near the surface of the neutron star magnetic poles (see Fig. 2.4). Two main models are used to describe the mechanism of how the magnetospheric gap above the polar cap is formed. They differ as to whether or not charged particles can be pulled out of the neutron star surface.

A schematic view of the *space-charge limited flow* (SCLF) model [Harding et al., 1978, Sturner et al., 1995, Daugherty and Harding, 1996] is shown in Fig. 2.5 (a,left). In this model, charges can be extracted from the neutron star surface as the surface temperature of the neutron star T_{s} is above the thermal emission temperature $T_{\mathrm{e,i}}$ for electrons and ions, respectively. Many pulsars have measured surface temperatures in the range of $10^5 - 10^6\,\mathrm{K}$ which exceeds $T_{\mathrm{e,i}}$. As charged particles are extracted from the outer surface layer of the neutron star and flow along the open magnetic field lines, the local charge density deviates from ρ_{GJ} due to the curvature of the field lines [Arons and Scharlemann, 1979] or due to distortions of the field lines by effects of general relativity [Muslimov and Tsygan, 1992].

In pulsars with a very high magnetic field, it is expected that $T_{\mathrm{s}} < T_{\mathrm{e,i}}$ and the charged particles are bound to the conducting neutron star surface. In this model of a *vacuum gap* [Ruderman and Sutherland, 1975], illustrated in Fig. 2.5 (a,right), charged particles

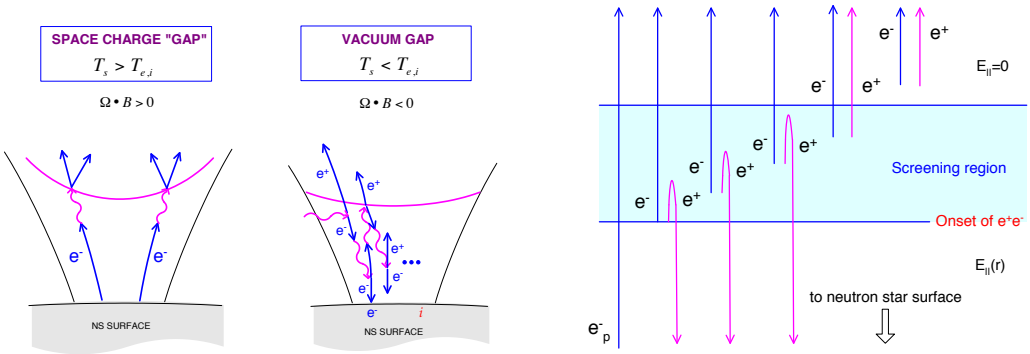

Figure 2.5 Formation of a space-charge limited flow (a, left panel) and vacuum (a, right panel) gap and of a pair formation front (b) in the polar cap model. Shown are the charges (electrons and positrons) extracted from the neutron star surface and the radiation mechanisms of curvature radiation and pair production within the pulsar's magnetosphere.

within the plasma-filled magnetosphere are accelerated along the open magnetic field lines upward or downward from the neutron star surface, depending on the sign of the charge, and a region free of charge above the polar cap is produced.

In both cases, a region of a high electric field with a strong component parallel to the magnetic field is formed above the polar cap. The alignment of the magnetic and spin axis, $\Omega \cdot \mathbf{B}$, determines the direction of acceleration of the charged particles. The charged particles that enter the region of the high electric field above the polar cap are further accelerated along the open magnetic field lines and emit γ-rays via CR or IC by scattering of soft thermal photons from the neutron star surface.

In most pulsars, additional magnetic pair production within the pulsar's strong magnetosphere from photons emitted via CR and/or IC of primary charged particles can lead to cascades of secondary (or higher generation) $e^{\pm}$-pairs as well as subsequent CR and IC photons that limit the width of the accelerating region by forming a so-called pair formation front (PFF) [Harding and Muslimov, 1998]. A schematic view of a PFF is given in Fig. 2.5 (b). The PFF screens the accelerating electric field $E_{||}$ above the neutron star surface and limits the particle acceleration.

For pulsars with larger ages as well as increased spin periods, the number of $e^{\pm}$-pairs and photons produced in the gap region decreases and the particles must accelerate over a longer distance until enough pairs from either CR or IC are produced to cancel the electric field $E_{||}$. The PFF forms at an higher altitude. Thus, young pulsars are believed to have a thin magnetospheric gap while old pulsars have a thick magnetospheric gap, as is indicated in Fig. 2.4.

In the polar cap scenario, the high energy emission is believed to come from near the

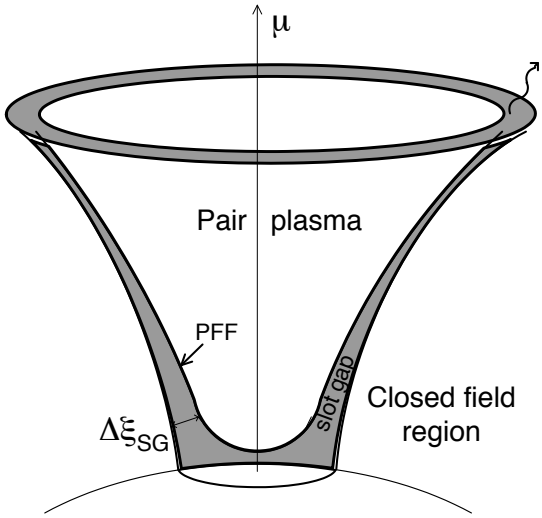

Figure 2.6 Overview of the slot gap model. The open gap with an accelerating field, shown in gray, forms along the last open magnetic field lines and extends to higher altitudes above the neutron star surface.

polar caps from CR and IC. The highest attainable CR energies are thereby limited by the width of the accelerating region. Due to the strong magnetosphere near the neutron star surface, the highest photon energies are limited by attenuation due to magnetic pair production within the magnetosphere. Thus, the curvature radiation is expected to have a sharp super-exponential cutoff at typically a few tens of GeV. With decreasing surface field strengths and larger gap widths, the maximum CR energy is believed to increase until it is finally limited by CR losses. The inverse Compton component is believed to be of much weaker strength compared to γ-ray-radiation from CR due to attenuation in the strong magnetic fields.

Slot-Gap Model

The *slot gap* model [Arons, 1983, Muslimov and Harding, 2003] is a variant of the polar cap model that allows acceleration to high altitudes above the polar cap even for young pulsars. The magnetospheric gap is formed in the region of the magnetic field lines that are near the boundary of the polar cap and that bend away from the spin axis. The acceleration of charged particles is not sufficient in this region to produce enough pairs at low altitudes to completely screen the accelerating electric field. The remaining

electric field causes the particles to accelerate to higher altitudes. Thus, the PFF curves upward near the magnetic field lines at the boundary of the polar cap (see Fig. 2.6). The PFF can even become asymptotically tangent to the boundary magnetic field lines and the accelerating region then extends up to the light cylinder. The γ-ray emission from CR and IC is thus expected from both low and high altitudes above the polar caps. As the magnetic field is weaker at high altitudes, the γ-ray emission is less affected by magnetic pair production and can extend to higher γ-ray energies compared to what is expected within the polar cap model. The slot gap model is interpreted as a physical representation of the *two-pole caustic* model [Dyks and Rudak, 2003] that postulates thin magnetospheric gaps extending from the polar cap up to the light cylinder along the surface of the last open magnetic field lines.

Outer-Gap Model

In the framework of the so-called *outer gap* models [Cheng et al., 1986, Romani, 1996, Hirotani and Shibata, 1999], the acceleration region is formed in the outer magnetosphere along the last open magnetic field line, between the null charge surface defined by $\Omega \cdot \mathbf{B} = 0$ and the light cylinder. In the plasma-filled outer magnetosphere, the positive and negative charges evolve separately depending on the sign of the charge relative to the null charge surface. Thus, as charges escape through the light cylinder above the null charge surface, they cannot be resupplied from below. A region of charge deficit forms, similar to the vacuum gap in the polar cap model, where an intense electric field is generated that accelerates charged particles to high energies.

In contrast to the polar cap models, the reservoir of $e^{\pm}$-pairs that screens the electric field and limits the region of particle acceleration is created from photon-photon pair cascades. These are produced in interactions of CR and IC photons with soft thermal photon fields or, self-consistently, with other IC photons. It is believed that some of these charged particles flow downward towards the stellar surface, thereby heating the surface and maintaining the flux of thermal photons.

In the outer gap scenario, the high energy γ-ray emission stems from a region with a local magnetic field that is orders of magnitude lower than the surface magnetic field. Thus, magnetic attenuation would then be irrelevant for most pulsars and the maximum attainable CR energies are limited by CR losses. The spectrum is expected to show an exponential cutoff at a few GeV. An additional component is expected from IC at TeV energies, that can escape the outer magnetosphere. A similar component from near the polar cap would be absorbed in the strong magnetosphere near the neutron star surface.

Outer-Gap Model with a Synchrotron Self-Compton Component

This model was put forward to explain the pulsed γ-ray radiation of the Crab pulsar that is observed up to 400 GeV and follows a broken power-law. In the models discussed so far, the γ-ray radiation from curvature radiation or inverse Compton scattering is expected from primary particles accelerated in the open gaps of a strong electric field. Here, the outer gap model is extended to include additional components from inverse

Compton scattering of secondary and tertiary particles on photons that stem either from external photon fields such as thermal UV or X-ray emission or from photon fields that have been produced by the primary particles (thus the name synchrotron self-Compton (SSC) component) [Lyutikov et al., 2012, Aleksić et al., 2012]. The exact mechanism is, however, not well understood and details are currently under study.

2.1.6 Observations at HE and VHE wavelengths

In the HE γ-ray domain only seven γ-ray emitting pulsars were seen with high significance with *EGRET* [Thompson, 2004], all of them young and energetic normal pulsars. Since the launch of the satellite based observatories *Fermi* Large Area Telescope (LAT) [Atwood et al., 2009] and *AGILE* [Tavani et al., 2009], the number of γ-ray emitting pulsars was greatly increased. *Fermi* reported pulsed HE γ-ray emission from 46 pulsars [Abdo et al., 2010d] within the first 1.5 years of operation and *AGILE* from four additional pulsars [Pellizzoni et al., 2009]. Among the γ-ray emitting pulsars seen by *Fermi*, a population of γ-ray emitting MSPs emerges [Abdo et al., 2009, 2010c].

These observations give a wealth of information for detailed modeling of the pulsar spectrum and light curve. The models have to incorporate a detailed modeling of the pulsar's magnetosphere, the pulsar properties and its geometry, i.e. the magnetic inclination angle α between the magnetic and rotation axis and the observer angle ζ between the rotation axis and the line of sight. The HE γ-ray pulsar light curves show a wide variety in the number of peaks and their position relative to the peaks as observed at other wavelength and allow to draw conclusions about the origin of the emission within the pulsar's magnetosphere and the pulsar's viewing geometry [e.g. Romani and Watters, 2010].

The spectrum of pulsed emission is a superposition of several emission mechanisms. Thermal emission from the surface of neutron stars as well as synchrotron radiation from primary and secondary electrons from within the pulsar's magnetosphere dominate the observed flux up to energies of 100 MeV. Curvature radiation from primary electrons is the dominant component from 1 GeV up to 100 GeV. A cutoff at a few GeV is predicted in most of the models whereas the shape of the cutoff dependends on the specifics of the model such as the maximum attainable energies of accelerated particles or the attenuation of emitted photons within the pulsar's magnetosphere. Such a cutoff is observed for most of the HE γ-ray pulsars [Abdo et al., 2010d].

Inverse Compton radiation from primary and secondary generation electrons contributes mainly at 0.1 TeV to 1 TeV, however, at a much smaller level than curvature radiation. Despite extensive searches in the VHE energy band for pulsed emission from pulsars [e.g. Chadwick et al., 2000, Lessard et al., 2000, de Naurois et al., 2002, Aharonian et al., 2004a, 2007], pulsed VHE γ-ray emission was reported so far only for the young and energetic 33 ms Crab pulsar, seen by MAGIC [Aliu et al., 2008] and VERITAS up to 400 GeV [VERITAS Collaboration et al., 2011]. The observed VHE γ-ray spectrum follows a broken-power law shape up to 400 GeV and was not predicted in most models.

2.2 Pulsar Wind Nebulae

In the previous section, the possible mechanisms for generation of pulsed γ-ray emission from within the pulsar's magnetosphere have been outlined. While searches for pulsed γ-ray emission from pulsars beyond 100 GeV has resulted so far in the detection of the Crab pulsar only [Aliu et al., 2008, VERITAS Collaboration et al., 2011], pulsar wind nebulae (PWNe) compose by now one of the most abundant classes of VHE γ-ray emitters.

Pulsars loose most of their rotational energy in the form of a relativistic wind of charged particles. As the charged particles flow outward, they interact with the surrounding medium. A standing shock front forms at some distance of the pulsar, the so-called termination shock where the charged wind particles are isotropized and accelerated leading to a bubble of a relativistically hot fluid beyond the termination shock. This region is visible throughout the electromagnetic spectrum from radio to TeV energies as a pulsar wind nebula (PWN). Reviews of PWNe as seen in the radio and X-ray energy band can be found in e.g. Gaensler and Slane [2006] and in the TeV energy band in e.g. Wilhelmi [2011].

In this section, the details on structure and evolution of PWNe are outlined together with basic calculations on the radiation mechanisms responsible for the observed emission.

2.2.1 Structure of Pulsar Wind Nebulae

Figure 2.7 shows a schematic overview of the structure of a PWN (left panel) embedded in an evolving young ($\sim 1\,\mathrm{ky}$) SNR (right panel). While this overview constitutes only a snapshot in the evolution of a PWN (see more in Section 2.2.2 on the evolution of PWNe) and is based on some simplifying assumptions, e.g. a uniform density within the SNR, it can be used to highlight the basic structure of a PWN that is valid for most its lifetime.

The spherically expanding PWN is powered by a pulsar that is located at the center of the PWN and near the center of the evolving SNR. As pulsars are generally believed to receive a kick velocity at their birth with a typical value of $250 - 300\,\mathrm{km/s}$ [Hansen and Phinney, 1997], this assumption is valid for young PWNe and SNRs. The pulsar emits a wind of highly relativistic particles and electromagnetic energy that is proportional to the pulsar's spin-down energy and originates in the pulsar's magnetosphere from within the light cylinder of $\sim 10^8\,\mathrm{cm}$. The particle component of the pulsar wind consists a plasma of highly relativistic electrons and positrons with a possible contribution of heavier nuclei. For more details on the pulsar's magnetosphere and on the debate on possible mechanisms of particle acceleration within the magnetosphere, see section 2.1.5. The pulsar and its magnetosphere are indicated by a black dot (labeled PSR) in Fig. 2.7 (left panel).

The pulsar wind then leaves the magnetosphere and the particles with the frozen-in magnetic fields traverse outwards, blowing a cavity in the surrounding outer nebula (region A in Fig. 2.7). The wind is decelerated and eventually terminates in a standing

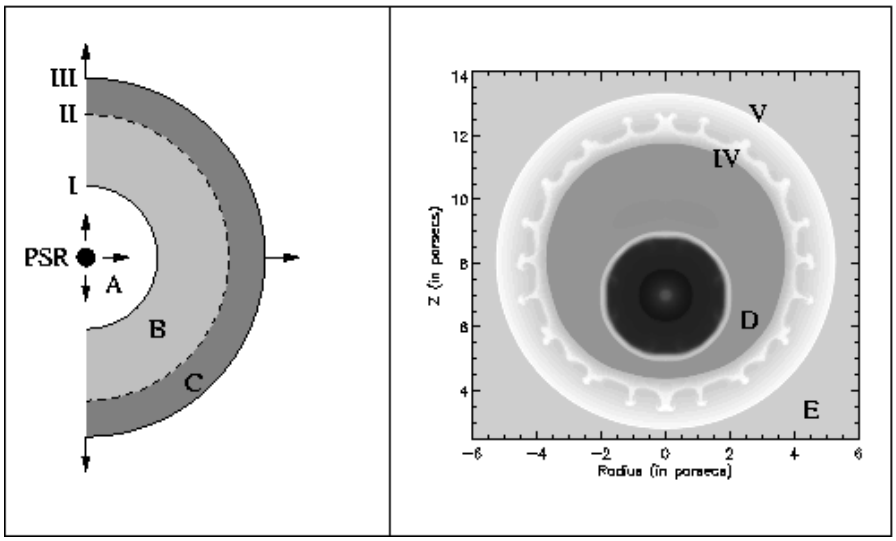

Figure 2.7 Overview of a PWN (left panel) expanding freely in a SNR (right panel). The *left panel* shows schematically the basic PWN structure: The pulsar (PSR) is located in the center of the pulsar wind cavity (region A) which is limited by the pulsar wind termination shock (interface I). The (visible) actual pulsar wind nebula is the shocked pulsar wind material in the pulsar wind bubble (region B). This region is separated from shocked swept-up SN ejecta (region C) by the contact discontinuity (interface II). Interface III denotes the pulsar wind forward shock. The *right panel* shows a logarithmic gray-scaling of the density distribution of such a PWN (dark core region) embedded in freely expanding SN ejecta (region D). Interfaces IV and V denote the SN reverse and forward shock, respectively, whereas region E consists of the interstellar medium. Taken from van der Swaluw [2005].

shock front (wind termination shock, boundary I in Fig. 2.7), where the ram pressure of the wind is balanced by the internal pressure of the more slowly-moving ambient material. Whereas the pulsar wind carries most if its energy in the form of electromagnetic energy near the pulsar's magnetosphere, the bulk of this energy has been transferred to the particle population near the wind termination shock. The mechanism of this energy transfer is still largely unknown (see e.g. Arons [2002]).

At the site of the wind termination shock, the particles are then isotropized and accelerated. The distribution of energies of the particle population takes on a power-law form. Up to the termination shock, the particles do not radiate, but flow freely within the wind cavity. Downstream the termination shock, the accelerated particles loose energy in form of synchrotron radiation and inverse Compton scattering, while being advected away from the wind termination shock. It is this region (region B in Fig. 2.7) that is visible throughout the electromagnetic spectrum as the actual pulsar wind nebula. The magnetic fields in the nebula can reach values up to several $100\,\mu$G, and decrease when the PWN expands to values in the order of typically $10\,\mu$G.

The outer edge of the PWN expands supersonically into the surrounding SN ejecta, thereby sweeping up and shock heating the SN ejecta (region C in Fig. 2.7) and is bounded by the contact discontinuity and PWN forward shock (boundaries II and III in Fig. 2.7) where the pulsar wind velocity becomes subsonic. The right panel of Fig. 2.7 shows a blow-up of the PWN (dark core) surrounded by the shell-like SNR with a double-shock structure (SN reverse and forward shock are denoted by boundaries IV and V). The PWN is embedded in freely expanding SN ejecta (region D) while the SNR expands into the ISM (region E). The picture of a PWN inside a freely expanding SNR as it is drawn in this section is called the *supersonic expansion stage*. The details of the exact layout of the PSR/PWN/SNR-complex depends on many variables such as the pulsar's spin-down energy history, the density profile of the surrounding medium, the pulsar's space velocity and evolutionary stage of the PWN and/or SNR.

2.2.2 Evolution of Pulsar Wind Nebulae

The standard picture of PWN evolution can be divided into the following stages that are closely bound to the evolution of the SNR. Detailed simulations have been performed by van der Swaluw et al. [2001] and van der Swaluw et al. [2004].

- *Supersonic expansion phase:* The PWN is embedded in unshocked SN ejecta and expands supersonically and, in an homogeneous environment, spherically into the SN ejecta. The SNR shows a double-shock structure of a SN reverse and forward shock. The SN reverse shock forms almost immediately after the SN explosion and, after a phase of moving outward interior to and with a smaller velocity than the supersonically moving SN forward shock, begins to move inward when the swept-up mass of the material ambient to the SNR is larger than the mass ejected by the SN. The supersonic expansion phase covers the first several thousand years of the PWN lifetime and ends as soon as the reverse shock collides with the PWN shock.

- *Reverse shock interaction phase:* After a few thousand years, the PWN shock will encounter the SN reverse shock leading to a crushed PWN. This interaction can lead to large enhancements of the magnetic field within the PWN (Rayleigh-Taylor instabilities). In case of an anisotropic arrival of the reverse shock due to e.g. density gradients in the material surrounding the SNR and/or a high velocity of the pulsar, the crushed PWN can have an asymmetric morphology and/or be offset from the pulsar position.

- *Subsonic expansion phase:* In this phase, the PWN bubble is now steadily expanding with subsonic velocity into the shocked SN ejecta that has been heated by the SN reverse shock. The distance that the pulsar traveled in this phase can become comparable to the actual PWN size. In case of a large offset of the PWN from the pulsar, it is not powered by the pulsar any more and becomes relic. If the pulsar and its PWN reach the edge of the SNR where the sound speed drops, the velocity of the pulsar becomes supersonic again, ending this phase of PWN evolution.

- *Bow shock phase:* A pulsar with a high kick velocity reaches the edge of the SNR after typically 40000 years. At the edge of the SNR, the sound speed in the shocked SN ejecta decreases rapidly. Thus, when the velocity of the pulsar becomes supersonic again, either at the edge of the SNR or outside of the SNR in the ISM, the ram pressure of the pulsar's movement will confine the PWN. This leads to a cometary bow shock. The forward shock of the PWN may be visible as Hα emission due to shock excitation and charge exchange of the surrounding neutral gas. If the pulsar overtakes the PWN shock, further distortions of the PWN morphology are expected. This phase will continue until the spin-down power drops below a critical value to further power the PWN.

Prototypical examples of young PWNe that have been detected with H.E.S.S. at TeV energies are e.g. SNR G0.9+0.1 [Aharonian et al., 2005], Crab Nebula [Aharonian et al., 2006d], SNR G21.5−0.9 and Kes 75 [Djannati-Ataï et al., 2008]. The VHE emission of these PWNe is generally very compact and appears point-like to H.E.S.S.. Extended VHE emission that is often offset from the current pulsar position has been observed from middle-aged and more evolved PWNe such as HESS J1825−137 [Aharonian et al., 2006a] and Vela X [Aharonian et al., 2006b]. No VHE emission from PWNe with bow shock morphology has been observed so far.

2.2.3 Gamma-ray Production in Pulsar Wind Nebulae

The main models for production of VHE γ-ray radiation inside of PWNe discuss a leptonic or a hadronic scenario. In the leptonic scenario (first MHD models were developed by Rees and Gunn [1974], Kennel and Coroniti [1984]), the particle population responsible for the electromagnetic radiation from radio through VHE wavelengths consists of non-thermal electrons and positrons, injected by the pulsar and accelerated to relativistic energies in the PWN. While the X-ray radiation is produced via synchrotron radiation (SR) from energetic electrons in the strong magnetic field of the PWN, the VHE γ-ray radiation is expected to be produced by inverse Compton scattering (IC) of ambient low energy photon fields such as the cosmic microwave background radiation (CMB), stellar radiation or (infrared) emission from interstellar dust. In the hadronic scenario as discussed by Horns et al. [2006], Bednarek and Bartosik [2003], the pulsar wind contains a mixture of electrons and heavier nuclei that are accelerated in the PWN. While the X-ray emission is still attributed to SR from relativistic electrons, the VHE γ-ray radiation is believed to be a product of the decay of neutral pions that were produced in interactions of the energetic nuclei and target nuclei from the surrounding medium.

In this section, the basic equations for TeV γ-ray production in both scenarios are outlined.

Electronic Origin of γ-rays

The basic radiation processes of synchrotron and inverse Compton scattering radiation are presented as reviewed in the works of Blumenthal and Gould [1970] and Ginzburg

[1979]. A review on the application to PWNe can be found in Aharonian et al. [1997] and de Jager and Djannati-Ataï [2009].

Synchrotron Radiation

Synchrotron radiation (SR) is the radiation emitted by relativistic electrons spiraling around magnetic field lines. The total energy loss rate of a single electron with velocity **v** in a magnetic field **B** due to SR is

$$-\left(\frac{dE}{dt}\right) = 2\,\sigma_{\rm T}\,c\,U_{\rm mag}\left(\frac{v}{c}\right)^2\gamma^2\sin^2\phi, \tag{2.11}$$

where $\sigma_{\rm T}$ denotes the Thomson cross-section [2], $U_{\rm mag} = B^2/2\pi$ the energy density of the magnetic field, γ the Lorentz factor of the electron [3] and ϕ the angle between the electron velocity vector **v** and magnetic field vector **B**, also called pitch angle. Averaging over an isotropic distribution of pitch angles ($\langle\sin^2\phi\rangle_{\rm av} = 2/3$) and in the relativistic limit $(v/c)^2 \to 1$, the average total energy loss rate of a single electron is

$$-\left(\frac{dE}{dt}\right) = \frac{4}{3}\,\sigma_{\rm T}\,c\,U_{\rm mag}\,\gamma^2. \tag{2.12}$$

It is conventional to define a critical frequency of SR emitted by a single electron as

$$\nu_{\rm c} = \gamma^2\left(\frac{eB}{2\pi m_{\rm e}}\right). \tag{2.13}$$

The spectrum of the synchrotron photons with frequency ν is proportional to $\nu^{1/3}$ for $\nu < \nu_{\rm c}$, sharply peaks at a peak frequency $\nu_{\rm SR} \simeq \nu_{\rm c}/3$ and falls off exponentially as $\nu^{1/2}e^{-\nu/\nu_{\rm c}}$ for $\nu >> \nu_{\rm c}$. The spectrum depends on the magnetic field B and the Lorentz factor γ of the electron. Assuming that all energy is emitted at the peak frequency $\nu_{\rm SR}$, (the so-called δ-approximation [e.g. Ginzburg, 1979]), the characteristic energy $E_{\rm SR} = h\nu_{\rm SR}$ of the SR photons from a population of mono-energetic electrons of energy $E_{\rm e}$ is

$$E_{\rm SR} \simeq 2\times10^{-4}\left(\frac{B}{10\,\mu{\rm G}}\right)\left(\frac{E_{\rm e}}{1\,{\rm TeV}}\right)^2\ {\rm keV}, \tag{2.14}$$

where the values for the charge and mass of the electron have been substituted and the magnetic field strength and energy of electrons have been normalized to typical values for a PWN. A higher magnetic field strength or more energetic particles shift the radiation up in energy.

The differential synchrotron spectrum from electrons that have a power-law energy distribution $N_{\rm e}(E_{\rm e}) \propto E_{\rm e}^{-p}$ with a spectral index p follows also a power-law of the form $\Phi_{\rm SR} \propto B^{\alpha_{\rm SR}}E_\gamma^{-\alpha_{\rm SR}}$ with photon index $\alpha_{\rm SR} = (p+1)/2$. It should be noted that any

[2] $\sigma_{\rm T} = \frac{8\pi}{3}r_{\rm e}^2 = 0.665\times10^{-24}\,{\rm cm}^2$, where $r_{\rm e} = 2.8\times10^{-13}\,{\rm cm}$ denotes the classical electron radius.
[3] $\gamma = E_{\rm e}/(m_{\rm e}c^2) = (1-v^2/c^2)^{-1/2}$.

cut-off in the electron spectrum, corresponding to e.g. the maximum attainable energies of electron acceleration, causes also a cut-off in the synchrotron spectrum. Typical SR spectra of PWNe peak in the X-ray energy band at keV energies.

From Eq. 2.14, the electron energy responsible for the observed SR photon energies can be estimated as (see also de Jager and Djannati-Ataï [2009])

$$E_{\mathrm{e}} \simeq 70 \left(\frac{B}{10\,\mu\mathrm{G}}\right)^{-1/2} \left(\frac{E_{\mathrm{SR}}}{1\,\mathrm{keV}}\right)^{1/2} \mathrm{TeV}. \tag{2.15}$$

It becomes apparent from Eq. 2.15 that electron energies up to at least 70 TeV are required to emit 1 keV SR photons for typical magnetic fields of PWNe in the order of $10\,\mu$G.

Inverse Compton Scattering

Inverse Compton scattering (IC) radiation is produced when relativistic electrons scatter low energy photons to high energies, at the expense of the kinetic energy of the electrons. Different radiation fields such as the cosmic microwave background radiation (CMB), light from dust and starlight can serve as target photon fields. Aharonian et al. [1997] consider IC on the CMB as the dominant energy loss process for electrons with energies up to 100 TeV. The CMB constitutes a uniform and isotropic target photon field and its photon energies follow a narrow Planck distribution with temperature T. The mean energy of target photons is $E_{\mathrm{ph}} = 2.7\,kT \simeq 6 \times 10^{-4}$ eV.

The total energy loss rate of a single electron in the Thomson regime is

$$-\left(\frac{dE}{dt}\right) = \frac{4}{3}\sigma_{\mathrm{T}}\, c\, U_{\mathrm{rad}}\, \gamma^2. \tag{2.16}$$

where σ_{T} denotes the Thomson cross-section and U_{rad} the energy density of the target photon field. This equation is correct as long as the energy of the target photons E_{ph} is well below the electron energy E_{e}, i.e. $(4E_{\mathrm{e}}E_{\mathrm{ph}})/(m_{\mathrm{e}}c^2) << 1$. For electron energies up to 100 TeV, the Thomson limit is a good approximation for scattering off the CMB. At higher electron or target photon energies, IC takes place in the Klein-Nishina (KN) regime and the full KN cross-section given in Blumenthal and Gould [1970] has to be invoked. Inverse Compton scattering in the Thomson regime is more efficient and the cross-section decreases towards higher energies in the KN regime. A KN suppression factor of $f_{\mathrm{KN}} = 2/3$ was used for the H.E.S.S. energy range by Aharonian et al. [2006a].

The spectrum of IC photons with frequency ν is proportional to ν for low electron energies and exhibits a sharp cut-off at high energies. In the Thomson limit, a population of mono-energetic electrons of energy E_{e} scattering on target photons with a mean energy of E_{ph} emit IC photons with a characteristic energy of

$$E_{\mathrm{IC}} \simeq \frac{4}{3} E_{\mathrm{ph}}\, \gamma^2. \tag{2.17}$$

Substituting the values for the electron mass and velocity of light leads to a typical

energy of IC photons of

$$E_{\rm IC} \simeq 5 \times 10^{-3} \left(\frac{E_{\rm ph}}{10^{-3}\,{\rm eV}}\right) \left(\frac{E_{\rm e}}{1\,{\rm TeV}}\right)^2 \,{\rm TeV}, \tag{2.18}$$

where the target photon energy $E_{\rm ph}$ and electron energy $E_{\rm e}$ are given as reference values. The energy of the IC photons does not depend on the magnetic field, but depends on the assumed radiation field and energy of the emitting electron.

The spectrum of radiation produced by a power-law distribution of electron energies with spectral index p follows again a power law with a photon index of $\alpha_{\rm IC} = (p+1)/2$.

From Eq. 2.18, the typical energies of electrons that up-scatter CMB target photons to a typical energy of 1 TeV can be estimated as

$$E_{\rm e} \simeq 18 \left(\frac{E_{\rm IC}}{1\,{\rm TeV}}\right)^{1/2} \,{\rm TeV}. \tag{2.19}$$

It can be noted that the energies of the electrons responsible for the IC photons with a typical energy of 1 TeV (for a target photon field with mean energy 10^{-3} eV) are less energetic than the electrons emitting SR photons with a typical energy of 1 keV (see also Eq. 2.15).

Energy Losses

Due to SR and IC, electrons loose energy, limiting their lifetime as radiating particles. The lifetime of the electrons can be defined as [Aharonian et al., 1997]

$$\tau = \frac{E_{\rm e}}{-\langle dE_{\rm e}/dt \rangle}. \tag{2.20}$$

Substituting the energy loss rates due to SR (Eq. 2.12), the total synchrotron lifetime of an electron with energy $E_{\rm e}$ and assuming isotropic pitch angles is given by

$$\tau_{\rm rad} = \frac{m_{\rm e}^2\, c^4}{\frac{4}{3}\sigma_{\rm T}\, c\, U_{\rm B}} \frac{1}{E_{\rm e}}, \tag{2.21}$$

where $U_{\rm B}$ denotes the energy density of the magnetic field. Substituting the reference value of $U_{\rm B} = 2.5\,{\rm eV\,cm^{-3}}(B/10\mu G)^2$ for the magnetic energy density and Eq. 2.15, the synchrotron cooling time of electrons of higher energy, responsible for SR, can be found as (see also de Jager and Djannati-Ataï [2009])

$$\tau_{\rm SR}(E_{\rm SR}) \simeq 1.6 \times 10^3 \left(\frac{B}{10\,\mu{\rm G}}\right)^{-3/2} \left(\frac{E_{\rm SR}}{1\,{\rm keV}}\right)^{-1/2} \,{\rm years}. \tag{2.22}$$

Correspondingly, the synchrotron cooling time of electrons of lower energy that are responsible for IC can be found when substituting the magnetic energy density and

Eq. 2.19 as (see also de Jager and Djannati-Ataï [2009])

$$\tau_{\rm SR}(E_{\rm IC}) \simeq 7.6 \times 10^3 \left(\frac{B}{10\,\mu{\rm G}}\right)^{-2} \left(\frac{E_{\rm IC}}{1\,{\rm TeV}}\right)^{-1/2} {\rm years}. \tag{2.23}$$

The synchrotron cooling time depends on the magnetic field and energy of the emitting electrons, respectively. Electrons of higher energy loose energy at a larger rate than those of lower energy and thus a steepening of the electron spectrum is expected due to synchrotron cooling. Electrons of lower energy, responsible for the 1 TeV IC photons have larger lifetime by a factor of ~ 4 than the electrons of higher energy that are responsible for the 1 keV SR photons. In addition, for an increasing magnetic field, the synchrotron cooling time shortens faster for low-energy electrons than for the electrons of higher energy. IC emission is thus suppressed for magnetic fields larger than $10\mu G$ and synchrotron losses dominate for $B > 3\mu G$.

IC losses become important only for magnetic fields in very extended PWNe where the magnetic field may drop below the ISM value. The IC cooling lifetime is similar to Eq. 2.21, if the magnetic energy density is replaced by the energy density of the target photon field $U_{\rm rad}$. The total synchrotron and IC lifetime for the electrons responsible for IC photons by scattering off the CMB is (see also de Jager and Djannati-Ataï [2009])

$$\tau(E_{\rm rad}) \simeq 10^5 \left(\frac{1}{(1+0.144(B/1\,\mu{\rm G})^2)(E/1\,{\rm TeV})^{1/2}}\right) {\rm years}, \tag{2.24}$$

where a KN suppression factor of 2/3 was included. For such extended PWNe, SR might be below detectable levels and the PWN is only seen in γ-rays with a limiting lifetime of 10^5 years assuming that most electrons are injected at early times.

X-ray to VHE Connection

Assuming that the same electron population is responsible for both SR and IC, one can relate the energies of the electron responsible for SR from Eq. 2.15 and IC from Eq. 2.19 to derive the ratio of energy fluxes from SR and IC as

$$\frac{f_{\rm IC}(E_{\rm IC})}{f_{\rm SR}(E_{\rm SR})} \simeq \left(\frac{E_{\rm SR}/1\,{\rm keV}}{E_{\rm IC}/1\,{\rm TeV}}\right) \simeq \frac{f_{\rm KN}\,U_{\rm rad}}{U_{\rm B}} \simeq 0.01\,f_{\rm KN} \left(\frac{B}{10\,\mu{\rm G}}\right)^{-2}. \tag{2.25}$$

with $U_{\rm rad} = 0.26\,{\rm eV\,cm^{-3}}$ the energy density of the CMB target photon field, $U_{\rm B} = 2.5\,{\rm eV\,cm^{-3}}(B/10\mu G)^2$ the energy density of the magnetic field and $f_{\rm KN}$ the KN suppression factor. This ratio can be used to calculate the magnetic field for different radiation fields with the assumption of a uniform magnetic field within the nebula and isotropic pitch angles.

2.2.4 Observations at X-ray and VHE wavelengths

PWNe from canonical pulsars compose by now the most numerous class of Galactic sources seen by H.E.S.S. at TeV energies. A systematic search for coincidences between

VHE γ-ray sources in the H.E.S.S. Galactic Plane Survey, covering the inner part of our Galaxy from -60° to 30° in Galactic longitude and -2° to 2° in Galactic latitude, and a sample of 435 radio pulsars, taken from the Parkes Multibeam Pulsar Survey [Hobbs et al., 2004, and references therein] as collected in the ATNF pulsar database [Manchester et al., 2005], showed that pulsars with a high spin-down energy flux at Earth of $\dot{E}/d^2 > 10^{35}\,\mathrm{erg\,s^{-1}}$ have a high probability of being detectable as TeV PWNe [Carrigan, 2007, Carrigan et al., 2008]. The observed VHE PWNe, all powered by canonical pulsars, show a wide range of characteristics. Many PWNe are extended beyond the H.E.S.S. point spread function and show an asymmetric morphology with an offset to the nominal pulsar position. Only a few PWNe are point-like and are powered by very young pulsars. See e.g. Wilhelmi [2011] for an overview.

Searches for PWNe from pulsars in the X-ray energy domain have revealed numerous detections as well with a very large diversity of properties of the PWN such as morphology and pulsar such as characteristic age (see e.g. Kargaltsev and Pavlov [2008]). The large sample of known X-ray and VHE emitting PWNe from canonical pulsars have made first studies of the scaling of the X-ray and VHE luminosity with pulsar parameters such as the spin-down power $\dot{E}$ and characteristic age τ_c possible (see e.g. Mattana et al. [2009], Kargaltsev and Pavlov [2010]). In a study by Mattana et al. [2009], 14 canonical pulsars with an X-ray PWN with associated VHE emission have been used to relate the $2-10\,\mathrm{keV}$ X-ray luminosity to the VHE luminosity in the $1-30\,\mathrm{TeV}$ energy band in dependence of the pulsar's spin-down power $\dot{E}$ and characteristic age τ_c. Figure 2.8 shows the scaling laws for $\dot{E}$ (left column) and τ_c (right column) together with the measured values of L_X (middle row), L_γ (upper row) and $F_\gamma^{1-30\,\mathrm{TeV}}/F_\mathrm{X}^{2-10\,\mathrm{keV}}$ (lower row) for the 14 X-ray/VHE PWNe.

It was found that the $2-10\,\mathrm{keV}$ X-ray luminosity $L_\mathrm{X}^{2-10\,\mathrm{keV}}$ increases with $\dot{E}$ and decreases with τ_c as

$$\log_{10} L_\mathrm{X}^{2-10\,\mathrm{keV}} = (33.8 \pm 0.04) + (1.87 \pm 0.04) \log_{10} \left(\frac{\dot{E}}{10^{37}\,\mathrm{erg\,s^{-1}}} \right), \tag{2.26}$$

$$\log_{10} L_\mathrm{X}^{2-10\,\mathrm{keV}} = (33.7 \pm 0.04) - (2.49 \pm 0.06) \log_{10} \left(\frac{\tau_\mathrm{c}}{10^4\,\mathrm{years}} \right). \tag{2.27}$$

No such scaling with $\dot{E}$ and τ_c is observed for the $1-30\,\mathrm{TeV}$ luminosity for the sample of canonical pulsars. The distance-independent ratio of TeV to X-ray flux $F_\gamma^{1-30\,\mathrm{TeV}}/F_\mathrm{X}^{2-10\,\mathrm{keV}}$ thus is found to decrease with $\dot{E}$ and increase with τ_c as

$$\log_{10} F_\gamma^{1-30\,\mathrm{TeV}}/F_\mathrm{X}^{2-10\,\mathrm{keV}} = (0.57 \pm 0.04) - (1.88 \pm 0.05) \log_{10} \left(\frac{\dot{E}}{10^{37}\,\mathrm{erg\,s^{-1}}} \right), \tag{2.28}$$

$$\log_{10} F_\gamma^{1-30\,\mathrm{TeV}}/F_\mathrm{X}^{2-10\,\mathrm{keV}} = (0.89 \pm 0.04) + (2.14 \pm 0.07) \log_{10} \left(\frac{\tau_\mathrm{c}}{10^4\,\mathrm{years}} \right). \tag{2.29}$$

These correlations can be explained in a simplified leptonic scenario as described in Mattana et al. [2009], where the X-ray and TeV emission are believed to originate from electron populations, of different age and energy that are limited by cooling due to radiation losses. In this model, it was assumed that the magnetic field in the nebula is constant and uniform and that adiabatic losses are negligible. The X-ray emission thereby stems from SR produced by high-energy electrons in the magnetic field of the PWN. The VHE emission originates from IC of less energetic electrons, up-scattering ambient photons fields that are provided e.g. by the cosmic microwave background radiation (CMB), optical starlight and infrared emission from dust.

In this scenario, the X-ray and VHE emission are connected via the same parent population of electrons, but probe electrons of different energy and age. While for 1 TeV IC photons, produced by up-scattering CMB in the Thomson regime, an electron energy of $\sim$ 18 TeV is needed (see also Eq. 2.19), electron energies of at least $\sim$ 70 TeV are needed to produce 1 keV SR photons in a magnetic field of 10 μG (see also Eq. 2.15). In a higher magnetic field of 50 μG, the energy of the electrons responsible for the 1 keV emission is correspondingly lower (31 TeV).

The lifetime of both electron populations is limited by energy losses due to SR, the dominant energy loss mechanism for magnetic field strengths larger than 3 μG [Aharonian et al., 1997]. As the electrons responsible for the X-ray emission have usually higher energies and are subject to severe radiative cooling losses via SR, their lifetime of a few 10^3 years is short compared to typical ages of PWNe (a few 10^4 years) and they are in the so-called cooled regime. The SR lifetime is 1800 years (400 years) for electrons that emit 1 keV photons in a magnetic field of 10 μG (50 μG). The VHE emission, however, is generated by electrons of usually lower energy with cooling times that are larger than the lifetime of the X-ray emitting electrons. The corresponding SR lifetime of the high energy electrons that emit 1 TeV photons by up-scattering the CMB is 6500 years (300 years) in a magnetic field of 10 μG (50 μG). See also Eq. 2.23 and 2.22. Thus, the X-ray emission represents the current energy output of the system, while the VHE emission builds up over a longer time range and traces the history of particle injection into the PWN. Therefore, different cases can be distinguished depending on the pulsar age τ_c compared to the lifetime of electrons emitting X-ray radiation (t_X) and lifetime of electrons emitting VHE γ-rays (t_γ). The cases are:

- $\tau_c < t_X < t_\gamma$:

  Electrons are steadily injected into the PWN. The X-ray and VHE radiation build up, while the latter will onset on a longer time scale. The PWN will have a small extension.

- $t_X < \tau_c < t_\gamma$:

  After an initial rise in the electron populations responsible for the X-ray and TeV emission, the populations reach a plateau and, due to their different energies and consequently lifetimes, fade on different time scales. Only high-energy electrons contribute to the observable X-ray emission while the VHE γ-ray emission stems

from low-energy electrons. In this stage, a positive scaling of the X-ray flux with $\dot{E}$ is expected. For typical characteristic ages of canonical pulsars that are larger than the synchrotron lifetime of X-ray-emitting electrons, a negative scaling of the X-ray emission with τ_c is expected. The cooling times for VHE-emitting electrons are on the other hand larger than the typical characteristic ages of canonical pulsars. The TeV emission builds up as sufficient amounts of low-energy electrons are accumulated, thereby tracing the history of particle injection into the PWN. Thus, the X-ray flux becomes rapidly fainter as the PWN grows older while the ratio of TeV-to-X-ray flux rises. The PWN is expected to be extended.

- $t_X < t_\gamma < \tau_c$:

  As the age of the system becomes significantly larger than the lifetime of X-ray emitting particles that are not further supplied by new particles as the pulsar has spun down significantly, the X-ray emission ceases. A relic PWN only visible in the VHE waveband is the result.

- $t_X < t_\gamma << \tau_c$:

  As the age of the system becomes significantly large all X-ray and VHE emission is too faint to detect. The particle populations are no longer supplied by the pulsar. The PWN has diffused out. The pulsar will no longer be visible unless effects such as confinement in strong shock driven by the pulsar's velocity as in bow shock nebulae set in.

This view is very simplistic as other properties such as the strength of the magnetic field in the PWN, the density of the surrounding medium or the energy output of the pulsar into the PWN also have great influence on the visible radiation. Recent time-dependent MHD simulations of the evolution of PWNe e.g. by de Jager et al. [2009] and Mayer et al. [2012], however, support the presented scenario.

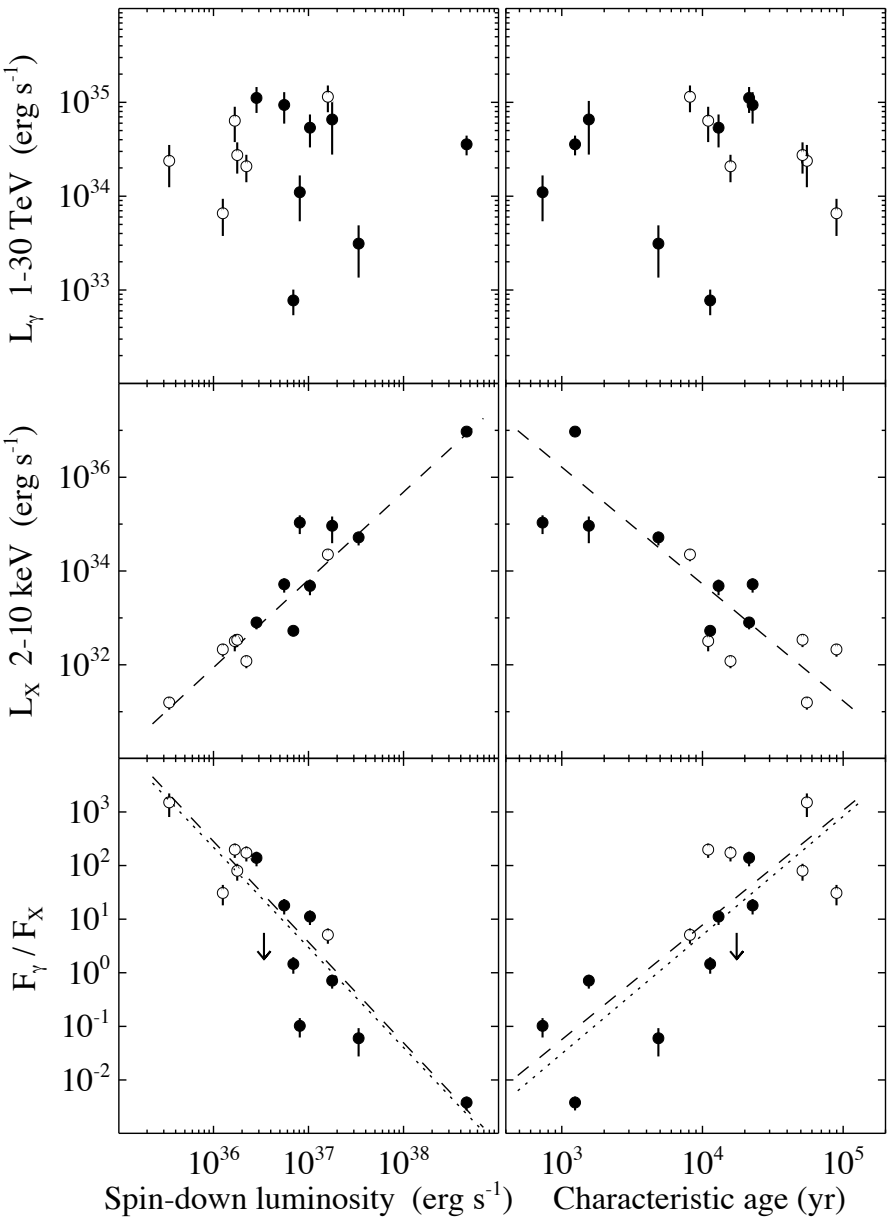

Figure 2.8 Correlation of the X-ray flux $F_{\rm X}$, VHE flux F_γ and the ratio of X-ray-to-VHE luminosity $L_{\rm X}/L_\gamma$ with the pulsar spin-down luminosity $\dot{E}$ and characteristic age $\tau_{\rm c}$. Full circles denote the already identified PWNe used in this study while open circles denote the PWN candidates. The corresponding fits are shown with dotted lines. Taken from Mattana et al. [2009].

3 Instrument and Analysis

The Earth is constantly hit by an isotropic flux of cosmic rays that covers an energy range of 10 orders of magnitude, from a few hundred MeV to at least $\sim 10^{20}$ eV. These cosmic rays consist mainly of protons and heavier nuclei, with small additions of electrons and positrons as well as neutrinos. While the charged cosmic rays are deflected in the galactic and extra-galactic magnetic fields and thus loose the directional information about their origin, photons can serve as messenger particles to search for astrophysical sources of high energy γ-rays. The photon flux is small compared to the flux of cosmic rays and becomes too small at energies above a few tens of GeV to be measured within a reasonable time span with collection areas in the order of $1\,\mathrm{m}^2$ (as typically used by satellite experiments). Thus, the Earth's atmosphere is used as a calorimeter in the *imaging atmospheric Cherenkov technique (IACT)*, giving effective detection areas in the order of $10^5\,\mathrm{m}^2$. In this approach, ground-based instruments are used to image the Cherenkov light emitted by extensive air showers which are initiated when the photon enters the atmosphere. The recorded images of the air shower can then be used to deduce the primary particle properties, such as direction and energy. An image analysis also allows the discrimination of photon-induced air showers from those initiated by the much more numerous background of cosmic-ray hadrons.

An overview on the properties of extensive air showers and their emitted Cherenkov light is given in Section 3.1. The *H*igh *E*nergy *S*tereoscopic *S*ystem (H.E.S.S.) experiment which employs the imaging atmospheric Cherenkov technique to detect photons in the energy range of 100 GeV up to 100 TeV is described in Section 3.2. The standard H.E.S.S. analysis chain applied to the recorded data is presented in Section 3.3. Parts of the data used in this thesis were taken in an alternative observation mode, the convergent pointing mode with a topological trigger as presented in Section 3.4, to lower the energy threshold of the instrument. The chapter concludes with a description of the timing analysis chain, applied to the data to search for pulsed emission from pulsars, in Section 3.5.

3.1 Extensive Air Showers

When a cosmic ray enters the Earth's atmosphere, it interacts with molecules and atomic nuclei in the air and thereby induces a cascade of secondary particles. The particles in the cascade carry most of the kinetic energy and momentum of the primary particle and continue to interact within the atmosphere, forming a so-called extensive air shower. In each interaction, the number of particles increases until reaching a maximum while the average energy per particle decreases to a threshold energy where no further shower

development takes place and the air shower eventually dies out.

The longitudinal extension of the air shower follows the initial direction of the primary particle and the overall particle number in the shower scales with the primary particle's energy, allowing for reconstruction of its direction and energy. In addition, the particle composition of the extensive air shower and its geometry depend on the type of the primary cosmic ray. Electrons and photons undergo electromagnetic interactions and thus induce an *electromagnetic air shower*. Air showers induced by hadrons evolve differently in the atmosphere. New particles such as pions and kaons are produced in interactions in the atmosphere that lead to hadronic sub-showers and a different composition and shape of *hadronic air showers*.

3.1.1 Electromagnetic Air Showers

An electromagnetic air shower, i.e. a cascade of particles induced by a photon or electron, evolves in the atmosphere via subsequent processes of bremsstrahlung and pair production. In each interaction step, a new generation of photons and electrons/positrons is produced and the particle number increases while the average energy per particle decreases. The cascade finally dies out when the average particle energy falls below 80 MeV, the critical energy in air where energy losses of electrons due to ionization of air molecules become comparable to bremsstrahlung losses. The electrons lose all of their energy before being able to produce another secondary photon. At this point, the number of secondaries has reached its maximum. The electrons are finally captured by ions in the atmosphere and the shower is absorbed. An electromagnetic cascade of particles, initiated by a 300 GeV photon, is shown in Fig. 3.1 (top,left).

The vertical extent of the shower is related to the energy of the primary particle and to the subsequent energy losses of the secondary particles. As the total depth of the atmosphere above sea level is greater than 20 times the mean free path length for a bremsstrahlung or pair production process, the shower will reach its maximum size well above sea level except for primary particles with energies above 100 PeV. As the secondary particles within the air shower are highly relativistic, the shower particles travel in a narrow front with a width of a few nanoseconds and the full shower develops within a few microseconds. The lateral spread of an electromagnetic air shower is predominantly determined by multiple Coulomb scattering of electrons and positrons off air nuclei. These showers are quite narrow and, on average, 90% of the shower particles stay at sea level within a cylinder around the shower axis with a radius of 60 m to 90 m, corresponding to one Moliére radius.

3.1.2 Hadronic Air Showers

In interaction of cosmic ray hadrons with atmospheric nuclei, new secondary hadrons, mainly pions and kaons, are produced that further interact or decay within the atmosphere. While charged pions decay into long-lived muons and neutrinos that escape the shower region, about one third of the newly produced hadrons are neutral pions that subsequently decay into two photons, initiating electromagnetic sub-cascades. Thus, in ad-

dition to an electromagnetic component, hadron-induced air showers have hadronic and muonic components where a significant part of the initial energy of the primary cosmic ray is absorbed. Such a hadron-induced particle cascade is shown in Fig. 3.1 (top,right).

Hadron-induced air showers reach their shower maximum [1] deeper in the atmosphere compared to electromagnetic air showers as the mean free path length is on average larger for hadrons than for photons or electrons. The lateral spread of hadronic air showers is larger than for electromagnetic air showers as the secondary hadrons formed in an hadronic air shower carry relatively large transverse momenta. In addition, the fluctuations in hadronic showers are larger than for electromagnetic showers due to the more complex interactions involved in the development of such showers. These features will be used subsequently in the analysis to discriminate electromagnetic from hadronic showers.

3.1.3 Cherenkov Light from Air Showers

Most of the secondary particles within the cascade of extensive air showers have a velocity v that is near the velocity of light c and greater than the speed of light in air c/n where n is the index of refraction in air. The charged particles emit Cherenkov radiation on their path through the atmosphere in a narrow cone with emission half-angle $\theta_c = \arccos(c/n\,v)$ along the particles direction. This Cherenkov emission can be recorded with imaging instruments located on ground. The amount of the emitted Cherenkov light as well as the emission angle of the Cherenkov light cone depend on the index of refraction n of air which is a function predominantly of emission height and of atmospheric conditions such as air pressure, temperature and water vapor content. The emission angle is $\sim 1.3°$ at sea level and decreases with emission height. As the shower particles and the light travel nearly at the same velocity, the Cherenkov light reaches ground level in an almost plane wave front with a width of a few nanoseconds regardless of its emission height. The Cherenkov light illuminates a circle on ground with a radius of 80 m to 150 m, the so-called Cherenkov light pool.

Figure 3.1 (left,bottom) shows the Cherenkov light pool of a photon-induced air shower. The Cherenkov light pool is homogeneous with a slight focusing on the outer rims which is the result of the changing emission angle with emission height. The different development of electromagnetic and hadronic air showers is also reflected in the distribution of Cherenkov photons on ground. Figure 3.1 (right,bottom) shows the Cherenkov light pool of a hadron-induced air shower. The Cherenkov light pool is illuminated more homogeneously for an electromagnetic air shower, while hadronic air showers lead to a larger spread in the distribution of Cherenkov photons with larger fluctuations from various electromagnetic and muonic sub-showers.

The Cherenkov spectrum falls from the ultraviolet to the visible wavelength range of 300 nm to 600 nm, typically collected by imaging atmospheric Cherenkov telescopes, as λ^{-2} where λ denotes the wavelength of the emitted Cherenkov light. As a result of the extinction of the Cherenkov light within the atmosphere due to absorption and scattering

[1] The atmospheric depth where the number of particles reaches its maximum is called shower maximum.

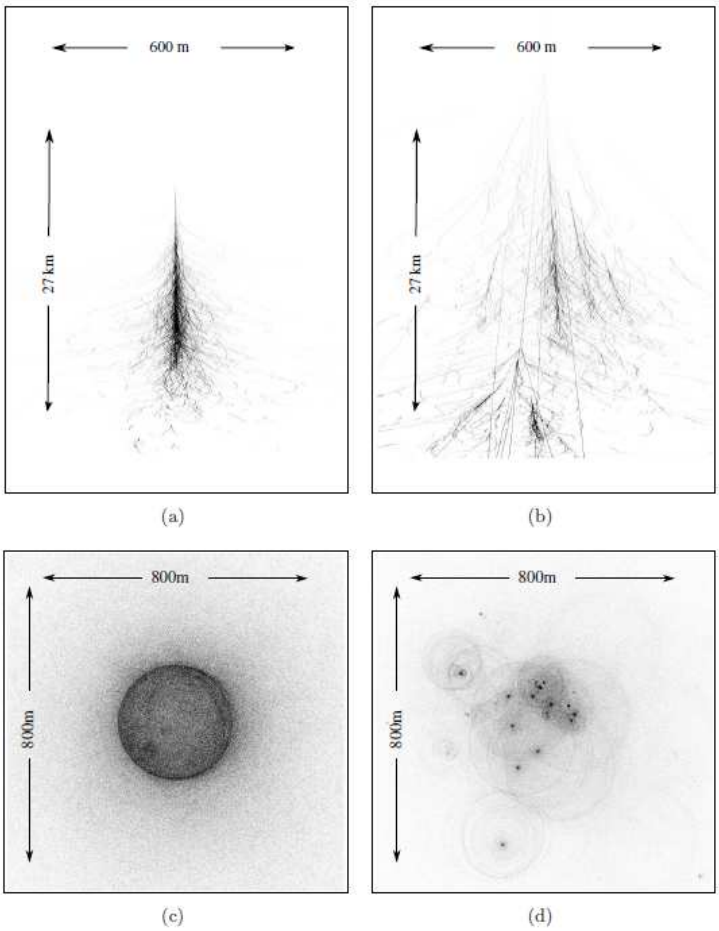

Figure 3.1 Development of an extensive air shower (top row) and its Cherenkov light pool (bottom row) of an air shower induced by a 300 GeV photon (left column) and a 1 TeV proton (right column). Images by courtesy of Konrad Bernlöhr.

on air molecules and aerosols, not all Cherenkov photons emitted by the shower will reach ground level. The maximum number of Cherenkov photons reaching ground level is in the blue visible wavelength range at $\sim 330\,\mathrm{nm}$. The density of Cherenkov photons at 2000 m above sea level is $\sim 100\,\mathrm{photons\,m^{-2}}$ ($\sim 6\,\mathrm{photons\,m^{-2}}$) for an air shower induced by a photon of an energy of 1 TeV (100 GeV). If the Cherenkov light has to traverse a larger air-mass on its way from the height of emission to the imaging detector, due to e.g. an increased distance of the detector to the impact point of the shower on ground or a larger zenith angle of observation, the density of Cherenkov photons on ground becomes correspondingly smaller.

3.2 H.E.S.S. Instrument

The *H*igh *E*nergy *S*tereoscopic *S*ystem (H.E.S.S.) experiment employs the *imaging atmospheric Cherenkov technique (IACT)* with *stereoscopic view* to detect air showers induced by photons in the energy range of 100 GeV up to 100 TeV. In this approach, imaging telescopes with large reflectors are located in the Cherenkov light pool of extensive air showers and are used to collect and image the Cherenkov photons onto a fast recording camera. The low duty cycle due to limited operation only in moonless nights and the small field of view of IACT telescopes compared to satellite-based observatories is compensated by the large detection area of the ground-based instruments. [2]

3.2.1 Site

The H.E.S.S. instrument is located in the Khomas Highland of Namibia, at (23°16′18″S, 16°30′00″E) and an altitude of 1800 m above sea level. The site was chosen for its good conditions for astronomical observations such as long periods of cloudless nights and a clean atmosphere with small light pollution due to terrestrial light sources. The relative humidity is below 90% throughout most parts of the year allowing for operation of the sensitive cameras at high voltages. In addition, the site allows for the observation of the southern hemisphere, especially the Galactic Center, at low zenith angles during culmination.

3.2.2 Telescopes

The H.E.S.S. instrument consists of four identical telescopes, arranged in a square of 120 m side length. A picture of the array is given in Fig. 3.2. The spacing was chosen in order to allow for a simultaneous view of the Cherenkov light emitted by a photon-induced air shower by at least two telescopes while keeping a maximum distance between the telescopes for good stereoscopic viewing conditions. A telescope consists of a camera located in the focal plane of a reflector mounted on a steel support structure. The optical reflector is of Davies-Cotton type [Davies and Cotton, 1957] and consists of 382 round mirrors of 60 cm diameter each, arranged on a sphere with a radius equal to the 15 m focal length of the reflector. The total reflector has a flat-to-flat diameter of 13 m and an area of 107 m^2 with an imaging accuracy of 0.03° on axis and 0.06° for photons at 2° off axis. The telescopes can be pointed at any position in the sky using an altitude-azimuth mount that allows for movement in all directions with a maximum slewing speed of 100 ° min^{-1}. A more detailed overview on the H.E.S.S. telescopes and their optical reflector can be found in Bernlöhr et al. [2003] and Cornils et al. [2003].

[2] Other ground-based detection techniques can be found in Cronin et al. [1993] (Air Shower Technique) and Smith [2006] (Solar Array Technique)

Figure 3.2 Picture of the H.E.S.S. array.

3.2.3 Camera

The camera consists of 960 photo-multipliers (PMTs) with a solid angle of 0.16° each, giving a total camera field of view of 5° (full opening angle), The PMTs provide a response time of a few nanoseconds, a quantum efficiency of 20%-30% in the wavelength range $300 - 700\,\mathrm{nm}$ and allow the conversion of Cherenkov photons to photo-electron equivalents (ph.e.) in the dynamical range of 1 to 1600 ph.e. A group of 16 PMTs are arranged in a so-called drawer that contains the electronics for triggering and data read-out as well as the high voltage supply. To increase the light yield, Winston cones are mounted in front of the camera to focus the incoming light onto the active area of PMTs. A more detailed overview on the mechanics and electronics of the H.E.S.S. camera can be found in Punch and H.E.S.S. Collaboration [2001] and Vincent et al. [2003].

3.2.4 Trigger

The H.E.S.S. trigger system, as described in detail in Funk et al. [2004], consists of a two level system. At the first level, the telescopes initiate a trigger signal individually based on the information registered in the camera. The camera is subdivided into 38 overlapping trigger sectors with 64 PMTs each to give an homogeneous trigger efficiency over the entire camera. A telescope trigger decision is formed when a signal above the critical threshold of $5.3 ph.e.$ (PMT threshold) is seen in at least 3 PMTs (sector threshold) within one trigger sector and time window of $1.5\,\mathrm{ns}$. At the second trigger level, it is demanded that at least two telescope trigger signals, sent to the central trigger via optical fibers, were initiated within a time window of $80\,\mathrm{ns}$ (telescope multiplicity). With the second step, it is not only assured that the air shower event is recorded in stereoscopic mode, but that also the rate of random triggers due to night sky background and Cherenkov light from local muons is greatly reduced at the hardware level.

After a trigger decision has been formed, a unique event number is assigned to each recorded air shower and distributed to all cameras. The data of each event, temporarily

stored in an analogue ring buffer in each camera, is read out and stored on the computer farm for later processing. The central trigger also logs the current read-out status of the cameras and thus allows for measurement of the system dead-time. To each individual event, a GPS time stamp is assigned by the central trigger, delivered by a Cesium atomic clock that is synchronized to the GPS system using a *GPS167 Meinberg* GPS receiver. The long term stability of the time system was shown to be less than $2\,\mu$s.

The trigger system is highly flexible and the values (PMT threshold, sector threshold and telescope multiplicity) used to form a trigger decision can be adjusted via a database. The standard values for the PMT and sector thresholds have been chosen in order to balance the minimum Cherenkov light needed for triggering and the amount of dead-time imposed on the system as well as the suppression of accidental background triggers.

3.2.5 Data Taking and Acquisition

Data are taken in units of so-called runs with a duration of 28 minutes each. In the standard observation mode, the telescope axes are pointed parallel and are targeted at a given sky position, following its movement on the firmament. Typically, the data are taken in *wobble mode*, where the putative γ-ray source is displaced by some offset from the camera center to allow for a background estimation from the same field of view. Different modes of operation are possible, employing alternative pointing modes and trigger algorithms. One of these modes, the convergent pointing mode with a topological trigger, will be discussed in Section 3.4.

3.3 Data Analysis

After the events have been synchronized and built on the computer farm, they are collected and stored in individual raw data files with a unique run number. These files are subsequently shipped to Europe for further processing and analysis. The analysis chain consists of calibration, event reconstruction, γ-hadron separation and signal extraction. The individual steps are explained in more detail in the following.

3.3.1 Calibration

For calibration and further analysis, only those data are considered that meet certain data quality criteria to avoid unreliable analysis results due to e.g. malfunctioning hardware or poor observation conditions. A changing absorption of the atmosphere due to e.g. clouds moving through the field of view of the telescopes or a layer of dust in some height above the telescopes can lead to wrong flux measurements from a γ-ray source. Cuts on the absolute trigger rate and its variation are used to identify those runs affected by an unstable atmosphere. Another important criterion is a stable sensitivity of the camera for recording Cherenkov light. The variations in the numbers of PMTs turned off due to e.g. bright stars in the field of view or lightning on the horizon as well as technical problems is required to be less than 10%. More details can be found in Aharonian et al. [2006d].

The data passing the quality criteria are then calibrated in a standard calibration chain as detailed in Aharonian et al. [2004b], using calibration coefficients collected from dedicated calibration runs and the data itself. In this procedure, the response of the cameras and individual PMTs to Cherenkov light are estimated. The optical response of the telescopes, which is slowly decreasing with time due to e.g. decreasing reflectivity of the mirrors, is estimated from Cherenkov light emitted by local muons present in the data [Bolz, 2004] and is used to correct the estimated energy of the photon candidates.

3.3.2 Event Reconstruction

The calibrated data are used to estimate the properties of the primary photon such as its arrival direction and energy. In this thesis, the approach of the so-called Hillas parametrization [Hillas, 1985] was used. To significantly improve the parametrization procedure, the recorded shower images are subjected to a tail-cut cleaning procedure that for each image separates PMTs with a likely Cherenkov light signal from those most likely containing noise due to e.g. night sky background light. Only data from PMTs that contain at least 10 ph.e. with a neighboring PMT with at least 5 ph.e. are kept together with PMTs of $5-10$ ph.e. if they have a neighbor with at least 10 ph.e.. All other PMT data is removed from the camera image. The cut values have been chosen to ensure good signal separation while keeping faint images.

The cleaned image of the Cherenkov light of a photon-induced shower has an approximately elliptical shape. The distinctiveness of the elliptical shape depends on many properties such as the viewing angle of the telescopes relative to the shower axis, the distance of the shower axis to the telescopes as well as energy and type of the primary particle. The images are parametrized by the method of Hillas [Hillas, 1985] and the Hillas parameters are (see also Fig. 3.3):

- nominal distance D (angular distance between the center of gravity of the image and the camera center)
- length L and width W of the ellipse
- image amplitude IA (or image size)
- orientation of the major axis within the camera plane.

The Hillas parameters are used to derive the arrival direction and energy of the primary particle and to separate photon-induced showers from hadron-induced showers. Cuts on the minimum image amplitude and on the maximum nominal distance are used to reject badly reconstructed images or images that have been truncated at the edge of the camera. A minimum of two images per event passing these cuts are required for stereoscopic event reconstruction.

The major axis of the Hillas ellipse in the camera plane points towards the origin of the shower on one side and towards the impact point of the shower on the ground on the other side. In stereoscopic mode, the shower images are superimposed in a common field

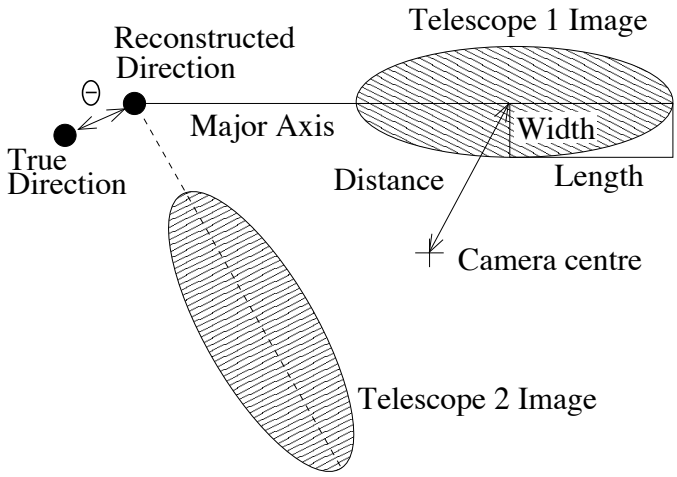

Figure 3.3 Sketch of Hillas parameters and direction reconstruction using a stereoscopic view of the shower from two telescopes. Taken from Aharonian et al. [2006d].

of view to give the arrival direction of the incident photon. A sketch of the algorithm is given in Fig. 3.3 for a superposition of two camera images. The direction of the incident photon is estimated from a weighted average of the intersection of all pairs of major axes of the ellipses. The angular resolution is typically around 0.1° on an event-by-event basis. The impact point of the shower on the ground is calculated from a similar algorithm from the intersection of the shower axes, projected in a plane perpendicular to the respective telescope's pointing direction and superimposed in a common coordinate system. The resolution of the estimated impact point is better than 15 m. The energy of the shower is estimated using Monte Carlo simulations of the Cherenkov emission from extended air showers initiated by photons and the detector response that gives the reconstructed shower energy in dependence of the total image amplitude, the impact parameter (distance between shower impact point and telescope), zenith angle and offset angle of the shower. The reconstructed energy is corrected for the changing optical efficiency of the detector by a simple scaling of the energy by the ratio of the actual optical efficiency (estimated from local muons as pointed out in Section 3.3.1) and the simulated optical detector response. The resolution of the estimated energy is better than 15%.

3.3.3 Event Selection

The more variable development of hadronic air showers result in shower images that are more irregular in shape than observed for photon-induced air showers. These differences in the shape of the shower images of photon- and hadron-induced air showers are used to discriminate between photons and hadronic background. In this method, a weighted combination of mean-reduced-scaled parameters $MRSP$ are calculated from the width

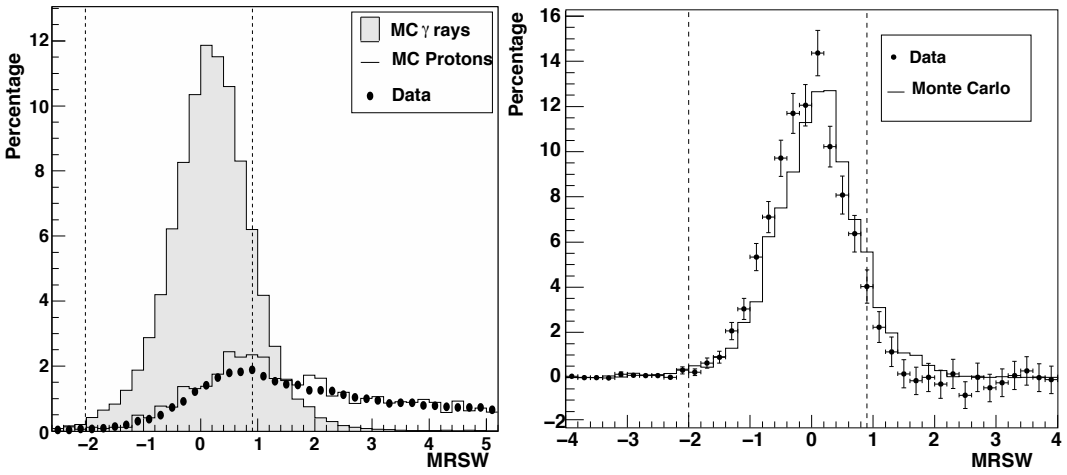

Figure 3.4 *Left:* Distribution of mean reduced scaled width and for signal and background events (points), simulated photons from a point-like source (shaded histogram) and simulated protons. *Right:* Distribution of mean reduced scaled width of excess events (points) and simulated photons from a point-like source (histogram). Taken from Aharonian et al. [2006d].

W and length L parameters of the individual telescopes as

$$\mathrm{MRSP} = \frac{1}{N_{\mathrm{tel}}} \sum_{N_{\mathrm{tel}}} \frac{P - < P > (IA, Z, IP)}{\sigma_{\mathrm{P}}(IA, Z, IP)}, \tag{3.1}$$

where N_{tel} is the number of telescopes with a shower image, P the parameter W or L, $<P>$ and σ_{P} the mean value and its variance as estimated from Monte Carlo simulations of photon-induced air showers for a given image amplitude IA, zenith angle Z and impact parameter IP.

The distribution of $MRSW$ is shown for signal and background events in Fig. 3.4 (left) together with real background data. Selection of a range in $MRSW$ and $MRSL$ as expected for photon-induced air showers leads to a rejection of hadron-induced air showers. Figure 3.4 (right) shows the distribution of $MRSW$ for images of photon-induced air showers after applying selection cuts on $MRSL$ together with signal evens from a γ-ray source. As the background of cosmic rays is isotropic, a cut on the angular distance θ between the reconstruction shower direction and the nominal source position can be used to further reduce the background of cosmic rays. The cut on the angular distance depends on the angular resolution and assumed source extension.

The optimum values for the selection cuts have been found a priori in an optimization procedure for maximum expected significance per square-root hour of observation time using data from a simulated γ-ray source for the signal and from measurements of sky regions with no known γ-ray source for the background events. The selection cuts depend on the assumed extension and spectrum of the γ-ray source and the different sets of cuts

used in this thesis are:

- *Hard selection cuts* are optimized for faint sources with a flux of 1% of that of the Crab nebula and a power-law spectrum with a photon index of 2.0. Due to the good angular resolution, these cuts are used mainly for morphology studies.
- *Standard selection cuts* are optimized for stronger sources with a flux of 10% of that of the Crab nebula with a power law spectrum with a photon index of 2.6. These cuts are used mainly for spectral studies.
- *Soft (or loose) selection cuts* are optimized for bright sources with a flux of 100% of that of the Crab nebula and a power law spectrum with a photon index of 3.2. These cuts are used mainly for spectral studies with a low energy threshold.
- *Low energy selection cuts* are optimized for sources with a flux of 10% of that of the Crab nebula with a steep power law spectrum with a photon index of 5 for energies below 500 GeV. These cuts result in a lower energy threshold compared to the standard cuts at the expense of a worse background rejection efficiency.

The different sets of cuts are described in more detail in Aharonian et al. [2006d] and Aharonian et al. [2007].

3.3.4 Background Estimation and Signal Extraction

To extract a signal from the remaining γ-ray-like events, an estimation of the irreducible background is needed. Therefore, the number of γ-ray-like events N_{on} from a circular region around the putative γ-ray source (signal or ON region) are compared to the number of γ-ray-like events N_{off} from regions within the same field of view without any known γ-ray source (background or OFF regions). The size of the signal region depends on the angular resolution and assumed source size. For point-like sources, the size of the signal region is adjusted according to the angular resolution of the employed selection cuts and is in general slightly larger than the H.E.S.S. point spread function (defined by a 68% containment radius) for that particular set of cuts. The number of excess events N_{ex} is

$$N_{\mathrm{ex}} = N_{\mathrm{on}} - \alpha \times N_{\mathrm{off}} \tag{3.2}$$

and its error

$$u(N_{\mathrm{ex}}) = \sqrt{N_{\mathrm{on}} + \alpha^2 \times N_{\mathrm{off}}} \tag{3.3}$$

where α is a normalization factor that accounts for the differences of signal and background regions in terms of size and acceptance of the camera to photons. The statistical

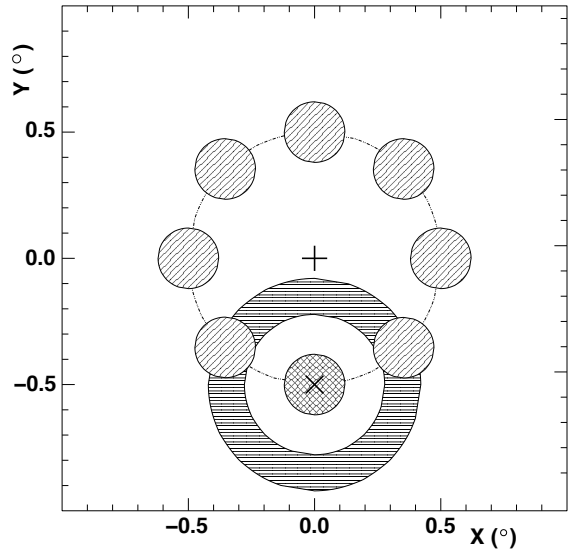

Figure 3.5 Ring and reflected region background method. The camera center is marked with + while the signal region is marked with **x**. The dark gray shaded ring denotes the area used for background estimation in the ring background method and the seven circular off regions of the reflected region background method are indicated by light gray circles. Taken from Aharonian et al. [2006d].

significance S of the estimated excess in the signal region is calculated, according to Li and Ma [1983], as

$$S = \sqrt{2}\left(N_{\mathrm{on}}\ln\left[\frac{(1+\alpha)}{\alpha}\left(\frac{N_{\mathrm{on}}}{N_{\mathrm{on}}+N_{\mathrm{off}}}\right)\right] + N_{\mathrm{off}}\ln\left[(1+\alpha)\left(\frac{N_{\mathrm{off}}}{N_{\mathrm{on}}+N_{\mathrm{off}}}\right)\right]\right)^{1/2}. \quad (3.4)$$

A statistical significance of at least 5σ after trial factors is required for a firm detection of any γ-ray source.

Various methods can be used to estimate the number of background events N_{off} and normalization factor α as e.g. detailed in Berge et al. [2007]. A sketch of the two methods used in this thesis is given in Fig. 3.5 where the circular signal region is marked with an x.

In the *ring background method*, the background is estimated from a ring centered on the signal region (dark gray area in Fig. 3.5). The inner radius of the ring is chosen such that no contamination from the signal region is expected. The area of the background region is chosen to be larger than the area of the signal region to minimize any statistical fluctuations. As the background region contains areas of different distance to the camera center, the normalization factor α has to take the changing camera acceptance into account. This background estimation method is very flexible and can be used to

calculate the excess for each point in the field of view. Although the background is then highly correlated within the field of view, this method is well suited for the study of the morphology of a γ-ray source.

In the *reflected-region background method*, the background is estimated from regions with the same offset from the camera center and with the same size as the signal region (light gray areas in Fig. 3.5). Therefore, the background regions have the same camera acceptance and the normalization factor α is simply the inverse of the number of background regions. This background estimation method is used in this thesis for the study of the spectrum of a γ-ray source.

3.3.5 Effective Area and Energy Threshold

The effective detection area of the H.E.S.S. telescope system is defined as the area perpendicular to the pointing direction in which the array is able to detect γ-rays. The effective area depends on the sensitivity of the individual telescopes to the Cherenkov light yield from the shower, the layout of the array in stereoscopic mode and the shower properties such as energy, zenith and offset angle. Lastly, the effective area also depends on the selection cuts used for the analysis. The effective areas in dependence of the photon energy are calculated from Monte Carlo simulations of a point-like γ-ray source and are shown in Fig. 3.6 (left) for one set of selection cuts and different zenith angles in dependence of the true (simulated) energy. The effective area decreases rapidly at the energy threshold of the instrument and is otherwise approximately constant for a wide energy range. The rapid drop at the low energy end moves to higher energies when the zenith angle increases as the showers and their respective Cherenkov light have to traverse a larger path through the atmosphere to reach the telescopes.

The effective areas can be used to define the energy threshold of the instrument, the so-called peak-rate energy threshold. When the effective area is folded with a power law, most commonly the spectrum of the Crab nebula with a photon index of 2.69 is used, the energy of the maximum of the resulting γ-ray rate is defined as the peak-rate energy threshold and is shown in Fig. 3.6 (right) for different sets of selection cuts as a function of the zenith angle. Another definition of the energy threshold, the so-called safe analysis threshold, is based on the requirement that the energy bias is less than 10%. The safe analysis threshold is indicated with a vertical line in Fig. 3.6 (left) and is slightly higher than the peak-rate energy threshold.

3.3.6 Spectrum and Integral Flux Measurement

Various methods are available for the generation of a differential γ-ray spectrum of a source. The methods are described in detail in Aharonian et al. [2006d] and in Hoppe [2008]. In the following, an overview on the 'Method A' (or bin-weighted method) of Hoppe [2008] will be given as this method is used throughout the thesis to derive the spectrum of steady VHE γ-ray emission. In this method, the event counts from the signal and background region, N_{on} and N_{off}, respectively, are filled in finely binned histograms in dependence on the logarithm of the reconstructed event energy. For each energy bin,

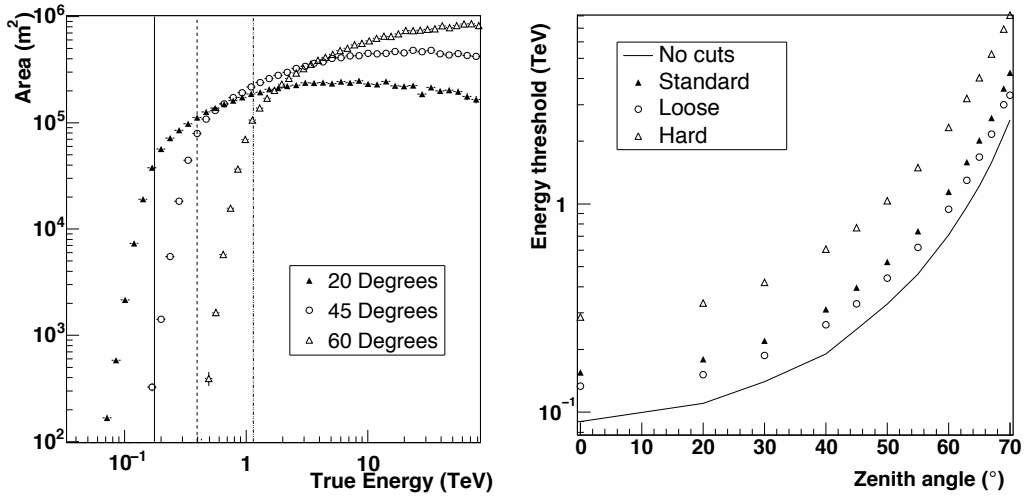

(a) **(b)**

Figure 3.6 *Left:* Effective areas for *standard selection cuts* in dependence of the true energy for different zenith angles. The safe analysis threshold is indicated with a vertical line. *Right:* Peak-rate energy threshold for different sets of cuts and zenith angles. The safe energy threshold is slightly higher. Taken from Aharonian et al. [2006d].

the run-wise mean effective area A_{eff} is calculated for the distribution of zenith angles ϕ and offset angles θ of the events. The background normalization factor α and the energy thresholds for each run are taken into account. The run-wise effective area is then multiplied by the live time T of the observation, yielding the so-called exposure $(T\,A_{\mathrm{eff}})$. The run-wise histograms of N_{on}, N_{off} and $(T\,A_{\mathrm{eff}})$ are then combined to obtain histograms which are valid for the whole data set. As the initial binning is usually too fine for the available statistics, the histograms are rebinned to give broader bins. For the spectra presented in this thesis, the bin size is set to a fixed value that was chosen by hand to give a good compromise between the total number of bins and the significance per bin. The differential γ-ray flux in each energy bin i with width $\Delta\,E_{\mathrm{i}}$ is calculated as

$$\left(\frac{dN}{dE}\right)_{\mathrm{i}} = \frac{N_{\mathrm{on,i}}}{\Delta\,E_{\mathrm{i}}} \sum_{\mathrm{runs}} \left(\frac{1}{T\,A_{\mathrm{eff}}}\right)_{\mathrm{i}} (\phi,\theta) - \frac{N_{\mathrm{off,i}}}{\Delta\,E_{\mathrm{i}}} \sum_{\mathrm{runs}} \frac{1}{\alpha_{\mathrm{run}}} \left(\frac{1}{T\,A_{\mathrm{eff}}}\right)_{\mathrm{i}} (\phi,\theta). \tag{3.5}$$

For broad bin sizes and correspondingly large event statistics in each bin, the error of the flux is expected to be approximately Gaussian and the error for each flux point is calculated using Feldman and Cousins [1998] with a 68% confidence level. In the absence of any γ-ray signal, the flux points in Eq. 3.5 are replaced by an upper limit calculated according to Feldman and Cousins [1998] using a 95% confidence level.

Using a χ^2-minimization procedure, the differential flux points are fitted by a function

for the expected spectrum, typically a power law of form

$$\frac{dN}{dE} = I_0 \left(\frac{E}{\mathrm{TeV}} \right)^{-\Gamma}, \tag{3.6}$$

with the normalization factor I_0 and photon index Γ. Although the effective area used in the calculation of the differential flux depends on the photon index, the effect is small for an index of less than 3.0 and, in this case, can be ignored.

The total integral flux F_γ in the energy range E_{min} and E_{max} for a power law spectrum can be calculated as

$$F_\gamma = \int_{E_{\mathrm{min}}}^{E_{\mathrm{max}}} I_0 \left(\frac{E}{\mathrm{TeV}} \right)^{-\Gamma} dE, \tag{3.7}$$

the total integral energy flux G_γ accordingly as

$$G_\gamma = \int_{E_{\mathrm{min}}}^{E_{\mathrm{max}}} I_0 \left(\frac{E}{\mathrm{TeV}} \right)^{-\Gamma} E\, dE \tag{3.8}$$

and the luminosity L_γ for a distance d is given by

$$L_\gamma = 4\pi\, d^2\, G_\gamma. \tag{3.9}$$

3.4 Alternative Observation Modes

The H.E.S.S. experiment helped to establish a wealth of astrophysical sources in the energy range from 100 GeV up to 100 TeV. Some astrophysical phenomena are known to be accessible only at or below the H.E.S.S. energy threshold. These phenomena include e.g. pulsars that show spectra with a cut-off well below 100 GeV. Indeed, recent observations with new satellite experiments such as *FERMI* and *AGILE*, operating in the energy range from MeV up to 300 GeV, produced numerous detections of pulsars in the GeV energy range. As already noticed in the review by Weekes [1988], the energy threshold of IACTs E_{T} is mainly governed by the minimum detectable Cherenkov light yield of photon-induced air showers and scales as

$$E_{\mathrm{T}} \propto \frac{NSB\, \Omega\, \tau}{A_{\mathrm{M}}\, \epsilon} \tag{3.10}$$

where NSB denotes the night sky background light, Ω the solid angle of the PMTs, τ the integration time, A_{M} the mirror area and ϵ the quantum efficiency of the PMTs. The MAGIC collaboration used a single imaging Cherenkov telescope having a large 17 m diameter reflector equipped with a camera with high quantum efficiency PMTs to reduce the energy threshold well below 100 GeV.

A different approach will be presented here for the H.E.S.S. experiment to increase the number of collected Cherenkov light photons from low energy γ-ray showers and to reduce the energy threshold while keeping the instrumental setup, i.e. mirror and

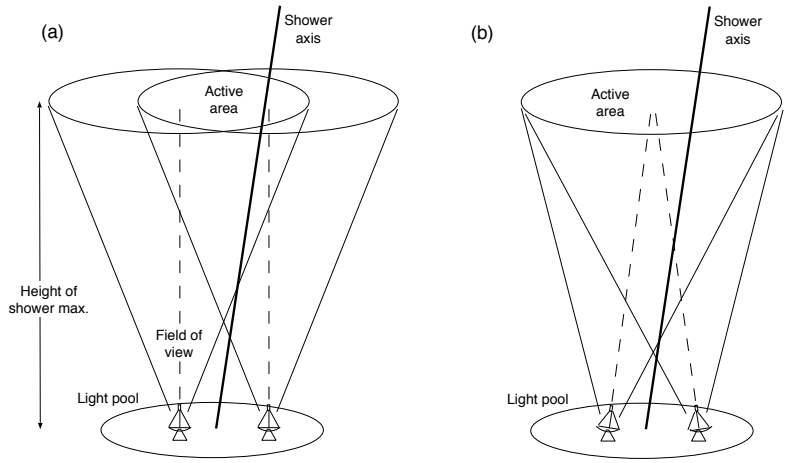

Figure 3.7 Sketch of a two telescope array geometry for standard (left) and convergent pointing (right), taken from Lampeitl et al. [2000].

camera, of the current experiment. In this approach, first introduced by the HEGRA collaboration [Lucarelli et al., 2003], an alternative trigger logic (the *topological trigger*) will be used in conjunction with an alternative tracking scheme (the *convergent pointing*). In this section, a short overview of the alternative observation mode will be presented. More details can be found in Fuessling [2006].

3.4.1 Convergent Pointing

The convergent pointing was introduced by the HEGRA collaboration [Lampeitl et al., 2000]. The geometry of the standard pointing mode (SM, left) and the convergent pointing mode (CP, right) is illustrated for two telescopes in Fig. 3.7. In standard mode, the telescopes are aligned parallel to each other, pointing at a given position in the sky. In convergent mode, the telescope axes are canted in such a way that they intersect at the atmospheric depth of maximum Cherenkov photon emission of γ-ray showers of a certain energy. The line connecting the center of the telescope array and the intersection point is directed towards the target position on the sky. For observations presented throughout this thesis, an atmospheric depth of $270\,\mathrm{g\,cm^{-2}}$ was chosen, corresponding to the maximum shower development of a photon-induced shower of an average energy of 100 GeV. This atmospheric depth translates into a height of 8.7 km above the H.E.S.S. site for observations at zenith.

In the imaging process of the shower, the atmospheric depth of the shower maximum translates into a shift of the image centroid in the camera plane from the nominal source position. As can be seen in Fig. 3.8, the convergent pointing shifts the image centroids towards the nominal pointing position. The convergent pointing thus leads to an enhancement of the shower images within a certain region in the camera plane surrounding the nominal pointing position. This makes the selection of an area within the camera where the images of low energy γ-ray showers are expected easier. In addition,

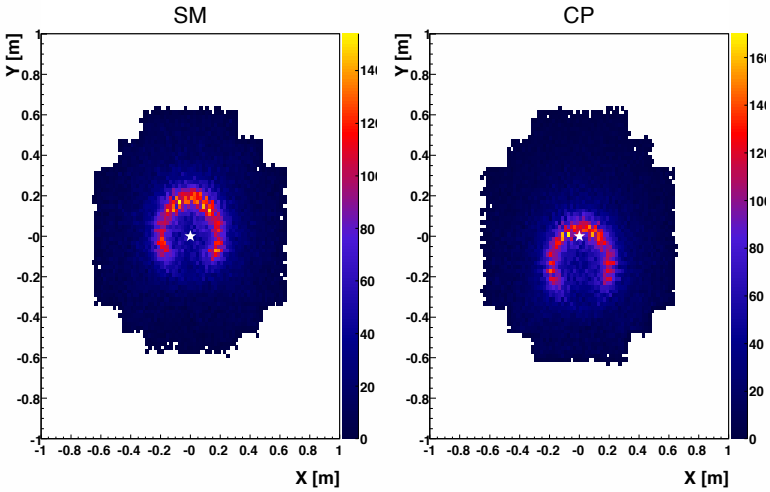

Figure 3.8 Centers of gravity of a simulated γ-ray point source located at 0.0° offset and 20° zenith angle for one telescope. The camera center is marked with a white star.

fewer shower images are truncated at the edge of the camera.

The overlap of the field of view of different telescopes is maximized at the height of maximum shower development of low energy γ-ray showers and makes the detection of such air showers by multiple telescopes more likely (see also Fig. 3.9 (top)). As the most luminous region of a 100 GeV shower is optimally viewed by all telescopes, the convergent pointing maximizes the total number of collected photons from low energy showers, at the expense of overall detection area. Figure 3.9 (bottom) shows the effective collection areas for *standard selection cuts*. As the shift of the image centroids is small for low energy showers, an increased detection efficiency can be seen only for low-energy showers at large offsets. A similar angular resolution and energy resolution as in parallel pointing mode has been found for the observation mode with convergent pointing in studies using Monte Carlo simulations. The standard H.E.S.S. analysis chain has been tested with observations on the Crab nebula (see Fuessling [2006] for more details).

3.4.2 Topological Trigger

The topological trigger was developed by the HEGRA collaboration [Lucarelli et al., 2003]. In this approach, it is attempted to lower the amount of Cherenkov photons needed to trigger the camera. In this trigger mode, the PMT threshold is thus lowered to collect more Cherenkov photons from such low energy showers and detect fainter shower images while keeping the random trigger rate due to e.g. night sky background stable. Low energy showers have a small number of Cherenkov photons at rather small distances from the shower core. Thus, only showers with a small distance to the telescopes and in a certain area within the array near its center have a sufficient Cherenkov light yield to trigger the telescopes. Images of low energy showers are expected only in specific

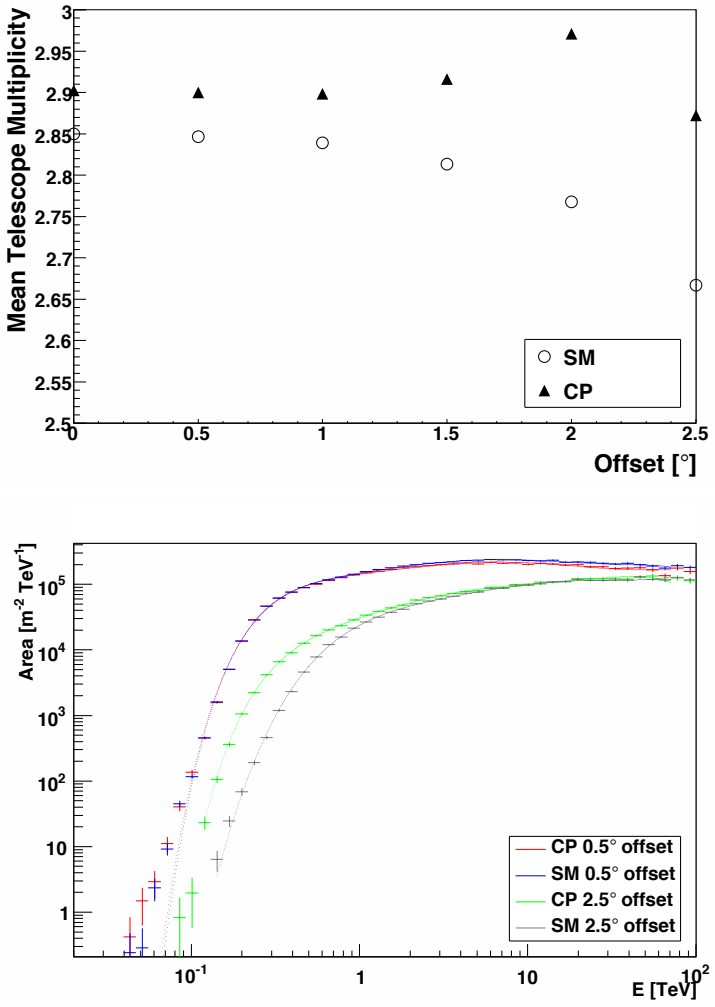

Figure 3.9 Top: Mean telescope multiplicity for a simulated γ-ray point source located at a zenith angle of 20° and various offsets. Bottom: Effective areas for the standard observation mode (SM) and the observation mode with convergent pointing (CP) for a simulated γ-ray point source located at 20° zenith angle for two different offsets using *standard selection cuts* for γ-hadron separation.

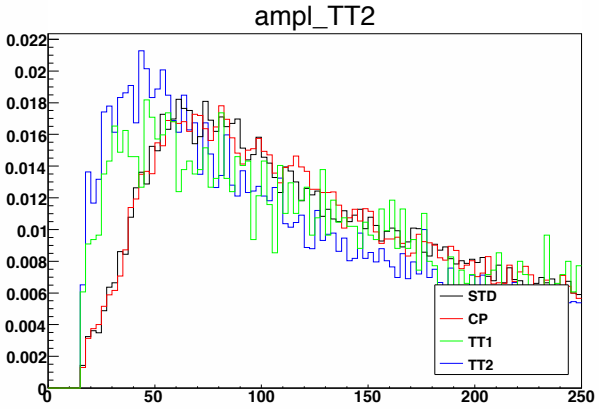

Figure 3.10 Normalized distribution of the image amplitude for a simulated γ-ray point source located at 0.5° offset and 20° zenith angle for the standard observation mode (SM), the observation mode with convergent pointing (CP) and the observation mode with convergent pointing and a topological trigger with a trigger area of 1.5° (TT1) and 0.8° (TT2). Please note that the TT2 observation mode has not been used for data taking and is further not discussed. No image selection cuts are applied.

areas in the camera plane. In the topological trigger, it is possible to restrict the active area within the camera that takes part in forming a trigger decision to that part of the camera where the image centroids of low energy showers are expected.

For the observations with a topological trigger with convergent pointing presented in this thesis (TT1), a circular region with a radius of 1.5° centered on the camera center was used. Only those PMTs within the active region, i.e. 280 PMTs out of a total of 960 PMTs, take part when a trigger decision is formed. As less combinations of PMTs forming a trigger decision are possible, the camera trigger rate is greatly reduced. This allows for reducing the PMT threshold to 4 ph.e. (standard value is 5.3 ph.e.) again increasing the trigger rate. Both effects lead to a stable trigger rate whereas a reduction of the PMT threshold to a value below 4 ph.e. in standard mode already leads to a significant increase in trigger rate and consequently in dead-time of the system [Funk et al., 2004]. In the case a trigger decision is formed, data from all PMTs in the camera is readout for later analysis.

The trigger mode has been studied using Monte Carlo simulations where the detector response was simulated with a reduced optical efficiency of 70%. The optical efficiency has been reduced to more closely match the true optical efficiency of the system at the time of the Monte Carlo production in the year 2006. Figure 3.10 shows the distribution of the size of images of simulated γ-ray showers triggering the H.E.S.S. experiment in the different observation modes. It can be seen that a detection of fainter images results for the observation mode with a topological trigger. For further analysis of the data taken in this mode, *soft selection cuts* with a cut on the minimum image size of 40 ph.e.

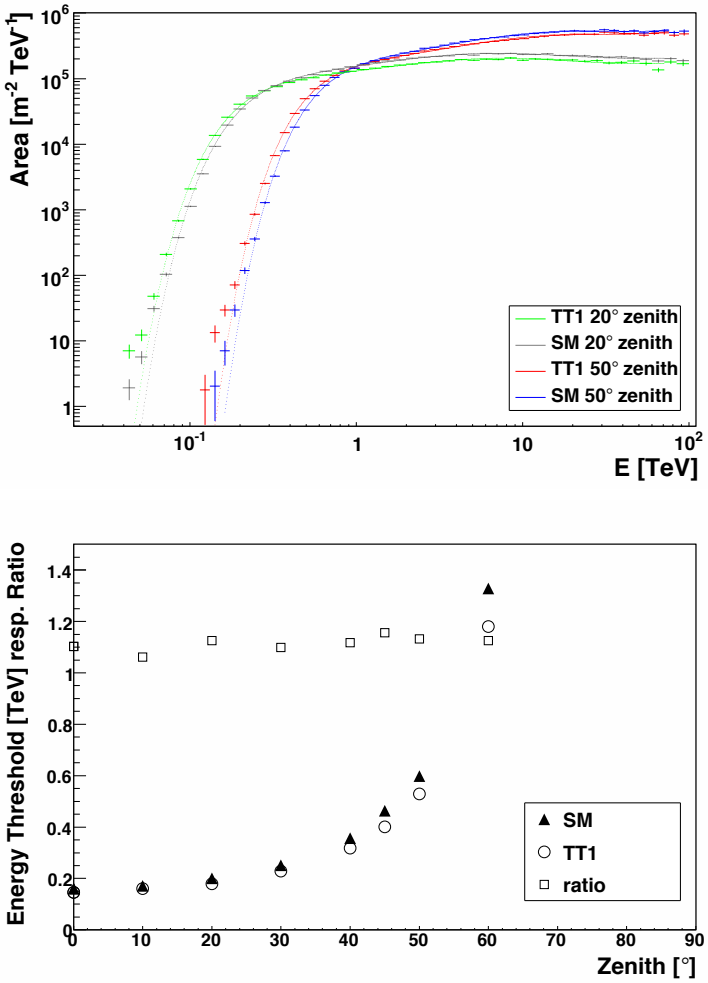

Figure 3.11 Top: Effective areas for standard observation mode (SM) and the observation mode with convergent pointing and a topological trigger (TT1) for simulated γ-ray point source located at 0.5° offset and two different zenith angles using *soft selection cuts* for γ-hadron separation. Bottom: Peak-rate energy threshold for the two observation modes SM and TT1 together with its ratio calculated as SM/TT1 for a simulated γ-ray point source located at 0.5° offset and various zenith angles using *soft selection cuts* for γ-hadron separation.

compared to 80 ph.e. in the *standard selection cuts*-based analysis have been used so that fainter images are not discarded during event selection. The resulting effective detection areas (shown in Fig. 3.11 (top)) show an increase in detection efficiency for low energy showers (below 1 TeV) at the expense of detection efficiency for high energy showers (above 1 TeV) as expected. The resulting peak-rate energy threshold (shown in Fig. 3.11 (bottom) for 0.5° offset and 20° zenith angle) is lowered by 10% in topological trigger mode compared to the standard mode. It has to be noted that any further decrease of the optical efficiency of the system over time lessens the effect of the reduced trigger threshold for the data sets presented in this thesis.

3.5 Timing analysis

A time series analysis with *epoch-folding* is applied to the γ-like events, selected from the direction of the pulsar, to search for periodicity in the event arrival times. This analysis makes use of the already known rotational spin-down behavior of the pulsar, described by a timing model obtained from observations in other wavebands than the VHE band such as the radio, X-ray or HE band. This method is more sensitive for searches of periodicity from known pulsars when compared to analysis methods such as blind search techniques (e.g. Atwood et al. [2006]) where no a priori information on the pulsar spin-down behavior is used. The timing analysis comprises several steps that are detailed in this section. After transforming the photon arrival times to the reference frame of the pulsar (see Section 3.5.1), the corrected arrival times are related to the pulsar period of rotation (see Section 3.5.2), and finally searched for periodicity with several statistical tests (see Section 3.5.3). In the case of a lacking signal, upper limits on the pulsed flux from the pulsar are calculated (see Section 3.5.4).

3.5.1 Correction of Arrival Times

To each recorded event an absolute time stamp t_{obs} is assigned by the Central Trigger [Funk et al., 2004] (see also Section 3.2.4). The event time stamp is provided by a *GPS167 Meinberg* GPS receiver. The receiver is synchronized to the time signal broadcast by the GPS satellites and to the local rubidium oscillator clock. The precision of the system is less than 100 ns by design [Meinberg Funkuhren GmbH and Co. KG, 2012] and the long term accuracy is estimated to be better than $2\,\mu$s [Funk et al., 2004].

The timestamps t_{obs} are stored in the standard terrestrial time format Coordinated Universal Time (UTC) in units of the SI second. This format is not well suited for astronomical observations as it is bound to the reference system of the Earth, which is not an inertial frame with respect to the pulsar system and non-uniform as it is adjusted regularly to maintain approximate agreement with the Earth's rotation.

In pulsar astronomy, the celestial reference frame of the solar system barycenter (SSB) as defined in the publications of the *International Earth Rotation and Reference Systems Service* [IERS, 2012] is of particular importance and in good approximation an inertial frame with respect to the pulsar. The recorded arrival times t_{obs} are transformed to

the SSB and subsequently to the time of pulse emission in the pulsar frame t_{psr} (pulsar proper time) by incorporating propagation delays of the signal on its way from the pulsar to the observatory. The full correction term reads as

$$t_{\mathrm{psr}}(\,\mathrm{TDB}) = t_{\mathrm{obs}}(\,\mathrm{UTC}) + \Delta_{\mathrm{C}} + \Delta_{\mathrm{SSB}} + \Delta_{\mathrm{B}}. \tag{3.11}$$

The clock related correction term Δ_{C} is used to translate the arrival times from the UTC format to the Barycentric Dynamical Time (TDB) format, the time coordinate of the SSB reference system. The clock correction term first removes the adjustments of the UTC time format due to the irregular rotation of the Earth that are announced as *leap seconds* in the Bulletin C by IERS [2012]. A monotonically increasing time in units of the SI second results which gives the proper time of a clock on the Earth's surface at mean sea level (Terrestrial Time, TT). TDB differs from TT only by a small periodic term that incorporates the metric describing the gravitational potential of the solar system constituents and is done using the analytical expression according to [Fairhead and Bretagnon, 1990].

The actual correction for the propagation delays of the signal on its way from the pulsar to the observatory is done by the correction term Δ_{SSB} that divides into

$$\Delta_{\mathrm{SSB}} = \Delta_{\mathrm{R}} + \Delta_{\mathrm{E}} + \Delta_{\mathrm{S}}. \tag{3.12}$$

The term Δ_{R} (*Roemer delay*) corrects for the motion of the observatory relative to the SSB. The Earth's rotation is calculated using the Earth orientation parameters published in the Bulletin B by IERS [2012]. The position of the SSB with respect to the Earth is defined for each point in time by the masses and positions of the major bodies of the solar system. It is calculated within the *DE200* model by Standish [1982] and is obtained from the Solar System ephemeris published by the *Jet Propulsion Laboratory* [JPL Solar System Dynamics Group, 2012].

In addition, effects of General Relativity imposed on the signal in the Solar System are corrected for by the correction terms Δ_{E} (*Einstein delay*, [Damour and Deruelle, 1986]) and Δ_{S} (*Shapiro delay*, [Shapiro, 1964]). The Shapiro delay is introduced to the signal on its passage through the gravitational field of the Solar System. The Einstein delay describes variations in the clocks referenced to the observatory and to the SSB due to the movement of the Earth in the gravitational field of the Solar System.

The last correction term Δ_{B} is only used for pulsars in a binary system and accounts for local Einstein, Shapiro and Roemer delays introduced by the pulsar's orbital motion in the gravitational field of the constituents of the binary system. The model of Blandford and Teukolsky [1976] is used in this thesis to describe the binary system and to calculate the binary correction term.

The corrected arrival times t_{psr} in the TDB time format then refer to the pulse emission times in a reference frame co-moving with the pulsar (or binary pulsar barycenter) and are searched for periodicity with the phase-folding technique.

3.5.2 Folding of Arrival Times

To search for periodicity within the $i = 1..N$ selected γ-like events from the direction of the pulsar, the corrected arrival times of the events are related to the phase ϕ_i of the pulsar. For this transformation, a timing model is used to describe the pulsar's spin-down behavior. The timing model can be written in the form of a truncated Taylor series expansion (see also Edwards et al. [2006]) of the rotational frequency $\nu = 1/P$ about the model frequency ν_{t_0} as

$$\phi = \sum_{\mathrm{j}} \frac{\nu_{\mathrm{t}_0}^{(j-1)}}{j!}(t_{\mathrm{psr}} - t_0)^j + \phi_0, \tag{3.13}$$

where $\nu_{\mathrm{t}_0}^{(j-1)}$ denote the model frequency and its derivatives, evaluated at a reference time t_0. The reference phase ϕ_0 is used for absolute phase alignment. The parameters of the timing models for the studied pulsars are taken from so-called *pulsar ephemerides*, timing solutions that have been obtained in other wavelengths. The currently largest sample of timing solutions stems from more than 2000 pulsars detected at radio frequencies that are collected in the ATNF pulsar database [Manchester et al., 2005].

Pulsars are known to show irregularities in their spin-down behavior, e.g. sudden changes of the rotational frequency known as *glitches* or rotational instabilities of the neutron star known as *timing noise*. A start and end date of a time period, for which a coherent timing solution could be found, specify the validity range of a pulsar ephemeris. Only those H.E.S.S. data taken within the validity range of a pulsar ephemeris are analyzed for a each pulsar. A distribution of event phases between 0 and 1 results that is referred to as a *pulsar light curve* that in the case of absence of any periodic signal is uniformly distributed in $[0, 1)$.

3.5.3 Tests to Search for Pulsed Emission

Various statistical tests have been put forward to search for periodicity in the obtained distribution of event phases and are used to evaluate as to what extent a measured pulsar light curve agrees with the assumption of a signal present in the pulsar light curve. The sensitivity of these tests is met by the challenges that the distribution of event phases are usually dominated by noise and that the shape of any pulsar light curve is a priori unknown in the VHE γ-ray regime. Known pulsar light curves as measured in other wavebands than the VHE band show a large variation in properties such as the number of pulse peaks, the corresponding pulse widths and positions. The pulsar light curves are known to vary from one pulsar to the next, but are also known to vary for one pulsar when observed in different energy bands. Thus, the statistical tests have to be sensitive to a wide range of possible pulsar light curves when calculating the significance of periodicity in the observed phase distribution of selected events.

Several test statistics are used in the search for pulsed emission to address these questions. The test statistics are constructed such that a single test value is calculated from the phase distribution whose probability density function (PDF) is known either

from theoretical arguments or from simulations. The PDF is then used to reject or accept the hypothesis of a pulsed signal at a desired confidence level. The test statistics described in the following are the *Pearsons* χ^2-, Z^2_m- and H-test. Except for the χ^2-test, the resulting test value can also be used to estimate the strength of the pulsed signal, i.e. fraction p of events in the pulsar light curve that stem from a pulsed signal.

Pearson's χ^2-test

The Pearson's χ^2-test is the simplest test and is most sensitive to single peaked pulsar light curves with rather narrow pulse widths. It is applied to the binned phase distribution and the test value is calculated as

$$\chi^2 = \sum_{\mathrm{i}=1}^{\mathrm{k}} \frac{(n_\mathrm{i} - \hat{n})^2}{\sigma^2_\mathrm{n}}, \tag{3.14}$$

where n_i denotes the number of observed events in the i-th bin, $\hat{n}$ the expected mean number of events per bin and $\sigma_\mathrm{n} = \sqrt{\hat{n}}$ the corresponding standard deviation. With the assumptions of a randomly distributed sample of event phases and an expected number of events per bin > 10, the test statistic follows a χ^2 distribution with $k - 1$ degrees of freedom where k is the number of bins used to construct the test statistic. The probability of the pulse profile to be uniform is given by

$$\mathrm{Prob}(\chi^2, \mathrm{k} - 1) = 1 - \Gamma[0.5(\mathrm{k} - 1), 0.5\,\chi^2], \tag{3.15}$$

where Γ denotes the incomplete gamma function.

A main disadvantage of the Pearson's χ^2-test is the arbitrary number of bins k used to generate the pulsar light curve that can introduce biases or loss of information. Therefore, the bin-free Z^2_m-test [Buccheri et al., 1983] and a generalization of this test, the H-test [de Jager et al., 1989], are used additionally. These tests employ the full knowledge of individual event phases ϕ_i.

Z^2_m-test

For the Z^2_m-test, the 2π-periodicity of the phase profile of N phases ϕ_i is used to expand it in a Fourier series f of the first m harmonics with

$$f_m(\phi_i) = \alpha_0 + \frac{1}{\pi} \sum_{n=1}^{m} [\alpha_n \cos(n\,\phi_i) + \beta_n \sin(n\,\phi_i)], \tag{3.16}$$

where n denotes the harmonic number and the Fourier coefficients are given by

$$\alpha_0 = \frac{1}{2\pi}, \quad \alpha_n = \frac{1}{N} \sum_{i=1}^{N} \cos(n\,\phi_i), \quad \beta_n = \frac{1}{N} \sum_{i=1}^{N} \sin(n\,\phi_i). \tag{3.17}$$

From the Fourier series, the Z_m^2 value is calculated as

$$Z_m^2 = 2\pi N \int_0^{2\pi} \left[f_m(\phi_i) - \frac{1}{2\pi} \right]^2 d\phi = 2N \sum_{n=1}^{m} \left[\alpha_n^2 + \beta_n^2 \right]. \tag{3.18}$$

In the case of a null hypothesis, i.e. no periodicity is present in the pulsar light curve, the test statistic follows a χ^2 distribution with 2 m degrees of freedom. The Z_m^2 test is sensitive to a wide variety of sinusoidal pulse shapes superimposed with a flat background. The simplest sinusoidal pulse shape can be tested using the first two harmonics $m = 1$ and $m = 2$ while higher values m are required for narrow pulse peaks. The Z_1^2 test statistic corresponds to the Rayleigh test [Brazier, 1994]. For $m = 1$, the test variable $x = Z_1^2/2$ follows a PDF

$$f(x|\mu) = \exp\left(-x - \frac{\mu^4}{4} \right) I_0(\mu\sqrt{x})\, dx, \tag{3.19}$$

while for $m = 2$, the test variable $x = Z_2^2$ follows a PDF

$$f(x|\mu) = \exp\left(-x - \frac{\mu^2}{4} \right) \frac{2\sqrt{x}}{\mu} I_1(\mu\sqrt{x})\, dx, \tag{3.20}$$

where $I_k(z)$ denotes the modified Bessel function of the first kind with index k. The unknown parameter μ is given by $\mu = p\sqrt{N}$ and hence is proportional to the true value of the pulsed fraction p, i.e. the fraction of events that can be attributed to any non-uniform contribution to the distribution of event phases. The probability to obtain an x value in the interval $(x; x + dx)$ is $f(x|\mu)dx$.

The number of pulsed excess events can be calculated from the Z_2^2 test statistic in solving for the maximum-likelihood estimate of μ by solving

$$\frac{\sqrt{x}}{\mu} I_0(\mu\sqrt{x}) - \left(\frac{1}{2} + \frac{2}{\mu^2} \right) I_1(\mu\sqrt{x}) = 0 \tag{3.21}$$

as detailed in Schwanke and Fuessling [2007].

The main disadvantage of this test is that one has to find the best value for m so that the test is most sensitive for the expected pulsar light curve. With a value of m that is too small, power is lost against narrow peaked light curves, while with a too large value of m, power is lost against broad and sinusoidal light curves. This disadvantage is overcome by using the H-test.

H-test

In the H-test [de Jager et al., 1989], the optimal number m of harmonics present in the pulsar light curve is searched for in the first 20 harmonics $1 < m \leq 20$ by calculating

$$H = \max_{1 \leq m \leq 20} (Z_m^2 - 4 \times (m-1)), \tag{3.22}$$

using Hart's rule [Hart, 1985] to search for the optimum m (hence the name H-test).

The H-test is thus sensitive to a wide range of possible pulse profiles. The probability of obtaining a test value larger than h was found with Monte Carlo simulations [de Jager and Büsching, 2010] and follows an exponential,

$$\text{Prob}(> h) \approx \exp(-0.4\,h). \tag{3.23}$$

The 2σ and 3σ upper limits on the number of pulsed excess events μ have been found numerically for single-peaked light curves using Monte Carlo simulations [de Jager, 1994] and are

$$\mu_{2\sigma} = (1.3 + 8.7\,\delta)(0.174\,h)^{(0.24+0.13\,\delta)} \exp\left[0.03 + 0.13\,\delta)(\log_{10}(0.174\,h)^2)\right], \tag{3.24}$$

$$\mu_{3\sigma} = (1.5 + 10.7\,\delta)(0.174\,h)^{(0.17+0.14\,\delta)} \exp\left[0.08 + 0.15\,\delta)(\log_{10}(0.174\,h)^2)\right], \tag{3.25}$$

where h denotes the value of the H-test and δ the assumed total phase interval of pulsed emission. These formulas are valid for $h > 0.3$ and $N > 20$ for small pulse widths as well as for $N > 30$ for broad pulse widths ($\delta \sim 0.5$).

3.5.4 Calculation of Upper Limits to the Pulsed Flux

If no significant periodicity is found in the phase distribution of events selected from the signal region, upper limits on the pulsed γ-ray flux can be obtained using several methods. They differ in the assumptions made concerning the characteristics of the pulsed emission, in particular concerning the shape of the pulsar light curve and the pulse positions.

On-Off method

In the *On-Off method*, the pulse position and pulse width as known in other wavebands than the VHE band are used to derive upper limits on the pulsed flux. Thereby, it is assumed that the observed VHE γ-ray flux stems from a similar region within the pulsar magnetosphere as observed in the reference waveband and the resulting pulsar light curves are similar in shape. The pulsar light curve obtained in the reference waveband is then divided in intervals of high emission (*on-phase*) and low emission (*off-phase*).

The events from the off-phase interval subsequently serve as the background estimation used for the calculation according to Eq. 3.2 of the excess of events in the on-phase interval. The normalization factor α is simply the ratio of the on-phase interval to the off-phase interval. The pulsed flux is then calculated from the excess of events using the method of [Aharonian et al., 2006d] under the assumption of a power-law spectrum with a photon index of 2.7. The pulsed flux measurements are converted into 99% confidence level upper limits using the approach of Feldman and Cousins [1998].

Pulsed Fraction method

In the *pulsed fraction* method, the pulsed flux is calculated using the number of pulsed excess events as derived from the Z_2^2- and H-test statistics. Thereby, no knowledge of the pulse position is used, but some assumptions on the pulse width (H-test) and pulse shape (Z_2^2-test) are taken over from the test statistics. Any upper limit on the number of pulsed excess events is calculated for each test statistic and turned into an upper limit on the pulsed flux using the method of [Aharonian et al., 2006d] under the assumption of a power-law spectrum with a photon index of 2.7.

4 Observations of the Millisecond Pulsars J1824−2452 and J0437−4715

4.1 Introduction

Millisecond pulsars (MSPs) and their nebulae are an increasingly abundant class of emitters both for pulsed and unpulsed emission seen in the radio through the high-energy γ-ray band.

About 10% of the total population of more than 2000 radio pulsars are MSPs (see Manchester et al. [2005]). Nearly half of them are located in globular clusters (see e.g. Ransom [2008] for a review and Freire [2011] for a recent catalog). While a significant fraction of the radio-detected MSPs are positionally coincident with a source seen at X-ray energies, only a dozen show pulsed X-ray emission. The majority of the MSPs with pulsed X-ray emission are found in the Galactic Plane (see e.g. Zavlin [2007] for a review) and four are located in a globular cluster [Becker et al., 2010]. Within the sample of MSPs with pulsed X-ray emission, two groups can be identified for which the bulk of the observed pulsed X-ray emission is either of thermal or of non-thermal origin [Zavlin, 2007]. Pulsar wind nebulae have been observed in the X-ray energy band for only two MSPs [Kargaltsev and Pavlov, 2008].

Prior to the launch of the satellite based observatories *Fermi* [Atwood et al., 2009] and *AGILE* [Tavani et al., 2009], pulsed high-energy (HE; $30\,\mathrm{MeV} < E < 100\,\mathrm{GeV}$) γ-ray emission from MSPs was known only for one MSP, PSR J0218+4232, for which pulsed HE γ-ray emission was seen up to $\sim 1\,\mathrm{GeV}$ by *EGRET* [Kuiper et al., 2000]. After the first 18 months of the *Fermi* mission, pulsed HE γ-ray emission was reported for 11 MSPs (see e.g. Ray and Parkinson [2011] for a review) and the number of HE MSPs is expected to grow as searches at radio frequencies, targeted at unassociated *Fermi*-LAT sources for which no pulsed HE emission was reported so far, revealed numerous new MSPs [Ray and Parkinson, 2011]. Pulsed HE γ-ray emission has been found for two MSPs located in a globular cluster. Marginal detection of pulsations from one MSP located in a globular cluster, PSR J1824−2452 in M 28/NGC 6626, was reported by *AGILE* [Pellizzoni et al., 2009] and the so far youngest MSP with a characteristic age of 25×10^6 years was found at GeV energies in the globular cluster NGC 6624 by Freire et al. [2011]. Thus, MSPs with a high spin-down energy flux $\dot{E}/d^2$ are detectable as γ-ray pulsars. Searches for the nebulae of MSPs, however, have so far been unsuccessful [Ackermann et al., 2011].

In the VHE regime, no pulsed or unpulsed emission from MSPs has been observed and upper limits on the VHE γ-ray emission have been reported for PSR J0218+4232 [De los Reyes et al., 2009].

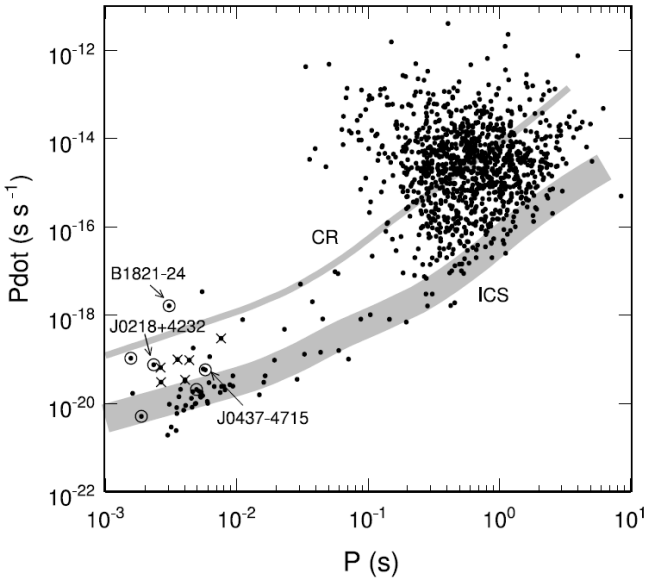

Figure 4.1 $P-\dot{P}$-diagram for known radio pulsars [Manchester et al., 2005, status 2005] with overlaid death lines (gray shaded band) for curvature radiation and radiation from inverse Compton scattering. The width of the death line correspond to the uncertainties within the model due to unknown neutron star surface temperature, mass, radius and moment of inertia.

In this chapter, results of the search for pulsed and unpulsed VHE emission from two MSPs, PSR J0437−4715 and PSR J1824−2452, will be presented.

4.2 Models for pulsed γ-ray Emission from MSPs

As for canonical pulsars, the proposed models for pulsed emission from MSPs are the polar cap (PC) model, the two-pole caustic (TPC) model and the outer gap (OG) model (see Section 2.1.5 for more details). The radiation mechanisms responsible for γ-ray emission at high energies are curvature radiation (CR) in the energy range $0.1-100$ GeV and inverse Compton scattering (IC) in the energy range $0.1-1$ TeV. Synchrotron radiation (SR) is only expected at lower energies of up to 100 MeV. As in the models for canonical pulsars, the pulsar's geometry, i.e. magnetic inclination angle (α), observer viewing angle (ζ) and resulting impact angle ($\beta = \chi - \zeta$), are essential ingredients for the modeling of pulsar light curves and spectra. The models also have to take into account the different pulsar properties of MSPs compared to canonical pulsars such as smaller spin periods, lower surface magnetic field strengths and much more compact magnetospheres. Due to their low spin-down rates, the majority of the MSPs are placed between the so-called CR and IC death lines in the $P-\dot{P}$-diagram as is shown in Fig. 4.1. These death lines define regions within the $P-\dot{P}$-diagram such that pulsars that lie below the CR (IC) death

line cannot produce sufficient $e^{\pm}$-pairs from CR (IC) photons to completely screen the accelerating electric field. It is thus believed that for the MSPs that lie below the CR death line, the accelerating gaps above the neutron star surface or in the outer magnetosphere within the OG models have a larger width compared to those of the canonical pulsars.

In the so-called *pair-starved polar cap* (PSPC) models [Bulik et al., 2000, Harding et al., 2005, Frąckowiak and Rudak, 2005a, Venter and Jager, 2005, Venter, 2008] for MSPs, a variation of the PC models, charges are expected to be accelerated to high altitudes above the polar caps. The resulting electric fields are unscreened and a larger open volume is available for particle acceleration. The maximum attainable particle energies are limited by CR and SR losses rather than by the width of the accelerating region. IC is believed to be negligible for particle cooling. In addition, the magnetic field of MSPs is much lower at high altitudes and γ-ray photons from CR are less affected by attenuation in the pulsar magnetosphere. It is predicted that MSPs can emit high energy γ-rays from CR up to energies of 50 GeV [Frąckowiak and Rudak, 2005a, Harding et al., 2005] or even up to 100 GeV [Bulik et al., 2000] in the most favorable cases. de Jager and Venter [2008] found that the maximum CR photon energies result for small magnetic inclination angles ($\chi < 45°$) and small impact angles β where $\chi \sim \zeta$. While CR is believed to be the dominant emission process for energies below $\sim$ 100 GeV an additional component is expected at higher energies from IC from electrons that scatter off thermal photon fields emitted from heated PCs near the NS surface. This component is only included in the models of Bulik et al. [2000] and Harding et al. [2005] and can extend up to TeV energies. The level of the radiation escaping the pulsar's magnetosphere is, however, much lower than for CR (by 4 orders of magnitude).

The high energy γ-ray emission from MSPs within the OG scenario [Wei et al., 1996, Zhang and Cheng, 2003, Zhang et al., 2007] are similar to those used for canonical pulsars. Pulsed γ-ray emission is then believed to stem dominantly from CR photons from within the outer gap and is, due to the larger curvature radius in the outer magnetosphere, predicted to not extend beyond $\sim$ 1 GeV [Wei et al., 1996] and $\sim$ 30 GeV [Zhang and Cheng, 2003] in the most favorable cases. The contribution from IC from $e^{\pm}$-pairs colliding with soft photon fields to the total pulsed γ-ray flux was modeled by Wei et al. [1996] and is several orders of magnitude lower than the CR flux. This component was omitted in the calculations of Zhang and Cheng [2003] and Zhang et al. [2007]. It was mentioned by Zhang et al. [2007] that those MSPs (e.g. PSR J1824−2452) with a thin gap, i.e. with screened electric fields, that are Crab-like pulsars can emit high-energy γ-rays through the SSC model rather than through the traditional OG model. This model has, however, not been applied to MSPs so far.

Depending on the CR cutoff energy, attenuation of the IC component in the pulsar's magnetosphere and the pulsar's geometry, the γ-ray emission predicted within the PSPC model is in reach for ground-based Cherenkov instruments such as H.E.S.S., while it is

Pulsar name	P	d	Age	$\dot{E}$	$\dot{E}/d^2$	$B_{\rm S}$
PSR	[ms]	[kpc]	[years]	[erg s^{-1}]	[erg s^{-1} kpc^{-2}]	[10^9 G]
J0437−4715	5.76	0.16	6.7×10^9	2.8×10^{33}	1.2×10^{35}	0.28
J1824−2452	3.05	5.5	3.0×10^7	2.2×10^{36}	7.3×10^{34}	2.25

Table 4.1 The characteristics of the candidate millisecond pulsars PSR J0437−4715 and PSR J1824−2452 as collected from the ATNF pulsar catalog [Manchester et al., 2005]. The distances are adopted from Deller et al. [2008] for PSR J0437−4715 and from Harris [1996, (2010 edition)] for PSR J1824−2452. Period, P, distance, d, spin-down age, spin-down luminosity, $\dot{E}$, and the corresponding value for $\dot{E}/d^2$, and magnetic field strength at the neutron star surface, $B_{\rm S}$, are listed. The values for PSR J0437−4715 are corrected for the pulsar's proper motion.

undetectable for H.E.S.S. within the OG models. In the pre-*Fermi* era, the PSPC model was the most widely accepted model for pulsed γ-ray emission from MSPs. The new population of γ-ray MSPs detected with *Fermi*-LAT provides a wealth of information for testing of pulsar models with unprecedented detail and lead to several surprises. The HE pulsar light curves as observed with *Fermi*-LAT (see e.g. Venter et al. [2009]) for the γ-ray MSPs show a large diversity in peak multiplicity, peak width and phase offset between radio and HE peaks. Recent modeling of radio and HE pulsar light curves [Venter et al., 2009] showed that six MSPs, where the double-peaked γ-ray light curve lags the radio light curve by a large phase offset (~ 0.5), are best explained within the TPC/OG models. Only two MSPs where the γ-ray light curve is almost aligned with the radio light curve is best described within the PSPC model. These findings imply that despite the assumption that MSPs are pair-starved, they are able to form narrow accelerating gaps. This indicates that the HE emission processes in MSPs must be similar to those put forward for young γ-ray pulsars. Indeed, it was found that MSPs and young pulsars have magnetic fields at the light cylinder of comparable strength [Abdo et al., 2009]. Unfortunately, model predictions within the newest TPC/OG models for the spectral properties of the pulsed γ-ray emission from MSPs are not yet available.

4.3 H.E.S.S. MSP Candidates

The two MSPs selected to search for pulsed VHE γ-ray emission are PSR J0437−4715 and PSR J1824−2452. Their brightness and/or proximity to Earth make these MSPs good candidates for this task. They have been intensively studied since their discovery both from a theoretical and observational perspective and are archetypes of different classes of MSPs. In this section, both MSP candidates are introduced.

4.3.1 PSR J0437−4715

The binary millisecond pulsar PSR J0437−4715 was discovered with a spin period of 5.76 ms during a southern sky survey for MSPs with the Parkes 64 m radio telescope [Johnston et al., 1993]. The position as obtained from radio observations is (RA, Dec)=($04^{\rm h}37^{\rm m}15.730^{\rm s}$, $-47°15'08.07''$) (J2000.0 coordinates) and PSR J0437−4715 is, with a Galactic latitude of $-42.0°$, located off the Galactic plane. The pulsar properties are summarized in Table 4.1. The distance of $d = 156.3 \pm 1.3$ pc, as measured from the trigonometric parallax [Deller et al., 2008], is one of the most accurate distance measurements for a pulsar to date and makes PSR J0437−4715 the closest MSP and one of the closest neutron stars known [Manchester et al., 2005].

PSR J0437−4715 is in a 5.74-day nearly circular orbit around a white dwarf [Bell et al., 1993]. The properties of the binary system have been measured to high accuracy using 10 years of data collected with Parkes [Verbiest et al., 2008]. The orbit of the binary system is inclined with respect to the Earth's equator at an angle of 138° and is thus not eclipsing. The masses of the neutron star and its companion are $1.76 \pm 0.20\,{\rm M}_\odot$ and $0.254 \pm 0.018\,{\rm M}_\odot$, respectively. The pulsar mass is rather high compared to the canonical neutron star mass of $1.4\,{\rm M}_\odot$, supporting the evolutionary scenario for MSPs with phases of long mass transfer.

PSR J0437−4715 has a proper motion of $\mu = 141\,{\rm mas\,yr^{-1}}$ [Verbiest et al., 2008] that corresponds to a transverse velocity of $v_{\rm t} = \mu \times d = 105\,{\rm km\,s^{-1}}$ at its distance. When calculating the (intrinsic) pulsar properties from the pulsar period and its derivative, the observed period derivative has to be corrected for the contribution of the large pulsar's proper motion, known as the Shklovskii effect [Shklovskii, 1970]. The corrected intrinsic spin period derivative of $\dot{P}_{\rm int} = \dot{P} - \frac{\mu^2 d}{c} \times P = 1.37 \times 10^{-20}\,{\rm Hz\,s^{-1}}$ is four times smaller than the observed period derivative. The inferred characteristic age is 6.7 Gyr, larger by a factor of ~ 2 than the inferred cooling age of the white dwarf companion [Danziger et al., 1993], and makes PSR J0437−4715 a very old member of the MSP population. The surface magnetic field strength is $B_{\rm S} \approx 2.8 \times 10^8\,{\rm G}$ and the magnetic field strength at the light cylinder is $B_{\rm LC} \approx 1.4 \times 10^4\,{\rm G}$. The spin-down luminosity of $\dot{E} = 2.8 \times 10^{33}\,{\rm erg\,s^{-1}}$ is rather low, but with its small distance, PSR J0437−4715 has a high spin-down energy flux at Earth of $\dot{E}/d^2 \approx 1.2 \times 10^{35}\,{\rm erg\,s^{-1}\,kpc^{-2}}$. Its proximity and brightness at Earth render PSR J0437−4715 one of the preferred targets for study of pulsed emission from MSPs.

Pulsed Emission

In addition to the detection of pulsed emission in the radio band, PSR J0437−4715 is also seen in the UV [Edelstein et al., 1995], X-ray [Becker and Trümper, 1993] and high energy band [Abdo et al., 2009]. Pulsar light curves as selected from the literature are shown in Fig. 4.2 and are discussed in more detail in the following.

The radio pulsar light curve (see Fig. 4.2 (a)) consists of a narrow and strong single pulse flanked by weak emission covering more than 50% of the pulse period that becomes stronger at lower radio frequencies. The spectrum follows a single power law with a

spectral index of (-1.17 ± 0.06), a typical value for radio pulsars, and a steepening of the spectrum is observed for radio frequencies greater than 1 GHz [Kramer et al., 1999].

The X-ray pulsar light curve consists of a single broad peak [Zavlin, 2006], nearly coincident with the radio peak. The pulsed emission exhibits an energy dependence where the peak narrows with higher energies (E$\geq$ 2 keV) and shifts by ~ 0.1 in phase. The intrinsic pulsed fraction thereby increases from $\sim 30\%$ in the $0.3 - 0.5$ keV energy band to $\sim 50\%$ in the $2 - 6$ keV energy band. The light curves for various X-ray energy bands ranging from 0.3 keV to 6 keV are shown in Fig. 4.2 (b).

PSR J0437−4715 belongs to the group of X-ray emitting MSPs where the bulk of the X-ray emission stems from thermal radiation (see Zavlin [2007] for a review) with an additional power-law component in the higher X-ray energy band ($\geq$ 2 keV). For old neutron stars such as MSPs, the thermal radiation is attributed to emission from the polar caps that are heated to X-ray temperatures of ~ 1 MK by relativistic particles returning from the acceleration zones within the pulsar magnetosphere [see Zavlin, 2009, for a review]. The thermal component was modeled by Zavlin [2006] with heated polar caps that have a non-uniform temperature distribution of a hotter polar cap core with a radius of 0.35 km and a temperature of 1.4 MK and a colder polar cap rim with a radius of 2.6 km and a temperature of 0.5 MK. The non-thermal power-law component with a photon index of (2.0 ± 0.4) for an absorbing hydrogen column density in the range of $n_{\rm H} = (0.1 - 0.3) \times 10^{20}\,{\rm cm}^2$ contributes mainly at higher X-ray energies ($\geq$ 2 keV). These findings are interpreted by Zavlin [2006] as such that the thermal emission, dominant at lower X-ray energies and coincident in phase with the radio emission, stems from emission zones co-located with those of the radio emission. It is believed that a different emission mechanism is responsible for the non-thermal emission that is dominant at higher X-ray energies and offset by 0.1 in phase from the radio peak. The phase-integrated pulsed X-ray luminosities are $L_{\rm X,th} = (3.4 \pm 0.7) \times 10^{30}\,{\rm erg\,s}^{-1}$ and $L_{\rm X,nonth} = (0.5 \pm 0.2) \times 10^{30}\,{\rm erg\,s}^{-1}$ for the thermal and non-thermal components of the spectrum, respectively. Thus, only $\sim 0.1\,\%$ of the spin-down power are transformed into pulsed X-ray radiation.

While no significant GeV γ-ray radiation was found for PSR J0437−4715 with *EGRET* [Fierro et al., 1995], pulsed γ-ray emission was recently detected above 0.1 GeV by *Fermi*-LAT [Abdo et al., 2009] showing a single peaked γ-ray light curve with the γ-ray peak offset from the radio peak by ~ 0.5 in phase (see Fig. 4.2 (c)). A pulsed energy flux above 0.1 GeV of $F_\gamma = (1.9 \pm 0.3) \times 10^{-11}\,{\rm erg\,cm}^{-2}\,{\rm s}^{-1}$ with a photon index of (2.1 ± 0.3) and an exponential cutoff at (2.1 ± 1.1) GeV was found. The corresponding γ-ray efficiency is $(1.9 \pm 0.3)\,\%$.

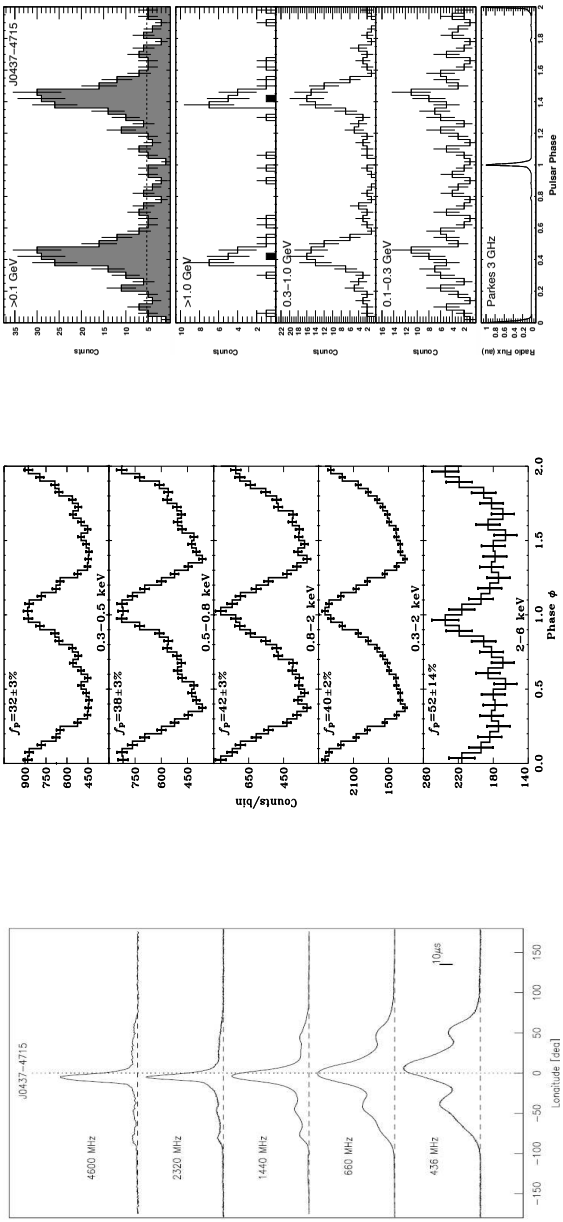

Figure 4.2 Pulsar light curves for PSR J0437−4715 as observed at **(a)** radio energies with Parkes at different frequencies ranging from 436 Mhz to 4.6 GHz (taken from Kramer et al. [1999]), **(b)** X-ray energies with *XMM-Newton* for different energy bands ranging from 0.3 keV to 6 keV (taken from Zavlin [2006]) and **(c)** radio and γ-ray energies as observed with Parkes at 3 GHz (bottom) and *Fermi*-LAT for three energy bands (middle) and the full energy range (top) (taken from Abdo et al. [2009]). Please note that two phase cycles are shown, except for the radio light curves. The estimated fraction of pulsed emission f_p in each energy interval is also indicated for the X-ray light curves. All light curves are aligned in phase so that the phase position of a full period (0.0, 1.0, 2.0) corresponds to the position of the radio peak.

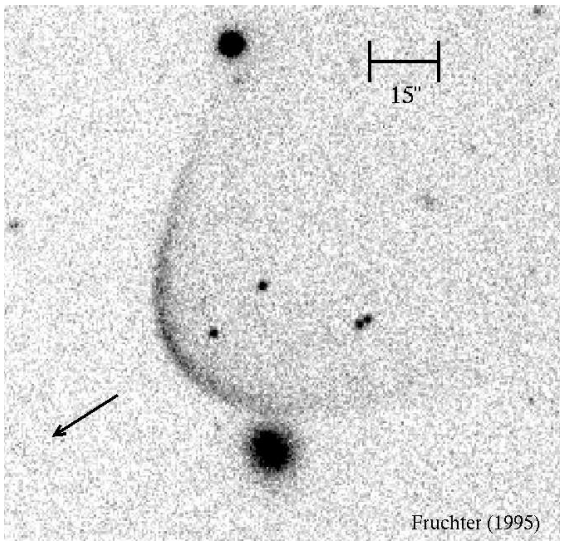

Figure 4.3 Bow-shock nebula around PSR J0437−4715 as observed in the H_α emission (courtesy of A. Fruchter). The arrow indicates the direction of the pulsar's proper motion. The faint star directly behind the shock is the white dwarf companion of the pulsar. The distance between the pulsar and the leading edge of the H_α emission is $10''$. On this scale, the position of the pulsar is indistinguishable from that of its companion.

Steady Emission

Optical observations revealed an H_α bow-shock nebula [Bell et al., 1995] making the pulsar PSR J0437−4715 one of only five pulsars for which such a bow-shock nebula has been observed in H_α [Bucciantini et al., 2005]. An optical image of the H_α bow-shock together with the white dwarf is shown in Fig. 4.3. The bow-shock apex is at about $10''$ south-east of the pulsar, in direction of the pulsar's proper motion. No such nebula is seen at X-ray [e.g. Zavlin et al., 2002] or high energies [Ackermann et al., 2011]. An upper limit on the unpulsed X-ray luminosity of $4.2 \times 10^{28}\,\mathrm{erg\,s^{-1}}$ was placed by Zavlin et al. [2002] in the energy range of $0.1 - 10\,\mathrm{keV}$, calculated at a distance of 139 pc, whereas Ackermann et al. [2011] set an upper limit on the HE luminosity of $0.03 \times 10^{33}\,\mathrm{erg\,s^{-1}}$ in the $0.1 - 100\,\mathrm{GeV}$ energy band using a distance of 156.3 pc.

4.3.2 PSR J1824−2452

The recycled and isolated MSP PSR J1824−2452 with a period of 3.05 ms was the first MSP to be discovered at radio [Lyne et al., 1987] and X-ray frequencies [Saito et al., 1997] in a globular cluster (M 28 or NGC 6626). The globular cluster lies close to the Galactic plane (b= $-5.6°$) and Galactic center (l= $7.8°$) at a distance of 5.5 kpc [Harris, 1996, (edition of 2010)] [1]. PSR J1824−2452 is located 10" offset from the center of the

[1] See also http://physwww.mcmaster.ca/ harris/mwgc.dat for an electronic version of the catalog.

core of M 28 that has a radius of about 0.24' (or 0.4 pc at a distance of 5.5 kpc). With currently 11 detected radio MSPs, M 28 has the third largest population of known MSPs after 47 Tucanae with 23 and Terzan 5 with 33 MSPs [Freire, 2011].

The measured period derivative of PSR J1824−2452 is $\dot{P} = 1.6 \times 10^{-18}\,\mathrm{s\,s^{-1}}$, rather large compared to other MSPs. The pulsar shows no significant proper motion and corrections to the pulsar's period derivative due to acceleration in the cluster's gravitational potential are estimated to be less than 10% and thus negligible, given the large period derivative [Becker et al., 2003]. The properties of PSR J1824−2452 are summarized in Table 4.1. With an age of 30 Myr, PSR J1824−2452 is ~ 100 times younger than most MSPs. It is also the most powerful MSP ($\dot{E} = 2.2 \times 10^{36}\,\mathrm{erg\,s^{-1}}$) and with a spin-down energy flux of $\dot{E}/d^2 \approx 7.3 \times 10^{34}\,\mathrm{erg\,s^{-1}\,kpc^{-2}}$ one of the most energetic pulsars seen at Earth [Manchester et al., 2005]. It has a strong magnetosphere with $B_S = 2.2 \times 10^9\,\mathrm{G}$ and $B_{LC} = 7.2 \times 10^5\,\mathrm{G}$, exceeding the values of PSR J0437−4715 by at least one order of magnitude and reaching the values of the Crab pulsar.

Pulsed Emission

Pulsed emission from PSR J1824−2452 has been subject of various studies in the radio [e.g. Backer and Sallmen, 1997], X-ray [e.g. Mineo et al., 2004, Bogdanov et al., 2011], and HE regime [Pellizzoni et al., 2009]. Pulsar light curves as selected from the literature are shown in Fig. 4.4 and are discussed in more detail in the following.

The pulsed light curve at radio frequencies (see Fig. 4.4 (a)) consists of three components, the prominent peaks RP1 (the main radio peak at 800 MHz) and RP2 (the main radio peak at 1.4 GHz) separated by ~ 0.3 in phase and a broader third peak that follows RP2 with a phase separation of ~ 0.2 [Backer and Sallmen, 1997].

X-ray pulsations from PSR J1824−2452 are observed in a wide energy band of $2 - 20$ keV from a double-peaked structure [Mineo et al., 2004] with two very narrow peaks (see Fig. 4.4 (b)). The peaks are separated by ~ 0.45 in phase with the main X-ray peak XP1 nearly coincident with the radio peak RP1. No energy dependence of the pulsar light curve has been observed.

PSR J1824−2452 belongs to the group of non-thermally emitting X-ray MSPs [Zavlin, 2007] that have high X-ray luminosities of $L_\mathrm{X} > 10^{32}\,\mathrm{erg\,s^{-1}}$ in the energy range $1 - 10$ keV. The phase-averaged non-thermal X-ray spectrum is best described by a single power law with a photon index of ~ 1.2 giving an unabsorbed X-ray luminosity of $1.4 \times 10^{33}\,\mathrm{erg\,s^{-1}}$ in the energy range of $0.3 - 8$ keV [Bogdanov et al., 2011], 2-3 orders of magnitude greater than for typical MSPs and several orders of magnitude greater than for any other MSPs found in M 28. Any thermal component is estimated to be less than 1% of the total X-ray flux in the same energy band.

While *EGRET* reported $3\,\sigma$ upper limits to the pulsed (and unpulsed) γ-ray emission from PSR J1824−2452 above 100 MeV and 1 GeV [Fierro et al., 1995], PSR J1824−2452 has been recently detected in the γ-ray regime for energies above 50 MeV by *AGILE* [Pellizzoni et al., 2009] with a significance of $4.2\,\sigma$ during a 5-day interval in August 2007. The γ-ray pulsar light curve consists of a broad single peak with a width of ~ 0.5 in phase coincident with the radio peak RP2. The γ-ray pulsar light curve is

shown in Fig. 4.4 (c). Surprisingly, only marginal detection was obtained by integrating other periods of comparable duration or the whole data set. While noise fluctuations of the pulsar itself or additional mechanisms disturbing the pulsar magnetosphere in the dense cluster environment are put forward to explain the variable pulsed γ-ray emission, systematic problems of the *AGILE* timing system for some of the observations cannot be excluded [Pellizzoni et al., 2009]. A pulsed integral flux above 100 MeV of $F_\gamma = (18 \pm 5) \times 10^{-8}\,\mathrm{cm}^{-2}\,\mathrm{s}^{-1}$ was found with a γ-ray efficiency of $L_\gamma/\dot{E} = 2\,\%$. No spectral information could be derived from this period. While the integral pulsed γ-ray flux of PSR J1824−2452 given by Pellizzoni et al. [2009] is larger than the total flux measured from the cluster M 28 by *Fermi*-LAT [Abdo et al., 2010a] (see also Section 4.3.2), searches for pulsations from PSR J1824−2452 in the *Fermi*-LAT data have so far not revealed any significant detection.

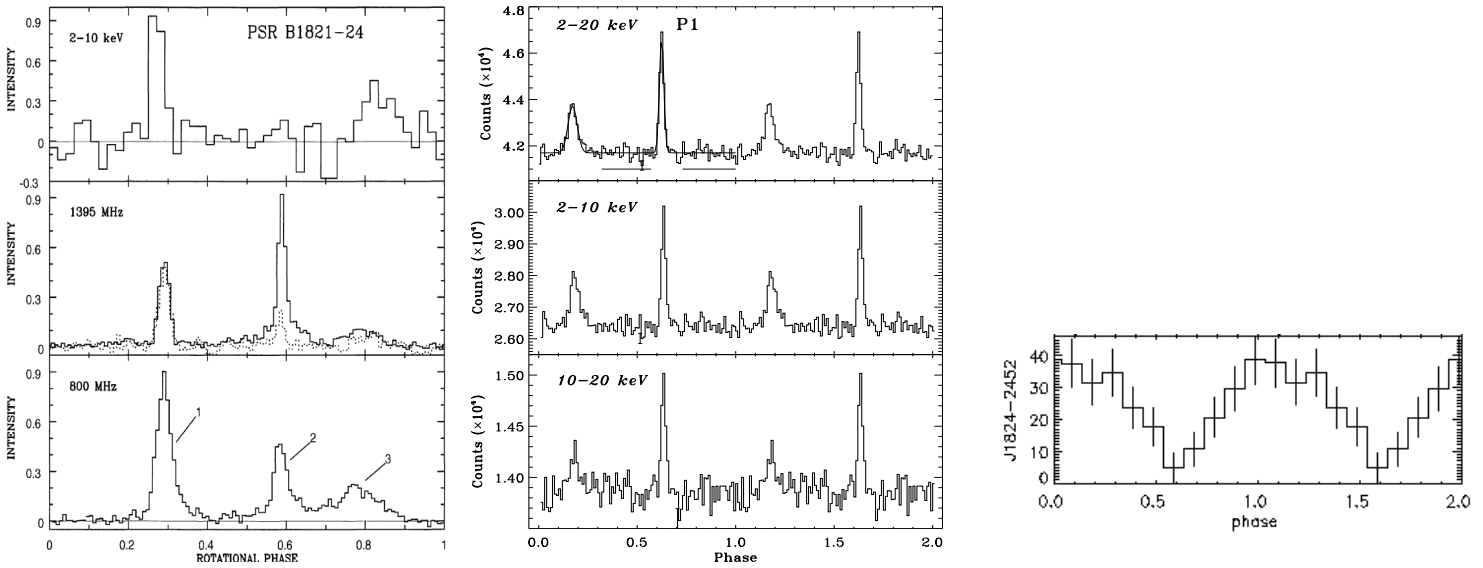

Figure 4.4 Pulsar light curves for PSR J1824−2452 as observed at **(a)** radio energies at two frequencies as observed with Parkes (bottom and middle panel) and X-ray energies (top panel) for the energy range $2 - 10$ keV (taken from Backer and Sallmen [1997]), **(b)** X-ray energies in different energy ranges as observed with *RXTE* (taken from [Mineo et al., 2004]) and **(c)** γ-ray energies as observed with *AGILE* [Pellizzoni et al., 2009]. The light curves in (a) are shown for one phase cycle while two phase cycles are used in (b) and (c). The light curves are phase-aligned such that the main X-ray peak coincides with the main radio peak as measured at 800 MHz, labeled as '1' in (a). The broad single peak observed at HE is nearly coincident with the main radio peak as measured at 1395 MHz, labeled as '2' in (a).

Steady Emission

While the bulk of the X-ray emission can be attributed to pulsed emission from the two narrow pulses (up to 85%), a persistent unpulsed component of $(17.5 \pm 4)\%$ with a similar spectrum as the pulsed component is found from the direction of PSR J1824−2452 and several emission scenarios are put forward to explain the unpulsed X-ray emission [Bogdanov et al., 2011]. An origin from an unresolved PWN as found for other energetic pulsars seems plausible. At a distance of 5.5 kpc, the expected angular size of the X-ray PWN of $\sim 1''$ would be difficult to resolve for *Chandra* given the high source density in the cluster core. Such a PWN would imply an X-ray luminosity of $L_{\mathrm{X}} \sim 10^{32}\,\mathrm{erg\,s^{-1}}$. But also an origin within the pulsar magnetosphere and/or small-angle scattering of the pulsed X-ray emission on dust in the interstellar medium cannot be excluded. In addition, diffuse emission from other X-ray sources that are not resolved within the *Chandra* measurement cannot be excluded.

Steady HE emission from the direction of the globular cluster M 28 was recently detected by *Fermi*-LAT [Abdo et al., 2010a] with a significance of $4.3\,\sigma$ and an integral flux above an energy of 100 MeV of $F_\gamma = (2.6 \pm 1.3) \times 10^{-8}\,\mathrm{cm^{-2}\,s^{-1}}$. The spectrum is well described by a power law with photon index (1.1 ± 0.7) and exhibits a cutoff at (1.0 ± 0.6) GeV. The spectral properties of the emission hence hint to an origin within the magnetosphere of a collection of MSPs, rather than to an origin within a PWN.

4.4 The H.E.S.S. Data Set

Data on PSR J0437−4715 and PSR J1824−2452 were collected in dedicated observation runs in the years 2004 and 2005. Observations were taken in *Wobble* mode with an alternating offset of $\pm\,0.5°$ in Declination and Right Ascension to the nominal source position. PSR J0437−4715 was observed with H.E.S.S. in October 2004 for a total of 11.3 hours in standard observation mode. In October and November 2005, 15.3 hours were added in the convergent observation mode with a topological trigger. Observations of PSR J1824−2452 were made between July and August 2005 for a total of 7.7 hours in convergent observation mode with a topological trigger. After data quality selection and dead-time correction, a total live time of 22.2 hours and 6.3 hours remains for the two data sets of PSR J0437−4715 and PSR J1824−2452, respectively. Table 4.2 summarizes the properties of the different data sets used in the analysis of both pulsars.

The observations were conducted in a restricted zenith-angle range to allow for the lowest possible energy threshold. For PSR J0437−4715, the zenith angles range from 23° to 30° with a mean zenith angle of 25° for each of the two data sets taken in the different observation modes. The zenith angles for PSR J1824−2452 range from 1° to 18° with a mean zenith angle of 7°. The mean target offset is 0.5° for all data sets.

The analysis energy threshold, calculated for *soft selection cuts* at the mean zenith and offset angle of the respective data set, is 230 GeV for the data set taken in the standard observation mode and 210 GeV for the data set taken in the convergent observation mode with a topological trigger for PSR J0437−4715. The lower mean zenith angle for the

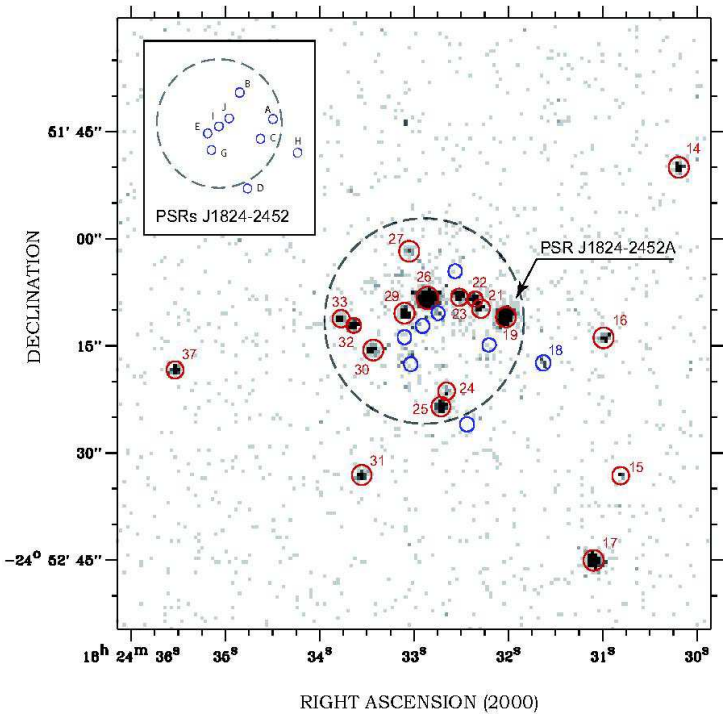

Figure 4.5 *Chandra* X-ray image of the central region of the globular cluster M 28 in counts/s in the energy range $0.2 - 8\,\mathrm{keV}$ (taken from Becker and Hui [2007]). The position of PSR J1824−2452 (source '19' and labeled as PSR J1824−2452A in the image) is marked with an arrow. In total, X-ray emission is observed from 46 sources from the direction of M 28. 12 sources are identified as MSPs (see also Bogdanov et al. [2011]). The location of the strongest MSPs are shown with blue circles in the image and in the inset. The core radius (0.24') of the globular cluster is shown with a dashed circle. Further X-ray sources are indicated by red circles.

Target	PSR J0437−4715		PSR J1824−2452
Observation Mode	SM	TT1	TT1
Date	10/2004	10-11/2005	07-08/2005
Number of runs	12	11	10
Live-time [hours]	12.0	10.2	6.3
Mean System Rate [Hz]	140	110	80
Zenith Angle Range [°]	23-30	23-30	1-18
Mean Zenith Angle [°]	25	25	7
Offset [°]	0.5	0.5	0.5
Energy Threshold [GeV]	230	210	170

Table 4.2 Details of the observations performed in standard mode (SM) and convergent mode with a topological trigger (TT1) on PSR J0437−4715 and PSR J1824−2452. The post-analysis energy threshold, evaluated at the mean zenith and offset angle of the respective data set, is given for *soft selection cuts*.

observations of PSR J1824−2452 results in a lower analysis energy threshold of 170 GeV.

4.5 Results

4.5.1 Steady Emission

The individual data sets on each pulsar in standard and convergent observation mode with a topological trigger have been investigated for a steady point-source like emission at the radio pulsar position using the standard point-source analysis with the reflected-region background model as described in detail in Section 3.3.4. For the analysis presented here, the *soft selection cuts* have been used to allow for a lower energy threshold when compared to an event selection based on *standard selection cuts*.

The resulting event statistics are shown in Table 4.3 for each of the individual data sets taken in the two observation modes for PSR J0437−4715 and for the total data sets for both pulsars. A total of $34 \pm 81_{\mathrm{stat}}$ excess events were found for PSR J0437−4715 from the combined data set, corresponding to a statistical significance of $0.4\,\sigma$. The search for a steady point-source like emission from the direction of PSR J1824−2452 resulted in a total of $-24 \pm 46_{\mathrm{stat}}$ excess events and a statistical significance of $-0.5\,\sigma$.

As no significant γ-ray event excess ($> 5\,\sigma$) is present in any of the data sets, upper limits on the excess events are calculated following the method of Feldman and Cousins [1998] using a confidence level of 99% and subsequently converted to an upper limit on the steady integral γ-ray flux F_γ above the energy threshold E_{th} of the respective data set as outlined in Section 3.3.6. The total exposure which has been used in the calculation of the integral flux upper limit was obtained using the effective collection area computed from Monte Carlo simulations corresponding to the respective observation mode. In the case of PSR J0437−4715 where data sets were taken in two different observation modes, the integral flux upper limit for the total data set has been calculated from the

Pulsar name PSR	Data	N_{on}	N_{off}	α	N_{ex}	S $[\sigma]$	N_{ul}	$F_\gamma(>\mathrm{E_{th}})$ $[\mathrm{cm^{-2}\,s^{-1}}]$
J0437−4715	SM	2440	16480	0.143	86±53	1.6	221	
	TT1	3340	23741	0.143	−52±62	−0.8	112	
	total	5780	40221	0.143	34±81	0.4	243	$< 3.2 \times 10^{-12}$
J1824−2452	TT1	1877	13305	0.143	−24±46	−0.5	97	$< 5.8 \times 10^{-12}$

Table 4.3 Results of the search for point-like γ-ray emission from the direction of the two pulsars for the data sets taken in standard (SM) and convergent observation mode with a topological trigger (TT1). For PSR J0437−4715, the results for the combined data set are also shown. Given are the number of selected γ-ray-like events from the ON region around the pulsar, N_{on}, and from the background regions, N_{off}, that must be scaled with the background normalization factor α to calculate the number of excess events N_{ex} and significance S. Only the statistical errors are shown for N_{ex}. The upper limits at 99% confidence level on the event excess, N_{ul}, and on the integral γ-ray flux F_γ above the energy threshold E_{th} are also shown for the total data sets on PSR J0437−4715 and PSR J1824−2452 with energy thresholds of 230 GeV and 170 GeV, respectively. In the calculation of the integral γ-ray flux upper limit, it was assumed that the source spectrum follows a power law with a photon index of 2.7.

Pulsar name PSR	Energy band [TeV]	L_γ $[\mathrm{erg\,s^{-1}}]$	$L_\gamma/\dot{E}$ [%]
J0437−4715	$1-10$	$< 2.33 \times 10^{30}$	< 0.08
	$1-30$	$< 2.65 \times 10^{30}$	< 0.09
J1824−2452	$1-10$	$< 3.22 \times 10^{33}$	< 0.15
	$1-30$	$< 3.65 \times 10^{33}$	< 0.17

Table 4.4 Upper limits at 99% confidence level on the unpulsed integral γ-ray luminosity L_γ and the spin-down conversion efficiency $L_\gamma/\dot{E}$ in the energy ranges $1-10$ TeV and $1-30$ TeV. A source spectrum following a power law with photon index 2.7 was assumed.

upper limit on the event excess from the total data set and the sum of the two exposures calculated for each of the independent data sets. The energy threshold was set to the maximum of the energy thresholds of the individual data sets. The estimation of the integral flux upper limits is based on the assumption of a γ-ray source spectrum following a power law $dN/dE = N_0(E/E_0)^{-\Gamma}$ with a photon index of $\Gamma = 2.7$ as expected from the background flux. Varying the photon index between 2.0 and 3.0 does not change the integral flux limits by more than 20%. The upper limits on the excess events and integral flux are also shown in Table 4.3.

For comparison with the scaling laws for steady VHE emission from PWNe presented in the next section, upper limits on the integral energy flux G_γ, the γ-ray luminosity $L_\gamma = 4\pi d^2 G_\gamma$ and the spin-down conversion efficiency $L_\gamma/\dot{E}$ in the energy bands $1-10\,\mathrm{TeV}$ and $1-30\,\mathrm{TeV}$ were calculated in a similar fashion as the upper limits on the integral γ-ray flux. The resulting values are shown in Table 4.4. A limiting γ-ray luminosity of $2.65\times10^{30}\,\mathrm{erg\,s^{-1}}$ was found for PSR J0437−4715 in the $1-30\,\mathrm{TeV}$ energy band with a spin-down conversion efficiency smaller than 0.09%. The upper limit on the γ-ray luminosity in the same energy band for PSR J1824−2452 of $3.65\times10^{33}\,d^2_{5.5\,\mathrm{kpc}}\,\mathrm{erg\,s^{-1}}$ [2] is 3 orders of magnitude higher than that for PSR J0437−4715. As the spin-down power of PSR J1824−2452 is also 3 orders of magnitude higher, its spin-down conversion efficiency of less than $0.17\,d^2_{5.5}\,\%$ is in the same order of that of PSR J0437−4715.

4.5.2 Search for Pulsed Emission

The models for pulsed emission of MSPs presented in Section 4.2 predict γ-ray emission from curvature radiation at the lower end of the energy range detectable with H.E.S.S. ($E < 100\,\mathrm{GeV}$) with a possible contribution at higher energies ($E \sim$ TeV) from inverse Compton scattering. To attain a higher sensitivity at various energies, the energy range was split into 8 non-overlapping energy bands. The bins of energy have been defined a-priori and are logarithmically-spaced, ranging from 80 GeV to 100 TeV. The search for pulsed emission has been applied to the selected γ-ray-like events from the direction of the pulsar in each energy interval and in the whole energy range. For the initial search, *soft selection cuts* were used to select γ-ray-like events. The analysis has been repeated for events with an estimated energy below 500 GeV with *low energy selection cuts*. A radius of 0.14° and 0.16° was used for the definition of the circular ON region centered on the radio pulsar position for the soft and low energy cut analysis, respectively. As a cross-check, the same search algorithm has been applied to the selected γ-ray-like events from the background regions constructed in the same field of view as the ON region using the method of the reflected region background model.

The arrival times of the selected γ-ray-like events were subsequently related to the pulsar phase using the timing analysis as described in Section 3.5. For the timing corrections and phase-folding, ephemerides obtained in radio observations [Manchester, 2005] and contemporaneous to the H.E.S.S. data were used. The ephemerides cover the whole H.E.S.S. observation period for both pulsars, giving certainty on a stable

[2] $d_{5.5\,\mathrm{kpc}} = d/(5.5\,\mathrm{kpc})$

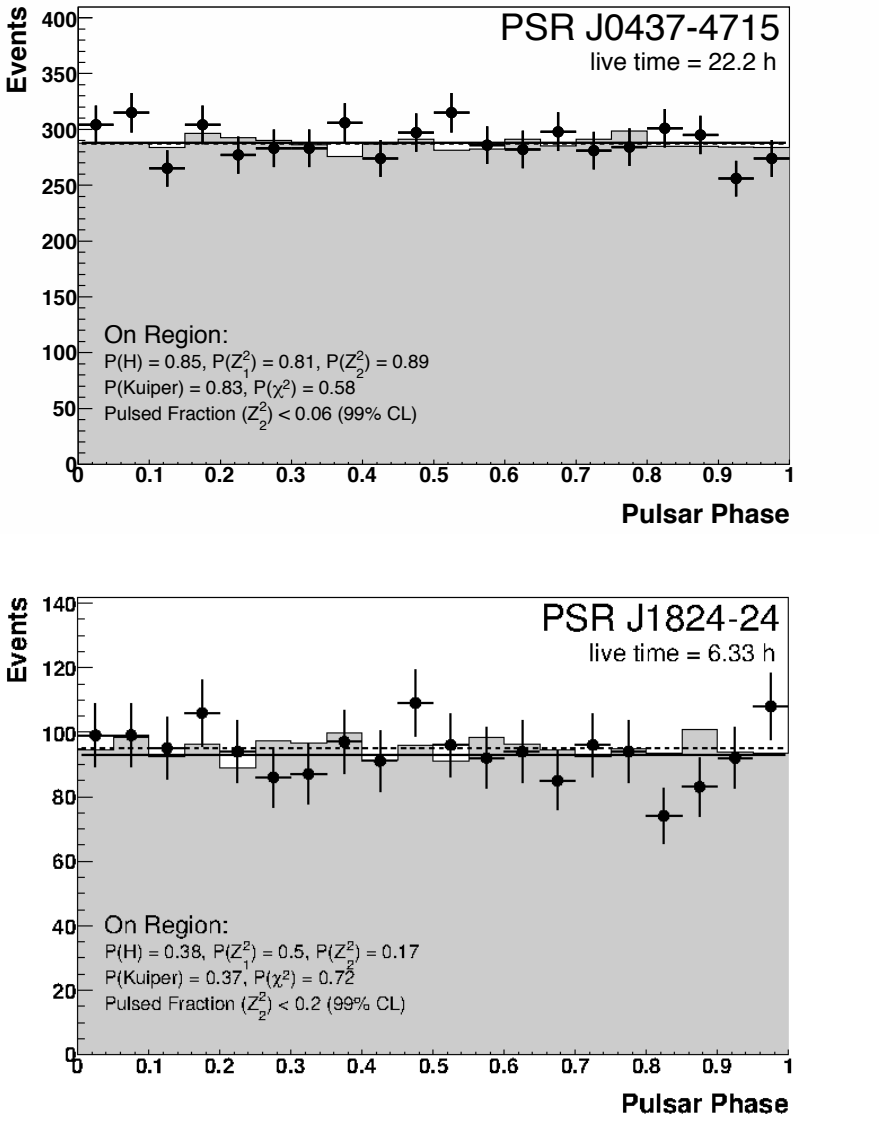

Figure 4.6 Distribution of event phases for PSR J0437−4715 (top) and PSR J1824−2452 (bottom) obtained from the ON region (black points) and from the OFF region (shaded histogram). The solid and dashed line represent a χ^2 fit to a constant to the phase distribution from the signal and the background region, respectively. The probabilities of the statistical tests for the phase distribution from the ON region being consistent with a flat distribution are also shown together with the derived upper limits on the pulsed fraction of events from the ON region.

Pulsar	selection		Probabilities			
PSR	cuts	N_{on}	P_{χ^2}	P_{H}	$P_{\mathrm{Z}_1^2}$	$P_{\mathrm{Z}_2^2}$
J0437−4715	soft	5780	0.58	0.85	0.81	0.89
	lowe	5833	0.32	0.76	0.71	0.60
J1824−2452	soft	1877	0.72	0.38	0.50	0.17
	lowe	2326	0.31	0.20	0.23	0.09

Table 4.5 Results of the search for periodicity in the phase distribution of γ-ray-like events from the signal region around the pulsar for the total data set and all energies. The probabilities of the test statistics being consistent with a flat phase distribution are shown together with the number of selected γ-ray-like events, N_{on}. For each pulsar, the results are shown for the *soft selection cuts* (first line) and for the *low energy selection cuts* based analysis (second line).

timing behavior of the pulsar. Pulsar light curves were constructed from the resulting distribution of event phases using 20 bins in phase, giving good coverage in each phase bin. In Fig. 4.6, the γ-ray pulsar light curves for the full energy range are shown for the ON and OFF region together with a χ^2 fit to a constant for the ON and OFF region, respectively. The pulsar light curve as constructed from the background regions has been normalized with the background normalization factor α, accounting for the different exposure in the signal and background regions. The fit results of a constant to the ON and OFF pulsar light curves of PSR J0437−4715 and PSR J1824−2452 are compatible with the assumption of a flat distribution for all four light curves. The derived constant level of the phase-averaged emission from the ON and OFF region are at the same level, supporting the result of the search for steady emission from the direction of the pulsar. Any steady excess from the ON region would appear as a higher level of emission in the phase-averaged light curve when compared to the OFF region.

The statistical tests to estimate the significance of any pulsed signal as described in Section 3.5.3 were performed on the unbinned and binnned distribution of event phases. For PSR J0437−4715, the statistical tests were applied to the two data sets stemming from the two different observation modes individually and to the combined phase distribution. Table 4.5 shows the probabilities obtained for each individual statistical test applied to the data set of PSR J1824−2452 and the combined data set of PSR J0437−4715, for all energies. No signature of pulsed emission was found for any data set and energy bin. The probabilities for all statistical tests are consistent with the assumption of a flat phase distribution of selected ON and OFF events.

For comparison with predictions for the model spectra, upper limits on the γ-ray excess were calculated and converted to differential upper limits on the pulsed γ-ray flux F_γ in a three-step procedure. In a first step, the pulsed γ-ray excess was obtained in each bin of estimated energy using the *on-off-pulse* method and *pulsed fraction* method on the basis of the Z_2^2-values as described in Section 3.5.4. An ON phase region with a phase interval of 0.2 was used for PSR J0437−4715 [Abdo et al., 2009] and of 0.5 for PSR J1824−2452 [Pellizzoni et al., 2009], centered on the respective γ-ray peak at 0.0

and 0.5. The pulsed excess was calculated for the whole data set of PSR J1824−2452 and the two independent data sets of PSR J0437−4715 for the two observation modes individually. In a second step, the pulsed excess events were converted to a pulsed γ-ray flux under the assumption of a power law source spectrum with a fixed photon index of 2.7. For PSR J0437−4715, a weighted mean flux was calculated from the two independent flux measurements in each individual energy bin. Lastly, a differential upper limit on the γ-ray flux was calculated from the flux measurements with the method of Feldman and Cousins [1998] using a confidence level of 99%. The derived upper limits will be discussed in more detail in the next Section.

4.6 Discussion

In this section, the H.E.S.S. upper limits on pulsed VHE γ-ray emission from the MSPs PSR J0437−4715 and PSR J1824−2452 are compared to scenarios where the emission is of magnetospheric origin. In addition, the results of the search for steady point-like emission from the direction of both MSPs are discussed in the context of an emission scenario of pulsar wind nebula origin.

4.6.1 Steady Emission

Like canonical pulsars, MSPs emit a relativistic wind that can lead to the formation of a pulsar wind nebula (PWN). PWNe powered by canonical young and middle-aged pulsars compose the largest class of Galactic sources seen by H.E.S.S. at VHE energies (see e.g. de Naurois and H.E.S.S. Collaboration [2013]). Little is known, however, about PWNe from MSPs which have a different evolutionary history than canonical pulsars. In the following, the results of the search for steady VHE emission from the two MSPs studied in this thesis will be discussed in the context of PWNe from canonical pulsars found at X-ray, HE and VHE energies.

A systematic search for positional coincidences between VHE γ-ray sources in the H.E.S.S. Galactic Plane Survey and a sample of radio pulsars showed that pulsars with a high spin-down energy flux at Earth of $\dot{E}/d^2 > 10^{35}\,\mathrm{erg\,s^{-1}}$ have a high probability of being detectable as VHE PWNe [Carrigan et al., 2008, Carrigan, 2007]. The positions of 435 radio pulsars, located in the inner part of the Galaxy from -60° to 30° in Galactic longitude and -2° to 2° in Galactic latitude, have been tested for positional coincidence with a VHE γ-ray source. The two MSPs PSR J1824−2452 and PSR J0437−4715 discussed in this thesis were not part of this study as their position is located outside of the search window. The two MSPs have spin-down energy fluxes of $1.2 \times 10^{35}\,\mathrm{erg\,s^{-1}\,kpc^{-2}}$ and $7.3 \times 10^{34}\,\mathrm{erg\,s^{-1}\,kpc^{-2}}$, respectively, that are in the range of that of the detected VHE PWNe and thus suggested, based on the spin-down energy flux alone, that they might be detectable at VHE energies.

Figure 4.7 shows the spin-down power $\dot{E}$ in dependence on the distance d for a sample of canonical pulsars with a detected VHE PWN and for the two MSPs discussed in this thesis. The pulsars with a detected VHE PWN have a spin-down power $\dot{E} >\sim$

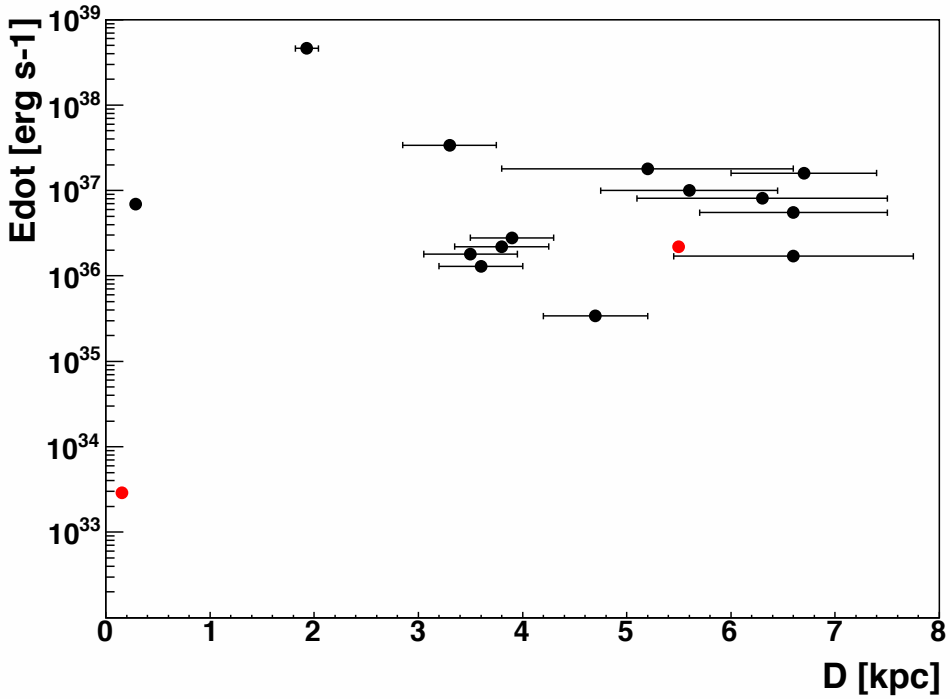

Figure 4.7 Plane of $\dot{E}$ vs. distance d for detected TeV PWNe (filled black circles) as collected from Mattana et al. [2009] and the MSPs PSR J0437−4715 and PSR J1824−2452 (red circles). PWNe from high-$\dot{E}$ pulsars are detected up to a distance d of $\sim 7\,\mathrm{kpc}$. While PSR J1824−2452 has similar $\dot{E}$ and d as the pulsars with a detected TeV PWN, the nearby PSR J0437−4715 has a significantly smaller $\dot{E}$.

$10^{36}\,\mathrm{erg\,s^{-1}}$ and a distance not greater than 7 kpc. PSR J1824−2452 has a relatively high spin-down power, comparable to what is observed from the sample of pulsars with a detected VHE PWN, and is not located at a greater distance than the farthest object in the sample. The spin-down power of PSR J0437−4715, however, is lower by 3-4 orders of magnitude than the average $\dot{E}$ of the pulsars with a detected VHE PWN and it is its proximity that made PSR J0437−4715 a promising candidate for VHE detectability.

The non-detection of steady VHE emission from the direction of the MSPs allowed to put upper limits (at 99% confidence level) on the spin-down conversion efficiency $L_\gamma^{1-10\,\mathrm{TeV}}/\dot{E}$ of $< 0.15\%$ and $< 0.08\%$ for PSR J1824−2452 and PSR J0437−4715, respectively. These upper limits are smaller than the average conversion efficiency of $\sim 1\%$ found for the canonical pulsars with a detected VHE PWNe [Hessels et al., 2008] and the two MSPs are thus inefficient VHE γ-ray emitters. Indeed, no VHE PWN has been detected so far from MSPs which have characteristic ages at least one order of magnitude larger than the canonical pulsars.

The population of HE PWNe currently consists of three clearly identified objects that include the HE PWN inside MSH 15−52 [Abdo et al., 2010b], the Crab Nebula and Vela-X [Ackermann et al., 2011, Pellizzoni et al., 2010]. In a systematic search for steady HE emission from in total 54 pulsars for which pulsed HE emission has been reported in the first 16 months of data taken with *Fermi* [Ackermann et al., 2011], one more highly plausible candidate, PSR J1023−5746, has been found. All of these HE PWNe are powered by young ($1 - 10\,\mathrm{kyr}$) and bright ($\dot{E} > 7 \times 10^{36}\,\mathrm{erg\,s^{-1}}$) pulsars and have also been detected at VHE energies by Cherenkov telescopes. No HE PWN has been clearly identified for any of the 9 MSPs, including PSR J0437−4715, that were part of the pulsar sample tested in the systematic search [Ackermann et al., 2011]. However, the HE γ-ray conversion efficiencies $L_\gamma/\dot{E}$ of the detected HE PWNe from the canonical pulsars are very low (below 1%) and most of the upper limits set for the HE PWN luminosities for the sample of pulsars are not yet constraining. For two MSPs, PSR J2124−3358 and PSR J0034−0534, steady emission was observed up to 10 GeV from a point-like source, but is thought to stem from off-pulse emission from within the magnetosphere rather than from a PWN. The latter scenario, however, cannot be excluded due to limited statistics at energies above 10 GeV. As already stated in Section 4.3, steady HE emission from the direction of PSR J1824−2452 has been observed [Abdo et al., 2010a], but is believed to stem from the globular cluster that harbors PSR J1824−2452 rather than from a PWN powered by the MSP.

Searches for PWNe from pulsars in the X-ray energy domain have revealed numerous firm detections for canonical pulsars, but only for two MSPs, PSR B1957+20 and PSR J2124−3358 (see Kargaltsev and Pavlov [2008] and Zavlin [2007] for a review). In fact, these two MSPs are the only MSPs with a detected X-ray PWN so far. Like PSR J0437−4715, these MSPs belong to the class of pulsars with an H_α bow-shock. The steady X-ray emission is observed from an elongated tail-like structure opposite to the pulsar's proper motion as observed for other bow-shock PWNe [Gaensler, 2005]. The X-ray conversion efficiencies from these tails are similar to those found for canonical pulsars [Zavlin, 2007]. PSR J0437−4715 resembles the MSP PSR J2124−3358 in many aspects. They are both mildly energetic ($\dot{E} \sim 10^{33}\,\mathrm{erg\,s^{-1}}$) and with distances of a few 100 pc relatively close to the Earth. The lack of diffuse X-ray emission from the direction of PSR J0437−4715 is thus surprising. This non-detection is attributed to a very low magnetic field of $< 5\,\mu$G in the post-shock region of PSR J0437−4715 [Zavlin et al., 2002].

As stated in Section 4.3, Bogdanov et al. [2011] confirmed earlier findings of steady X-ray emission from the direction of PSR J1824−2452. However, it is not clear if this steady emission stems from an X-ray PWN or from contamination from other X-ray sources in the globular cluster M 28. In addition, [Cheng et al., 2006] argued that PWNe surrounding MSPs in core regions of globular clusters are likely affected by interactions with the dense stellar environment and are thus possibly underluminous.

Given the lack of detection of a PWN at various energy bands, detailed modeling of

	Energy range	Pulsar name	
		J0437−4715	J1824−2452
L_{X}	$0.2 - 10\,\mathrm{keV}$	$< 4.2 \times 10^{28}\,\mathrm{erg\,s^{-1}}$	$\sim 1 \times 10^{32}\,\mathrm{erg\,s^{-1}}$
L_{γ}	$1 - 30\,\mathrm{TeV}$	$< 2.65 \times 10^{30}\,\mathrm{erg\,s^{-1}}$	$< 3.65 \times 10^{33}\,\mathrm{erg\,s^{-1}}$

Table 4.6 Overview on the unpulsed X-ray and VHE luminosities of PSR J1824−2452 and PSR J0437−4715, respectively.

the PWN scenario for the two MSPs seems unconstraining. The results of the search for steady VHE emission from the two MSPs obtained in this thesis will thus be discussed in context of population studies conducted in the X-ray, HE and VHE energy bands for PWNe from canonical pulsars. It was already noted in Carrigan et al. [2008] that the observed VHE γ-ray luminosity and conversion efficiency are not a simple function of the spin-down energy flux $\dot{E}/d^2$, but that other parameters such as the pulsar age τ_{c}, the nebula volume that is related to the density of the ambient medium and/or the expansion velocity of the shock front (and hence the age of the system), or the magnetic field strength in the nebula region might play a role. Correlation studies connecting the population of VHE PWNe with a complementary population at X-ray and HE energies can be used to provide important diagnostics for a better understanding of the evolution of PWNe. While all of the detected HE PWNe have a VHE counterpart, the sample is currently still too small for correlation studies using HE and VHE PWNe. Using the larger sample of known X-ray and VHE emitting PWNe from canonical pulsars, first studies of the correlation of X-ray and VHE luminosities with pulsar parameters such as the spin-down power $\dot{E}$ and characteristic age τ_{c} have been done by Mattana et al. [2009] and Kargaltsev and Pavlov [2010], as described in more detail in Section 2.2.4. A different scaling behavior of the X-ray and VHE luminosity might be expected for pulsars of such old age as MSPs compared to what is observed for canonical pulsars.

For comparison with the scaling laws from Mattana et al. [2009] on the basis of the pulsar's $\dot{E}$ and τ_{c}, the corresponding values for the X-ray and VHE luminosities of the MSPs discussed in this thesis are converted to the respective $2 - 10\,\mathrm{keV}$ and $1 - 30\,\mathrm{TeV}$ energy ranges used in the correlation studies and are summarized in Table 4.6. For PSR J0437−4715, the upper limit on the $0.1 - 10\,\mathrm{keV}$ PWN X-ray luminosity from the direction of the pulsar [Zavlin et al., 2002] is converted to the $2 - 10\,\mathrm{keV}$ band under the assumption of a power law with a photon index of 2.0. For PSR J1824−2452, the steady X-ray luminosity detected by Bogdanov et al. [2011] is converted to the $2-10\,\mathrm{keV}$ energy band under the assumption of a power law with a photon index of 1.2. As it is not clear whether this emission stems from a PWN, the X-ray luminosity is used as an upper limit in the following. In Table 4.6, the upper limits on the X-ray and VHE luminosity are collected for the two MSPs.

Figure 4.8 shows the X-ray luminosity $L_{\mathrm{X}}^{2-10\,\mathrm{keV}}$, VHE luminosity $L_{\gamma}^{1-30\,\mathrm{TeV}}$ as well

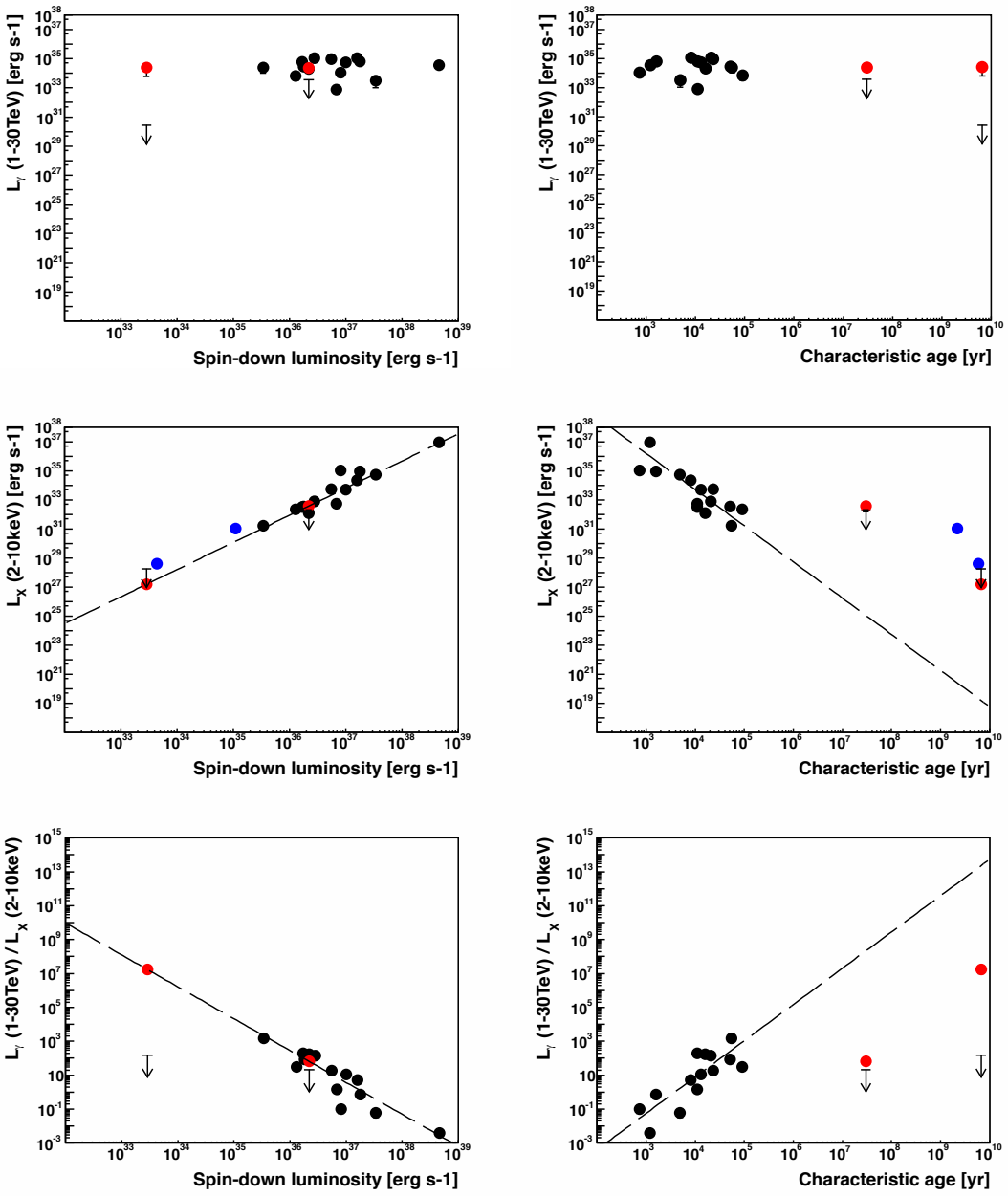

Figure 4.8 Correlations of the TeV (upper row) and X-ray (middle row) luminosity as well as the ratio of TeV-to-X-ray flux (lower row) with $\dot{E}$ (left column) and τ_c (right column) as detailed in Mattana et al. [2009]. The best-fit solution for the scaling laws are presented with dashed lines. The sample of X-ray/TeV PWNe of canonical pulsars used in the study are indicated by filled black circles. For both MSPs, the H.E.S.S. upper limits on the TeV luminosity (upper row), the upper limit on the X-ray luminosity for PSR J0437−4715 and the measured steady X-ray luminosity for PSR J1824−2452 (middle row) and the derived TeV-to-X-ray flux ratio derived from the H.E.S.S. TeV upper limit and the X-ray luminosity as predicted by the scaling law for $\dot{E}$ are indicated by arrows in the corresponding plot. The corresponding values as calculated from the scaling laws for $\dot{E}$ are shown for both MSPs with filled red circles in all plots. In addition, the measured diffuse X-ray emission from the bow-shock MSPs PSR B1957+20 and PSR J2124−3358 are shown with filled blue circles (middle row).

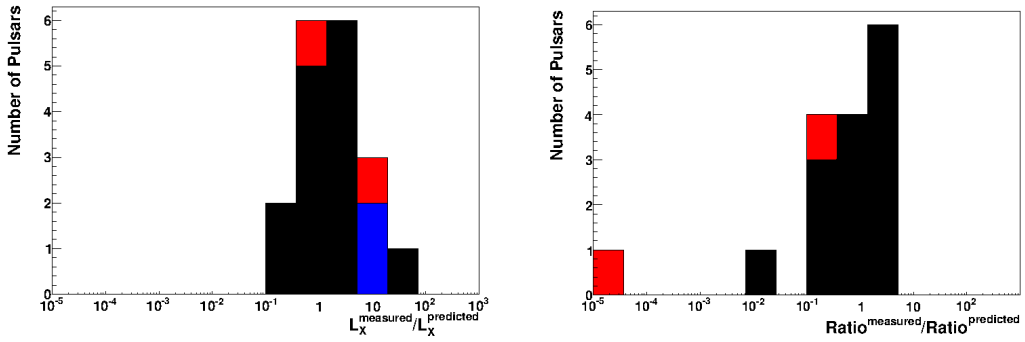

(a) **(b)**

Figure 4.9 Distribution of **(a)** the ratio of measured X-ray luminosity to the predicted X-ray luminosity and **(b)** the ratio of the measured TeV-to-X-ray flux ratio to the predicted ratio. The measured TeV-to-X-ray flux was calculated from the measured H.E.S.S. upper limit on the TeV flux and the predicted X-ray luminosity. All predicted values were calculated from the scaling law for $\dot{E}$ according to the study of Mattana et al. [2009] The filled black histograms represent the X-ray/TeV PWNe used in this study. The filled red histogram represents the MSPs PSR J0437−4715 and PSR J1824−2452, while the blue histogram in (a) indicates the bow-shock MSPs PSR B1957+20 and PSR J2124−3358.

as the corresponding ratio R of VHE-to-X-ray flux $R = F_\gamma^{1-30\,\mathrm{TeV}}/F_\mathrm{X}^{2-10\,\mathrm{keV}}$ [3] for the sample of detected VHE PWNe used in the study of Mattana et al. [2009] (black circles) in dependence of the pulsar's $\dot{E}$ (left column) and τ_c (right column). The scaling laws for L_X and R are indicated by a solid line. In addition, the X-ray luminosities of the bow-shock PWNe of the two MSPs PSR B1957+20 and PSR J2124−3358 are shown as blue circles. The upper limits on the X-ray and VHE luminosities as well as the corresponding ratio R for the MSPs discussed in this thesis are indicated as arrows. For comparison of the predictions from the scaling laws with the measured values for the X-ray and VHE flux, the predicted values for L_X, F_γ/F_X and L_γ on the basis of the scaling law for $\dot{E}$ are indicated for both MSPs and both dependencies on $\dot{E}$ (left column) and τ_c (right column) by red circles in Fig. 4.8.

As a large scatter is inherent in such correlation studies using PWNe of pulsars with different intrinsic and environmental properties, the ratio of the measured values (from now on indicated by the superscript m) to that predicted by the scaling laws (indicated by the superscript p) for both MSPs are compared to the distribution of these ratios as deduced from the sample of PWNe used in the correlation study. Figure 4.9 (a) shows the distribution of the ratio of measured X-ray luminosity L_X^m to that predicted

[3] Please note that $R = F_\gamma^{1-30\,\mathrm{TeV}}/F_\mathrm{X}^{2-10\,\mathrm{keV}} = L_\gamma^{1-30\,\mathrm{TeV}}/L_\mathrm{X}^{2-10\,\mathrm{keV}}$

by the scaling law for $\dot{E}$. The $2 - 10\,\mathrm{keV}$ upper limit on the PWN X-ray luminosity for PSR J0437−4715 is larger by a factor of 5 than estimated from the $L_{\mathrm{X}}^{\mathrm{p}}(\dot{E})$ relation, while the steady X-ray luminosity for PSR J1824−2452 is smaller by a factor of 4. It can be seen, that the measured upper limits do not deviate more from the predicted X-ray luminosity $L_{\mathrm{X}}^{\mathrm{p}}$ than those of the sample of X-ray PWNe used in the study. As noted above, the two bow-shock MSPs PSR B1957+20 and PSR J2124−3358 appear to be overluminous (by a factor of ~ 10) compared to the predicted values. The only other canonical pulsar that has a larger deviation from the distribution of the total sample is PSR J1846−057 (larger by a factor of ~ 40), a very young (706 yr) canonical pulsar, and will be discussed in detail in the next chapter of this thesis.

The measured H.E.S.S. upper limits on the $1 - 30\,\mathrm{TeV}$ VHE luminosity L_{γ}^{m} can be used together with the $2 - 10\,\mathrm{keV}$ X-ray luminosity L_{X} to calculate the ratio R^{m} of VHE-to-X-ray luminosity. As it is not clear whether the measured steady X-ray emission for PSR J1824−2452 stems from a PWN and only upper limits are available for PSR J0437−4715, the X-ray luminosity $L_{\mathrm{X}}^{\mathrm{p}}$ as predicted by the scaling law for $\dot{E}$ is used in the calculation of R^{m}. A ratio of 344 is estimated for PSR J0437−4715 and 36 for PSR J1824−2452. The measured ratio R^{m} can be compared to the predicted ratio R^{p} of VHE-to-X-ray flux as calculated from the scaling law for $\dot{E}$ yielding a so-called double ratio $R^{\mathrm{m}}/R^{\mathrm{p}}$. The distribution of this double ratio is shown in Fig. 4.9 (b) for both MSPs and the canonical pulsars. The ratio R^{m} for the high-$\dot{E}$ MSP PSR J1824−2452 is smaller by a factor of 3 than what is expected from the scaling law, but does not deviate more from the scaling law than is observed for the total sample of pulsars. The derived ratio R^{m} for the comparatively low-$\dot{E}$ pulsar PSR J0437−4715 on the other hand is smaller by a factor of 5×10^4 than the ratio R^{p} estimated from the scaling law. Again, the only other pulsar that has a predicted ratio R^{p} larger than what is observed is PSR J1846−057 (smaller by a factor of $\sim$100). Thus, based on the scaling laws for $\dot{E}$, PSR J1824−2452 and PSR J0437−4715 should have bright VHE PWNe, opposite to what is observed. It is not clear if this discrepancy supports the notion that the MSPs follow a different scaling behavior than what is observed for the sample of canonical pulsars with a detected X-ray and VHE PWN. The discrepancy can be removed, if one assumes that any contribution from an X-ray PWN is smaller than the predicted value used in the calculation of the double ratio. An X-ray luminosity smaller by a factor of 3 and 5×10^4 for PSR J0437−4715 and PSR J1824−2452, respectively, is needed to place the double ratio within the range observed for the sample of canonical pulsars. On the other hand, more stringent upper limits on the VHE luminosity would push the double ratio again to smaller values.

The question whether the two MSPs follow a different scaling behavior than the canonical pulsars or not cannot be unambiguously decided when comparing the upper limits on the X-ray and VHE luminosity to the scaling laws based on the characteristic age of the pulsar (see Fig. 4.8 (right)). As noted by Tauris [2012], the characteristic age of an MSP is not a good indicator for the true age of such a system. At least in the case of an MSP in a low-mass binary system, the cooling age of the white dwarf companion can be

used as an age indicator. PSR J1824−2452 is a relatively young MSP ($\tau_c = 50\,\mathrm{Myr}$), but still 100 times older than the oldest pulsar used in the study by Mattana et al. [2009]. With a characteristic age of 6.7 Gyr and a cooling age of its white dwarf companion of half that value, PSR J0437−4715 is by far the oldest object among the examined pulsars. The upper limits on the X-ray luminosities as measured for PSR J1824−2452 and PSR J0437−4715 (indicated by arrows in Fig. 4.8 (right column)) are 6-8 orders of magnitude larger than what is expected from the scaling law for τ_c. Please note that the X-ray luminosities as expected from the scaling law for $\dot{E}$ (indicated by red circles in Fig. 4.8 (right column)) are also several orders of magnitude larger than what is expected from the scaling law for τ_c for objects of such high age. Additionally, the two MSPs with an identified X-ray PWN are overluminous by several orders of magnitude when compared with the scaling law for τ_c.

The ratio of VHE-to-X-ray flux calculated using the H.E.S.S. upper limit and the upper limits on the X-ray luminosity is smaller than the ratio of VHE-to-X-ray flux as predicted from the τ_c relation by 7 orders of magnitude for PSR J1824−2452 and even by 12 orders of magnitude for PSR J0437−4715. An X-ray luminosity smaller by the same factor would be needed to place the ratio of VHE-to-X-ray flux in the range of that expected from the scaling law for τ_c.

In a similar correlation study, Kargaltsev and Pavlov [2010] found from a larger sample of X-ray- and VHE-emitting PWNe, including objects with less clear identification and a larger fraction of older pulsars, that the correlation of $F_\gamma^{1-30\,\mathrm{TeV}}/F_\mathrm{X}$ with τ_c seems to level off at $\log_{10}\tau_c > 4.5$ or $\tau_c >\sim 32\,\mathrm{kyr}$, respectively. This in turn would put less drastic constraints on the X-ray luminosity when comparing it to the upper limits on the VHE luminosity as measured with H.E.S.S. and the scaling laws.

Due to the non-detection of a PWN in the X-ray and in the VHE energy band, it is not possible to decide whether the scaling laws found by Mattana et al. [2009] hold true for pulsars of a very high age such as PSR J1824−2452 and PSR J0437−4715. However, comparing the age of the MSPs with the total lifetime of VHE-emitting electrons (100 kyr, see Section 2.2.3 and Eq. 2.24), the non-detection at VHE energies supports the view that the PWNe of such old objects as MSPs aged beyond the lifetime of the VHE-emitting electron population. It is thus not surprising that MSPs with ages orders of magnitude larger than canonical pulsars, are not detected as VHE emitters and do not follow the scaling relations for $\dot{E}$ and τ_c found for the sample of canonical pulsars with detected X-ray and VHE PWNe. Further constraints need more detailed studies of the specifics of MSP PWNe. In addition, population studies of higher sensitivity that include older pulsars are needed to add to the diagnostics of PWNe at different evolutionary stages and to model the scaling of X-ray and VHE luminosity with the pulsar parameters and properties of the surrounding medium.

4.6.2 Pulsed Emission

The differential H.E.S.S. upper limits on the pulsed flux derived in the range from $\sim 100\,\mathrm{GeV}$ to $\sim 10\,\mathrm{TeV}$ are compared to model predictions for the pulsed spectrum available for PSR J0437−4715 and PSR J1824−2452. Predictions were made for both MSPs

PSPC	PSR J0437−4715				PSR J1824−2452			
Model	Screened	χ [°]	ζ [°]	$E_{\mathrm{max}}^{\mathrm{CR}}$ [GeV]	Screened	χ [°]	ζ [°]	$E_{\mathrm{max}}^{\mathrm{CR}}$ [GeV]
HUM05	no	10	all	~ 5	yes	50	all	~ 50
FR05	no	35	40	~ 5	no	50	48	~ 50
V08	no	$10 - 35$	$10 - 40$	~ 10	yes	all	all	~ 150

Table 4.7 Overview on the peak CR energy for model predictions within the PSPC models of Harding et al. [2005] (HUM05), Frąckowiak and Rudak [2005b] (FR05) and Venter [2008] (V08) for different geometrical configurations. Adapted from [de Jager and Venter, 2008].

within the 1-dimensional PSPC model by Harding et al. [2005] and within 3-dimensional PSPC models by Frąckowiak and Rudak [2005b] and [Venter, 2008] that include effects from General Relativity. Recent modeling of pulsar light curves observed in the radio and HE band, however, suggests that the pulsed emission for most MSPs (including PSR J0437−4715) is best described within the OG/TPC models while only few MSPs are best described within the PSPC models [Venter et al., 2009]. As PSR J1824−2452 has not been detected by *Fermi*-LAT, no updated model predictions exist for this pulsar and the light curve characteristics (HE peak in coincidence with radio peak) suggest that for PSR J1824−2452, the PSPC model cannot be ruled out. As no predictions for the spectra of pulsed emission are thus far available within the OG/TPC models, the derived upper limits will be discussed for both MSPs in the context of available predictions within PSPC models.

As the model predictions highly depend on the pulsar's geometry, i.e. the magnetic inclination angle χ, the observer angle ζ and resulting impact angle $\beta = \chi - \zeta$, spectra have been calculated for a large range of angles and can be confronted with the derived H.E.S.S. upper limits. Please note that within the model of Harding et al. [2005], total radiation spectra for a specific χ were calculated that do not necessarily represent radiation seen by an observer at a particular viewing angle ζ. In all of the tested PSPC models, the acceleration of particles is limited by CR from primary electrons and SR from primary and secondary electrons. Pulsed emission from IC on thermal X-ray photons has been included only in the model of Harding et al. [2005] while it is neglected in the other PSPC models. Emission from CR is predicted in all models to be the dominant emission process.

Figure 4.10 shows the differential upper limits for PSR J0437−4715 together with the modeled CR spectra and the spectrum as measured by *Fermi*-LAT [Abdo et al., 2009] for the best fit parameters, not taking into account statistical and systematic uncertainties. The energy range for the differential H.E.S.S. upper limits for PSR J0437−4715 lies well above the energy range for CR within the PC models and the expected cutoff energy from the *Fermi*-LAT measurement. All PSPC models assume that the accelerating electric field is unscreened for this MSP. An overview on the energy of the peak CR

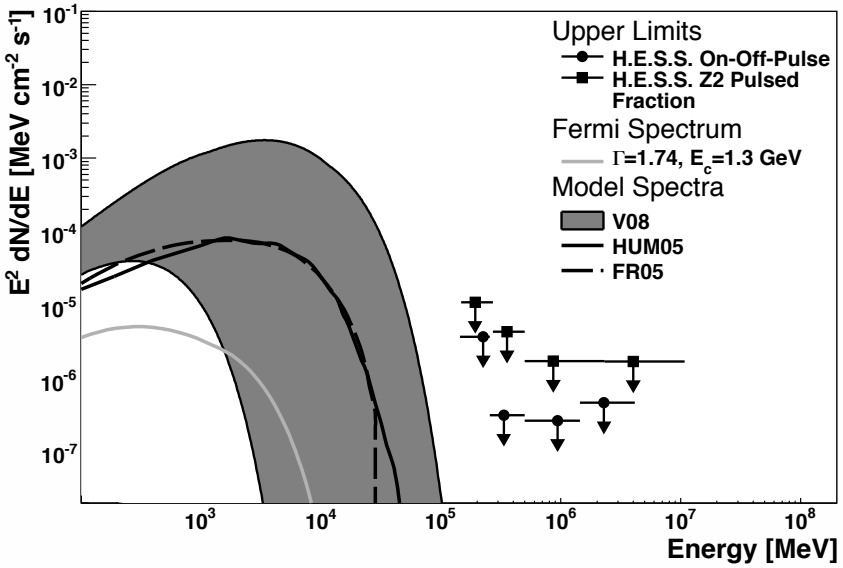

Figure 4.10 H.E.S.S. upper limits as well as predicted curvature radiation spectra from PC models for PSR J0437−4715 together with the *Fermi*-LAT measurement. The solid and dashed line represent predictions by Frąckowiak and Rudak [2005b] (FR05, $\chi = 35°$, $\zeta = 40°$) and by Harding et al. [2005] (HUM05, $\chi \sim 10°$). The gray shaded band indicates the band of possible spectra predicted by Venter [2008] (V08, $\chi = 10° - 35°$, $\zeta = 10° - 40°$). The differential flux upper limits are shown for *soft selection cuts* except for energies less than 500 GeV, where only the upper limits as derived with *low energy selection cuts* are shown.

emission as predicted within the PSPC model for different geometrical configurations can be found in Table 4.7. For most PSPC models, geometrical configurations with an observer angle ζ close to the inclination angle χ were chosen that match the geometrical configuration of ($\chi = 35°$,$\zeta = 40°$) as found from radio polarization measurements [Manchester and Johnston, 1995]. The peak energies range from 0.5 GeV to 10 GeV and are thus well below the H.E.S.S. energy range. The spectrum measured by *Fermi*-LAT shows a lower flux level and has a lower cutoff than the predicted spectra from the PSPC models. This is expected as the CR photons within the OG/TPC models are generated in the much weaker outer magnetosphere ($B_{\rm LC}/B_{\rm S} \sim 10^{-4}$ for PSR J0437−4715). This leads to an overestimation of the accelerating electric field within the PSPC models compared to OG/TPC models. In addition, in the studies of Venter et al. [2009], it was found that the radio and HE light curves of PSR J0437−4715 are best described within the OG/TPC models with an inclination angle $\chi = 30°$ and observer angle $\zeta = 60°$. The larger value of the impact angle β (30° from light curve modeling vs. 5° from radio polarization measurements) also leads to a cutoff of the CR spectra at a lower energy.

Pulsed emission from IC within the PSPC model of Harding et al. [2005] is expected at energies extending from ~ 50 GeV to 10 TeV with a maximum at 1 TeV. The level of

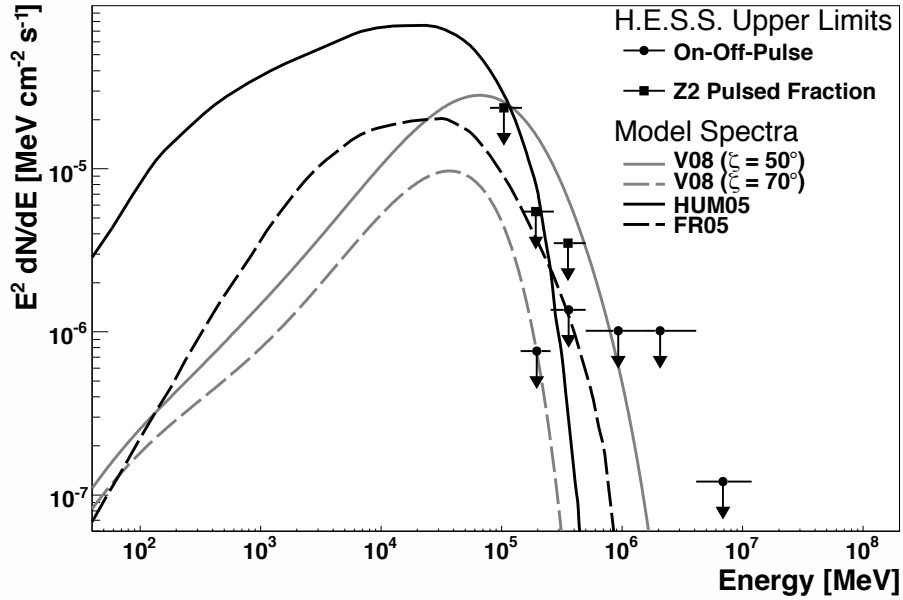

Figure 4.11 H.E.S.S. upper limits on the differential pulsed flux of PSR J1824−2452 and curvature radiation spectra within the PC models by Harding et al. [2005] (HUM05, black solid line), Frąckowiak and Rudak [2005b] (FR05, black dashed line, $\zeta = 48°$) and by Venter [2008] for two different observer angles (V08, gray solid line for $\zeta = 50°$ and gray dashed line for $\zeta = 70°$). All models assume a magnetic inclination angle of $\chi = 50°$. The differential flux upper limits are shown for *soft selection cuts* except for energies less than 500 GeV, where only the upper limits as derived with *low energy selection cuts* are shown.

the predicted emission at 1 TeV is $10^{-8}\,\mathrm{MeV\,cm^{-2}\,s^{-1}}$ for emission from IC which is not attenuated in the pulsar's magnetosphere and $10^{-9}\,\mathrm{MeV\,cm^{-2}\,s^{-1}}$ for emission from IC which is attenuated in the magnetosphere. The level of the IC emission is thus one to two orders of magnitude below the lowest H.E.S.S. upper limit at 1 TeV.

In Figure 4.11, the differential H.E.S.S. upper limits for PSR J1824−2452 are compared to the predictions within the available PSPC models. As PSR J1824−2452 has a much higher magnetic field strength, Harding et al. [2005] and Venter [2008] assume the accelerating electric field to be screened, while Frąckowiak and Rudak [2005b] use an unscreened electric field. The magnetic inclination angle was fixed in most models to $\chi = 50°$ as inferred from radio polarization measurements [Backer and Sallmen, 1997]. The peak CR energies as predicted for different geometrical configurations are summarized in Table 4.7 and range from 0.1 GeV to 150 GeV. The maximum CR cutoff energies for PSR J1824−2452 are much larger than for PSR J0437−4715, due to its larger spin-down energy. Some PSPC models predict high-energy cutoffs to reach up to 100 GeV [Frąckowiak and Rudak, 2005b, Venter, 2008] when the geometry is favorable, i.e. for small impact angles β when the line of sight crosses the narrow beam of radiation and

$\chi \sim \zeta$. The H.E.S.S. upper limits may therefore be used to rule out large observer angles within the model of Venter [2008] as also implied by the value of $\zeta \sim 90°$ as inferred by Backer and Sallmen [1997]. For such a large observer angle where only off-beam radiation will probably be visible, even *Fermi*-LAT may find it difficult to observe CR from PSR J1824−2452 in the context of the current PSPC models.

The pulsed IC emission within the model of Harding et al. [2005] extends from 10 GeV to 10 TeV with a maximum level of radiation at an energy of 5 TeV of $10^{-7}\,\mathrm{MeV\,cm^{-2}\,s^{-1}}$ for the unattenuated spectrum and $10^{-9}\,\mathrm{MeV\,cm^{-2}\,s^{-1}}$ for the attenuated spectrum, respectively. Due to the stronger magnetic field strength of PSR J1824−2452, the attenuation is stronger when compared to that of PSR J0437−4715. The level of the unattenuated component at an energy of 5 TeV is in the order of the H.E.S.S. upper limit, but two orders of magnitude below the H.E.S.S. upper limit for the attenuated component.

In order to resolve the open questions, updated OG/TPC model calculations for the pulsed spectra are needed. The H.E.S.S. upper limits can be used to give valuable input for the level of the inverse Compton component. In addition, upcoming measurements of higher flux sensitivity at GeV to TeV energies from future Cherenkov telescopes such as HESS-II [Vincent, 2005] or CTA [Doro and CTA Consortium, 2011] are needed to address these questions.

5 Observations of PSR J1846−0258 in the composite SNR Kes 75

Among the more than 100 sources detected with Cherenkov telescopes at very high energies (VHE; $E > 100\,\mathrm{GeV}$), a large fraction is associated with pulsar wind nebulae (PWNe) and/or shells of supernova remnants (SNRs) [Horan and Wakely, 2012]. Observations at VHE wavelengths added significantly to the understanding of the properties of these astrophysical sources and of the acceleration mechanisms at work in them (see e.g. Hinton and Hofmann [2009] for a review). A special class among the SNRs that also have been detected at VHE wavelengths are the *composite SNRs* that host a PWN inside an expanding supernova shell. In the case where the angular size of the composite SNR is smaller or close to the point spread function (PSF) of the instrument, the VHE emission remains unresolved and a clear association of any VHE emission from the direction of such object with either the PWN or the SNR shell is difficult. Examples for such cases are the VHE sources HESS J1813−178 and HESS J1640−465 which are each in spatial coincidence with a composite SNR [Aharonian et al., 2006c].

The Galactic supernova remnant Kes 75 is a prototypical example for such a composite SNR. It harbors a PWN in the center of a SNR shell of $3.5'$ diameter. Due to its size, Kes 75 appears point-like for observations with the H.E.S.S. instrument ($\sim 5'$ PSF). Kes 75 stands out from the population of composite SNRs as it is likely a very young SNR associated with a rotation-powered pulsar that has a characteristic age of only 723 years, one of the youngest pulsars known to date. In addition, with its exceptionally high inferred dipole magnetic field of $\sim 5 \times 10^{13}\,\mathrm{G}$ and phases of X-ray outbursts, the pulsar shows properties that place it in the transitional regime to magnetars.

In this chapter, a study of the VHE γ-ray emission as observed with H.E.S.S. from the direction of the Kes 75 region is presented that updates the previous discovery of VHE emission from the direction of Kes 75, labeled as HESS J1846−029 [Terrier et al., 2008]. The analysis presented here uses a data set that more than doubled since the discovery of the VHE source. The study comprises an analysis of the morphology and the spectrum of the VHE γ-ray source and the results are discussed in the context of a possible PWN and/or SNR shell origin for the VHE γ-ray emission. Furthermore, results on the search for periodicity of the VHE γ-ray emission at the pulsar's frequency are presented to determine any magnetospheric contribution to the observed signal from this source.

5.1 The Kes 75 Region

Since the discovery of a radio source in the direction of Kes 75 in 1968, cataloged as G 29.7−0.3 in Kesteven [1968], the region has been studied in considerable detail at various energy bands. Emission is seen at radio [e.g Becker and Helfand, 1984], infrared (IR) [e.g. Morton et al., 2007] and X-ray [e.g. Helfand et al., 2003] wavelengths from a shell-like structure embedding a pulsar and its nebula. The pulsar wind nebula is resolved in the radio [e.g. Becker and Helfand, 1984] and X-ray [e.g. Ng et al., 2008] energy bands. Pulsations from the pulsar PSR J1846−0258 at a period of 324 ms is observed only at X-ray energies [e.g. Gotthelf et al., 2000]. With a spin-down power of $\dot{E} = 8.3 \times 10^{36}\,\mathrm{erg\,s^{-1}}$ and a characteristic age of 723 years, the pulsar is very young and energetic.

5.1.1 The Supernova Remnant Shell

The radio emission from the supernova remnant shell of Kes 75 shows an unusual and highly asymmetric morphology [Becker and Helfand, 1984]. A radio sky map of the Kes 75 region as observed at a frequency of 1.4 GHz with VLA [Bock and Gaensler, 2005] is shown in Fig. 5.1 (a). Only the southern half of the circular shell with a diameter of $3.5'$ is observed while the northern part is undetected. The most intense emission is seen in two regions at the South-Eastern and South-Western end of the half-shell. The radio emission obtained from the two bright regions exhibits a steep spectrum with a spectral index of $\alpha = -0.7$ (for an energy flux $S_\nu = S(\nu_0)\nu^\alpha$) with modest polarization ($< 1\,\%$) and is attributed to synchrotron radiation from the expanding SNR shell [Becker and Helfand, 1984].

The good spatial resolution of *Chandra* has been used to resolve extended X-ray emission from the direction of Kes 75 [Helfand et al., 2003] as shown in Fig. 5.1 (b). An X-ray emitting region of circular size is found with a diameter of $3.2'$, nearly matching the size of the radio emission. While the whole SNR volume is filled with faint and diffuse X-ray emission, bright X-ray emission from the shell is concentrated in two regions in the southern half-shell which are in good spatial coincidence with the radio maxima.

The X-ray spectrum of the faint and diffuse emission observed from the northern part of the SNR shell with *Chandra* can be described by a power law with a photon index of 2.75 [Su et al., 2009]. As pointed out already by Helfand et al. [2003], this X-ray component most likely originates from the PWN rather than the SNR shell and is believed to be dust-scattered into the SNR region, forming a so-called PWN halo.

Some controversy exists on the description of the X-ray spectrum of the two bright southern clump regions. Morton et al. [2007] and Su et al. [2009], using *Chandra* observations of deeper exposure, find the spectrum from the two regions best described by a two-temperature component thermal model that also includes line emission from Si, S, Ar, Mg and Fe. The low-temperature component with $kT \sim 0.2\,\mathrm{keV}$ shows line emission from elements with solar abundances and is associated with thermal emission from circumstellar matter (CSM) and/or interstellar matter (ISM) that has been swept-up and heated by the supernova shock front. The high-temperature component with

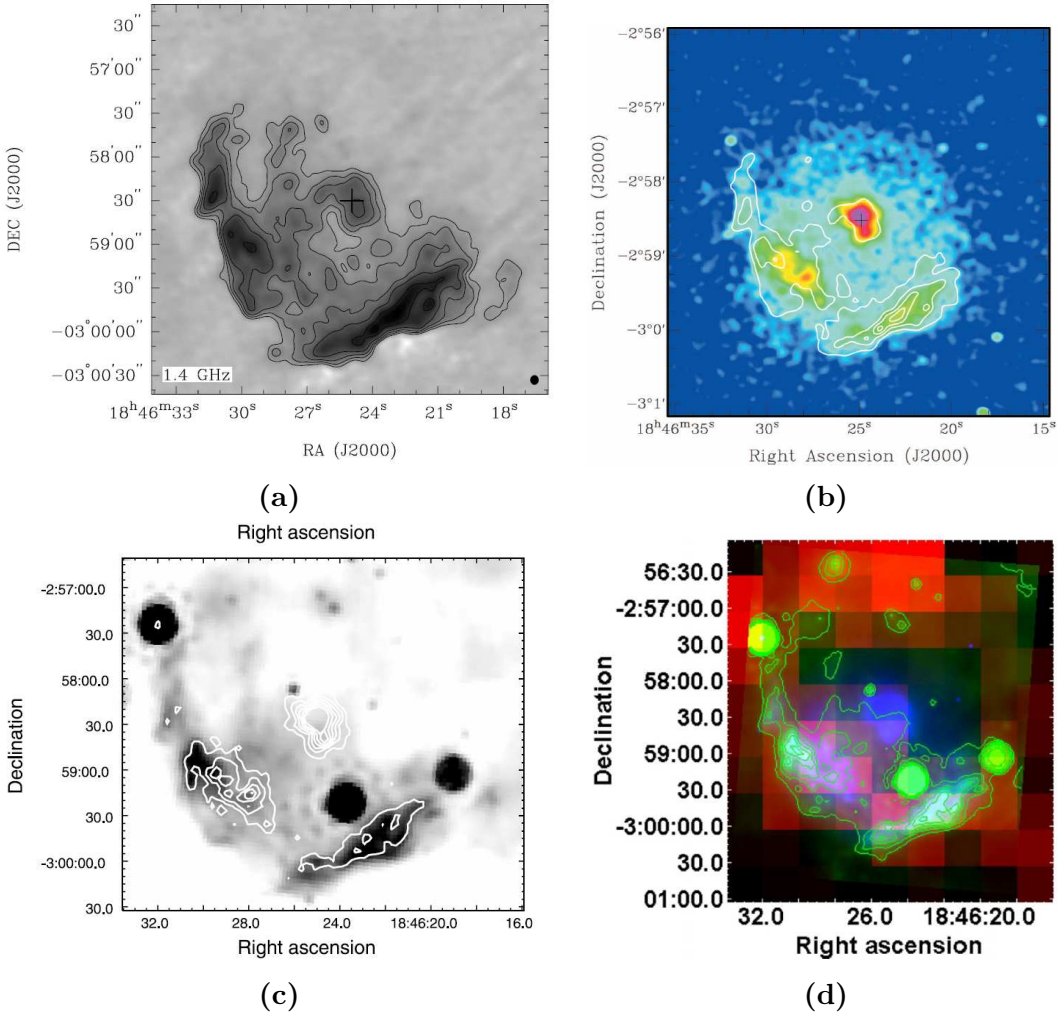

Figure 5.1 **(a):** Sky map of the Kes 75 region as observed with VLA at a radio frequency of 1.4 GHz (logarithmic intensity scale, contours at 2, 5, 10, 20, 50 and 80 mJy/beam). Taken from Bock and Gaensler [2005]. **(b):** Smoothed X-ray map of the Kes 75 region as observed in the 1.0 keV to 7.0 keV energy band with *Chandra* (logarithmic intensity scale). The image has been smoothed with an elliptical Gaussian of $6''.2 \times 5''.4$ size. The radio image contours are overlaid. Taken from Helfand et al. [2003]. The plus sign marks the position of PSR J1846−0258 in (a) and (b). **(c):** Spitzer 24 μm mid-IR image of the Kes 75 region (logarithmic scale, ranging from 100 to 200 MJy sr^{-1}). The *Chandra* X-ray contours are overlaid. The bright and faint circular sources in the image are consistent with point sources along the line of sight to Kes 75. Taken from Morton et al. [2007]. **(d):** ^{12}CO intensity map in the velocity interval of 45 to 51 km s^{-1} (red scale). The Spitzer 24 μm IR contours (green) and the smoothed *Chandra* X-ray emission in the energy from 1.0 keV to 7.0 keV (blue) are overlaid. Taken from Su et al. [2009].

$kT \sim 1.5\,\mathrm{keV}$, however, shows line emission from elements with abundances larger than the solar values. It is therefore believed that this component is thermal emission from hot and metal-rich SN ejecta that have been shock-heated by a supernova reverse shock. It is estimated from the best-fit model that the supernova reverse shock would have been formed within the last 75 years [Morton et al., 2007].

An alternative description of the X-ray spectrum from the southern clump regions is given by Temim et al. [2012]. Whereas Morton et al. [2007] and Su et al. [2009] used a background region that is located outside of the SNR region to derive the X-ray spectrum from the two southern clumps, a region located in the northern part of the SNR shell is used by Temim et al. [2012] in a reanalysis of the *Chandra* data to estimate the background and to subtract any contribution from the dust-scattered PWN halo. It is found that the X-ray spectrum can be equally well described by a single-temperature thermal model with $kT \sim 1.5\,\mathrm{keV}$ and a two-temperature thermal model with $kT \sim 0.2\,\mathrm{keV}$ and $kT \sim 1.5\,\mathrm{keV}$. Both model fits include line emission from Si, S, Ar, Mg and Fe, but in contrast to previous studies no evidence is found for elemental abundances larger than the corresponding solar values in either of the model fits. A supernova reverse shock is thus not needed to explain the observed X-ray emission. A circumstellar or interstellar origin is favored where the hot X-ray emission component may be produced by the interaction of the SN shock front with clumpy CSM.

The detection of $24\,\mu\mathrm{m}$ mid-IR emission from the direction of Kes 75 using the *Spitzer Space Telescope* [Morton et al., 2007, Temim et al., 2012] allows to trace the location of dust which has been swept-up by the SN shock front and collisionally heated by the shocked, X-ray emitting gas. The mid-IR emission is only observed in the southern regions, as shown in Fig. 5.1 (c), and is in good spatial agreement with the bright southern regions seen in the radio and X-ray energy bands. The IR spectrum is dominated by continuum emission from two distinct dust components of temperatures 55 K and 140 K [Temim et al., 2012]. These findings support the view of a low- and a high-temperature X-ray emitting gas being present that heat the cool and hot dust components, respectively. While the hot dust component is concentrated in the southern clump regions, the cool dust component extends over a larger region to the inner SNR region and along the southern shell.

Observations of $^{12}\mathrm{CO}(J = 1 - 0)$ and $^{13}\mathrm{CO}(J = 1 - 0)$ line emission revealed several molecular clouds (MCs) in the direction of Kes 75, one MC complex in the velocity range $45 - 58\,\mathrm{km\,s^{-1}}$ and several MCs in the velocity range $83 - 96\,\mathrm{km\,s^{-1}}$ [Su et al., 2009]. The $^{12}\mathrm{CO}$ intensity map for a velocity range of $45 - 51\,\mathrm{km\,s^{-1}}$ is shown in Fig. 5.1 (d). The emission is concentrated in a ring-like structure and the southern rim is in spatial coincidence with the emission maxima of the bright southern regions of Kes 75 as seen at radio, X-ray and mid-IR wavelengths. This correlation suggests that Kes 75 is associated with the adjacent MC complex. The mean velocity of this complex is $54\,\mathrm{km\,s^{-1}}$ and corresponds to a kinematic distance of $10.6^{+0.1}_{-1.0}\,\mathrm{kpc}$. Furthermore, molecular clouds present in the line of sight to the northern region of Kes 75 (in the velocity ranges $51 - 58\,\mathrm{km\,s^{-1}}$ and $83 - 96\,\mathrm{km\,s^{-1}}$ which correspond to kinematic distances smaller than 10.6 kpc) are believed to obscure the X-ray emission from the northern region and thus

can be used to explain the unusual asymmetric X-ray morphology of the SNR shell [Su et al., 2009]. However, a possible interaction with clumpy circumstellar matter or a non-uniform ambient medium cannot be excluded, as pointed out by Su et al. [2009].

Several SNR properties such as its age and expansion are still uncertain which can be largely attributed to the unknown distance to Kes 75. Early estimates of the distance based on HI absorption measurements are in the range of $6.6 - 19\,\mathrm{kpc}$ [Caswell et al., 1975] and $19 - 21\,\mathrm{kpc}$ [Becker and Helfand, 1984]. Using measurements of HI absorption of higher sensitivity and ^{13}CO emission, Leahy and Tian [2008] give a range for the distance of $5.1 - 7.5\,\mathrm{kpc}$. An association of Kes 75 with the molecular clouds at a velocity of $54\,\mathrm{km\,s^{-1}}$, as discussed above, would place Kes 75 at a distance of about 10.6 kpc Su et al. [2009]. Due to the large extinction in the direction of Kes 75, neither the historical event of the SN nor its remnant have been observed at optical wavelengths. Thus, no independent estimate of the SN age or distance exists. In the following, the distance of $d_{6\,\mathrm{kpc}} = 6\,\mathrm{kpc}$ will be adopted.

At the assumed distance, the SNR shell as seen at radio energies with a diameter of $3.5'$ has a projected size with a radius of $r = 3.05\,d_{6\,\mathrm{kpc}}\,\mathrm{pc}$, consistent with an age of ~ 800 years and an expansion velocity of $3800\,d_{6\,\mathrm{kpc}}\,\mathrm{km\,s^{-1}}$ which is similar to the value of $3700\,\mathrm{km\,s^{-1}}$ found from broadening of the X-ray emission line of Si [Helfand et al., 2003]. This would place Kes 75 in the free expansion phase in a standard Sedov-Taylor evolution model. These findings can be interpreted in a scenario as discussed by Chevalier [2005] for a core-collapse SN where the supernova shock wave runs into a dense environment pre-existing the supernova explosion. The stellar winds of a massive SN progenitor such as a Wolf-Rayet star could have swept up the circumstellar medium, thus creating a low-density bubble which is bounded by dense wind shell. The SN shock front then travels almost freely through a region of very low density until it interacts with the dense wind shell.

5.1.2 The Pulsar Wind Nebula

Emission from the pulsar wind nebula in the center of Kes 75 has been resolved in the radio [e.g Becker and Helfand, 1984] and X-ray [e.g. Ng et al., 2008] energy bands and is detected up to 200 keV with *INTEGRAL* [McBride et al., 2008].

The radio emission is strongly polarized (up to 25%) and exhibits a flat spectrum with a spectral index of $\alpha = 0.3$ [Becker and Helfand, 1984].

The X-ray morphology of the PWN has been mapped in great detail using deep *Chandra* observations [Ng et al., 2008] and is shown in Fig. 5.2 (a). Diffuse X-ray emission is seen from a complex structure with elongated emission along a symmetry axis which is oriented in the North-West to South-East direction. The PWN has a radius of $\sim 20'' = 0.6\,d_{6\,\mathrm{kpc}}\,\mathrm{pc}$. At the center of the PWN, a bright point source at the position of the pulsar PSR J1846−0258 is observed which is embedded in a compact diffuse nebula of $3''$ width. Small-scale structures such as equatorial outflows and polar outflows to the south of the pulsar can be seen. The best-fit model to the PWN structure of a torus, jet-like features along the symmetry axis and a point source with its compact nebula in the center of the PWN are shown in Fig. 5.2 (b).

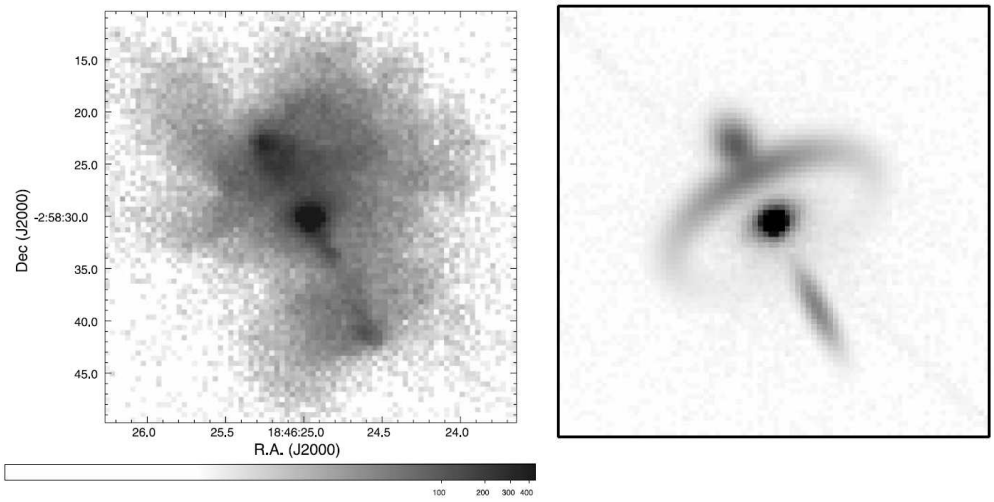

(a) **(b)**

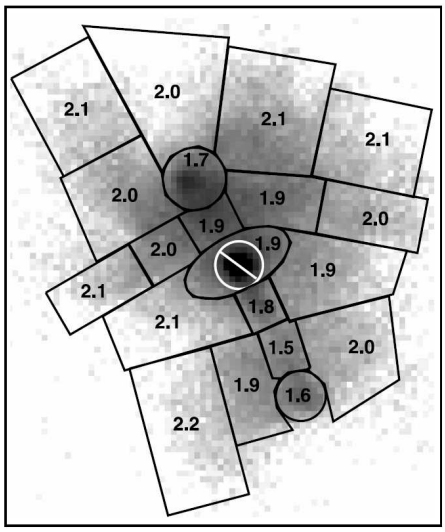

(c)

Figure 5.2 **(a):** Sky map of the PWN region as observed in 2006 with *Chandra* in the $1-8\,\mathrm{keV}$ energy range. Diffuse emission is seen from a structure with an overall diameter of $40''$. The structure is elongated along the symmetry axis directed from North-West to South-East. A bright point source at the position of the pulsar PSR J1846−0258 is embedded in a compact nebula at the center of the PWN. **(b):** Best-fit model to the PWN structure of a torus, a point source and three Gaussian ellipses that represent the compact diffuse nebula surrounding the point source as well as the clumps and jets observed north and south of the pulsar. **(c):** Extraction regions for the PWN spectrum and corresponding best-fit power-law photon indices. All images taken from Ng et al. [2008].

The X-ray spectrum as derived in the energy range of $0.5 - 10\,\mathrm{keV}$ from the total PWN region is well-described by an absorbed power-law ($F \propto \nu^{-\Gamma}$) with an absorbing column density of $N_\mathrm{H} \sim 4 \times 10^{22}\,\mathrm{cm}^{-2}$ and a photon index of $\Gamma \sim 1.9$. The photon index varies across the PWN region with harder photon indices of ~ 1.6 in the inner regions and softer photon indices of ~ 2.1 in more distant regions [Ng et al., 2008]. The photon index for various extraction regions is shown in Fig. 5.2 (c). The total PWN X-ray luminosity is $L_X^\mathrm{PWN} = 1.4 \times 10^{35}\,d^2_{6\,\mathrm{kpc}}\,\mathrm{erg\,s}^{-1}$ in the $0.5 - 10\,\mathrm{keV}$ energy band and the corresponding conversion efficiency is $\eta_X^\mathrm{PWN} = L_X^\mathrm{PWN}/\dot{E} \sim 2\,d^2_{6\,\mathrm{kpc}}\%$. These X-ray properties of the PWN of PSR J1846−0258 are similar to the values observed for other young X-ray PWNe [e.g. Kargaltsev and Pavlov, 2008].

While the PWN spectrum extends from X-ray energies up to 200 keV, as observed with *INTEGRAL* [McBride et al., 2008] (though contribution from the pulsar cannot be excluded), without a spectral break, such a break might exist between the radio and X-ray energy band. Morton et al. [2007] estimate a spectral break at a frequency of $5 \times 10^{14}\,\mathrm{Hz}$ that corresponds to an energy in or near the IR band. If this break is attributed to synchrotron cooling, a magnetic field of 100 mG is estimated. This value is unusually large and it has been argued that the break is rather due to evolutionary effects such as an intrinsic break in the injection spectrum of particles [Ng et al., 2008] or a nonuniform magnetic field than due to standard synchrotron cooling.

5.1.3 The Pulsar PSR J1846−0258

The **isolated rotation-powered pulsar** PSR J1846−0258 in the core of Kes 75 was discovered at X-ray energies with *RXTE* and *ASCA* [Gotthelf et al., 2000] and *INTEGRAL* [Kuiper and Hermsen, 2009] up to an energy of 150 keV. The position of the pulsar is (RA, Dec)=($\alpha = 18^\mathrm{h}46^\mathrm{m}24.94^\mathrm{s} \pm 0.01^\mathrm{s}, \delta = -2°58'30.1'' \pm 0.2''$) (J2000.0 coordinates). Despite extensive searches in the radio [Archibald et al., 2008] and HE [Parent et al., 2011] band, it has been so far not detected at any other waveband. Given the non-detection at radio energies, a distance estimate from the radio dispersion measure is not available and an association of the pulsar and its nebula with Kes 75 are based on spatial coincidence and energetics.

The pulsar has a spin period of 324 ms and a spin period derivative of $7.1 \times 10^{-12}\,\mathrm{s\,s}^{-1}$ and is, with a spin-down power of $\dot{E} = 8.3 \times 10^{36}\,\mathrm{erg\,s}^{-1}$, quite energetic. With a characteristic age of only 723 years [Gotthelf et al., 2000], it is among the youngest known rotation-powered pulsars in the Galaxy. PSR J1846−0258 showed a very stable timing behavior for more than five years after its discovery in 2000 and Livingstone et al. [2006] were able to measure a braking index of $n = (2.65 \pm 0.01)$. Under the assumption of a constant braking index since pulsar birth ($\dot{\nu} \propto \nu^n$), an upper limit on the true age of 884 years consistent with the characteristic age can be inferred.

Pulsed X-ray emission is seen from a broad single peak with an energy-independent shape [Kuiper and Hermsen, 2009] (see Fig. 5.3). The spectrum of the pulsed emission can be well described by a power law with a photon index of ∼1.2 [Gotthelf et al., 2000]. The pulsar has an X-ray luminosity of $L_\mathrm{X}^\mathrm{PSR} = 2.6 \times 10^{34}\,d^2_{6\,\mathrm{kpc}}\,\mathrm{erg\,s}^{-1}$ in the

$0.5 - 10\,\mathrm{keV}$ energy band and a corresponding X-ray conversion efficiency of $\eta_{\mathrm{X}}^{\mathrm{PSR}} \sim 0.3\,d_{6\,\mathrm{kpc}}^2\%$ [Ng et al., 2008], comparable to other young rotation-powered pulsars. While PSR J1846−0258 does not appear to be different from the population of rotation-powered pulsars with respect to its X-ray conversion efficiency, the pulsar stands out from this population as it has a very high dipole surface magnetic field strength of $\sim 5 \times 10^{13}\,\mathrm{G}$ as inferred from the standard magnetic braking model with a braking index of $n = 3$ [Gotthelf et al., 2000]. The magnetic field strength is among the largest dipole field strengths known from young pulsars and places PSR J1846−0258 in a transitional regime to magnetars.

Phase coherence, i.e. a valid timing solution describing the spin-down behavior of PSR J1846−0258, was lost on 31 May 2006 when four short ($< 0.1\,\mathrm{s}$) X-ray outbursts, followed by a fifth outburst on 27 July 2006, were observed with *RXTE* [Gavriil et al., 2008] and *Chandra* [Kumar and Safi-Harb, 2008]. Figure 5.4 (bottom panel) shows the pulsed flux for ~ 8 years of *RXTE* observations [Livingstone et al., 2010]. The $2-10\,\mathrm{keV}$ pulsed X-ray flux increased during the outbursts on 31 May 2006 by a factor of ~ 5, a magnitude similar to what is observed from magnetars. The increase was followed by a decline of the pulsed flux enhancement that lasted for $\sim 2\,\mathrm{months}$ with a total $2-60\,\mathrm{keV}$ energy release of $(3.8 - 4.8) \times 10^{41}\,d_{6\,\mathrm{kpc}}^2\,\mathrm{erg}$ [Gavriil et al., 2008], assuming isotropic emission. In a spectral analysis of *RXTE* data [Kuiper and Hermsen, 2009], it was found that the outburst dominantly added a soft component below $10\,\mathrm{keV}$ to the spectrum, while the higher energy part of the spectrum remained unchanged. Consequently, the photon index of a power-law fit to the pulsed X-ray spectrum changed from ∼1.2 in 2000 (pre-outburst) to ∼1.9 during the outburst in 2006.

The X-ray outburst was accompanied by a sudden glitch of the pulsar's period with an initial frequency increase of $\delta\nu = 1.24(41) \times 10^{-5}\,\mathrm{Hz}$, followed by a long period of exponential recovery with a net decrease of the pulse frequency of $(-9.52 \pm 0.09) \times 10^{-5}\,\mathrm{Hz}$ [Livingstone et al., 2010]. Figure 5.4 shows the frequency relative to the initial frequency as predicted by the pre-outburst timing model (top panel) and the frequency derivative (middle panel) for six years of *RXTE* observations [Livingstone et al., 2010]. The glitch with a sudden change in frequency and frequency derivative are clearly visible. While phase coherence was completely lost during the outburst, valid timing solutions could be obtained for small time intervals spanning ∼100 days each during the recovery phase in 2006 and 2007 [Kuiper and Hermsen, 2009] until the pulsar eventually fully recovered its initial spin values. Observations with *RXTE* and *Chandra* [Livingstone et al., 2011], covering the post-outburst period until 2009, showed that the level of intrinsic timing noise has increased compared to the pre-outburst level. In addition, the braking index changed from $n = 2.65 \pm 0.01$ to $n = 2.15 \pm 0.03$, a decrease of $\sim 20\%$.

5.2 The H.E.S.S. Data Set

The region around Kes 75 and the pulsar PSR J1846−0258 was first observed in the years 2004 and 2005 during the H.E.S.S. survey of the Inner Galaxy [Aharonian et al., 2006c]. First indications of VHE γ-ray emission in the direction of Kes 75 triggered dedicated

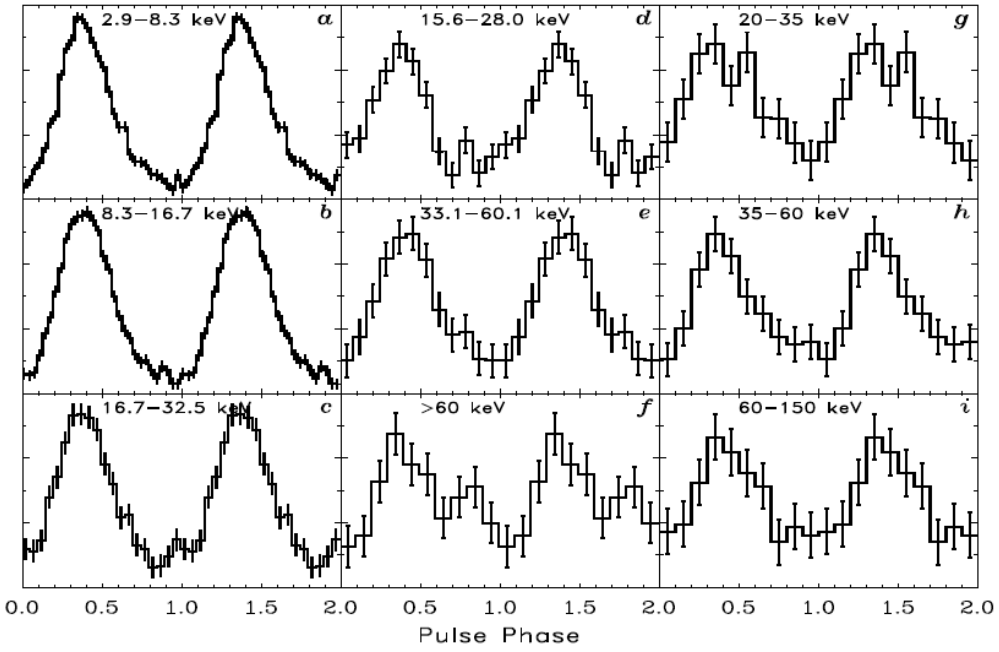

Figure 5.3 Pulsar light curves as observed for PSR J1846−0258 with *RXTE* (3−250 keV: a-f) and *INTEGRAL* (20−300 keV: g-i) before the X-ray outburst in 2006. The pulse profile consists of a broad single peak with an energy-independent pulse shape. The errors bars are 1σ on the measured counts. Taken from [Kuiper and Hermsen, 2009].

follow-up observations to firmly establish a signal. The follow-up observations were performed in the years 2006 and 2007 in *wobble mode* where the nominal target position is displaced from the system's pointing direction by an alternating offset angle ranging from 0.6° to 0.9°. Additionally, the data set largely benefited from observations with pointing offsets larger than 1.0° of nearby regions and the continuing H.E.S.S. survey of the Inner Galaxy in the years from 2006 to 2008. A summary of the observation periods for each year together with the resulting mean zenith and offset angles of the observations is shown in Table 5.1.

The detection of a faint VHE γ-ray source, cataloged as HESS J1846−029, with a peak significance of $10\,\sigma$ (for an integration radius of 0.1°) has been announced at the 30^{th} International Cosmic Ray Conference [Terrier et al., 2008]. The published data set amounts to 32 hours, covering the observation periods from 2004 to mid of 2007. The analysis presented in this thesis includes the total available data set, ranging from 2004 to 2008 and essentially doubling the observation time available for analysis.

A standard data quality selection procedure as described in Aharonian et al. [2006d] that excludes data taken under unstable weather conditions or with malfunctioning hardware from further analysis is applied to the total data set. As the detector acceptance for γ-ray-like events drops off at large angular distances to the center of the

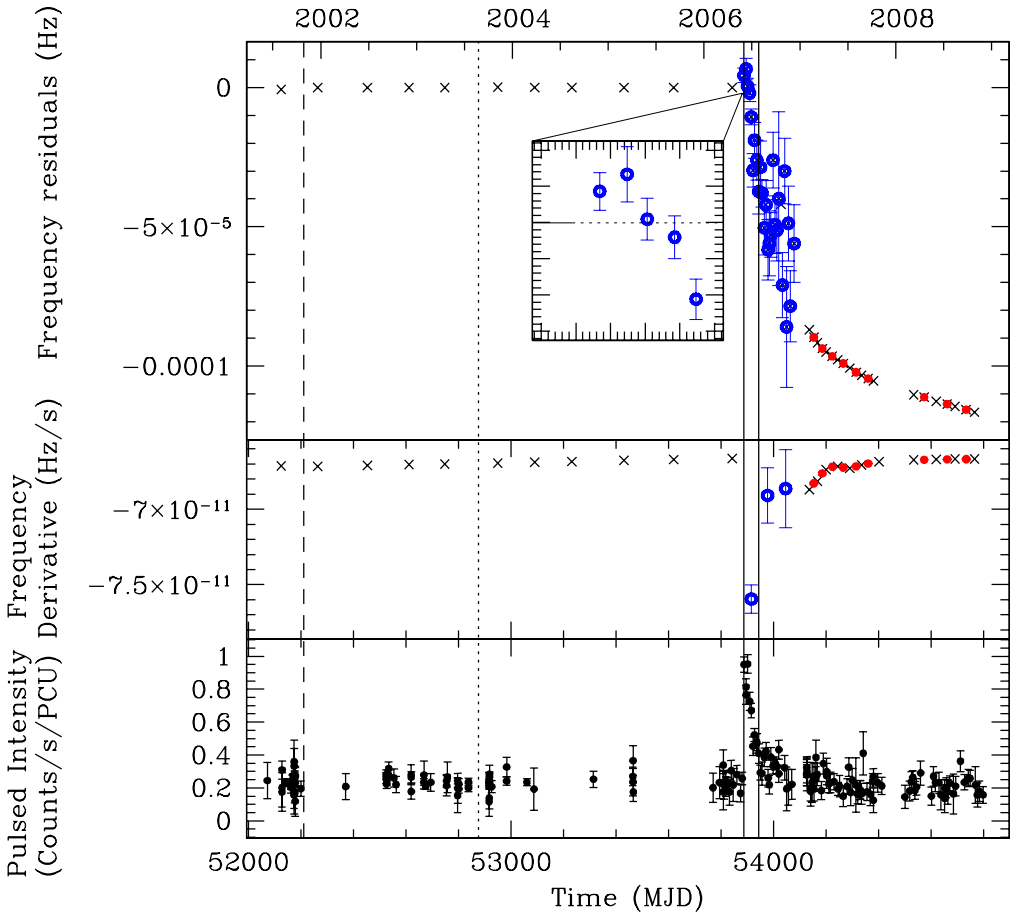

Figure 5.4 Timing parameters and the pulsed flux as observed with *RXTE* for ~ 8 years covering the pre-outburst, outburst and post-outburst phase. Shown are the spin frequency residuals ($\nu - \nu_0$) about the pre-glitch model frequency ν_0 (top panel) , the spin frequency derivative $\dot{\nu}$ (middle panel) and the pulsed flux in the $2 - 20$ keV energy band (bottom panel). Black crosses indicate timing measurements obtained with the epoch-folding technique for short segments of data, while filled red circles indicate timing measurements obtained with the same technique but for overlapping segments of data. A different technique has been used for obtaining the timing measurements for the outburst phase (blue open circles). The dashed and dotted lines represent dates of a small glitch and a glitch candidate, respectively, while the solid lines represent the dates of the bursts. Taken from [Livingstone et al., 2010].

field of view [Berge et al., 2007], the full data set with maximum pointing offsets of up to 3° has been used only for morphological studies (*morphology data set*). The mean pointing offset is 1.7°. The total live time of this data set amounts to 67.4 hours that corresponds to an acceptance-corrected live time, normalized to an offset of 0.7°, of 47.2 hours. For spectral and timing studies, observations with a maximum pointing offset of 2° were considered (*spectrum data set*). The mean pointing offset is 1.0° and the remaining acceptance-corrected live time is 40.4 hours (normalized to an offset of 0.7°). The acceptance-corrected live time of the good-quality *morphology* and *spectrum data sets* is shown in Table 5.1 for the whole observation period and for each year individually. The zenith angle of the observations taken between 2004 and 2008 ranges from 19° to 59°, with a mean zenith angle of 28°.

5.2.1 Data Quality

Shortly before this thesis was handed in, it was realized that some event time stamps in the calibrated data available for analysis (so-called DST files) are affected by a software bug in the standard H.E.S.S. DST production chain. This software bug caused a shift in the event time stamp by an integer of 3 to 5 seconds. In each DST, this shift was observed for the last 5% to 10% of the events. Unfortunately, it was not possible to solve this bug and reproduce the DSTs in time for this thesis.

The shift of the event time stamps does not influence the standard H.E.S.S. analysis to search for steady VHE γ-ray emission and the results presented in Section 5.4.1 are not affected. The analysis results of a search for pulsed γ-ray emission as presented in Section 5.4.2, however, are likely affected and should be handled with caution. In the calculation of the pulsar phase from the event time stamp, a shift in event time inevitably leads to a derived event phase that is not related to the actual spin-down behavior of the pulsar. It is expected that the affected event phases will contribute to the uniformly distributed background and thus cause a loss of sensitivity in the search for pulsed emission. Additionally, the upper limits on the number of pulsed excess events should be handled with care due to the increased background. Please note that this data quality problem affected at most 10% of the total number of events, and as a first approach, the upper limits on the number of pulsed excess events are increased by 10% in the following.

Year	Start Date (DD/MM)	End Date (DD/MM)	$\theta_{\mathrm{off,max}}$ (°)	$\langle\theta_{\mathrm{off}}\rangle$ (°)	Z_{min}–Z_{max} (°)	$\langle Z\rangle$ (°)	Runs	Live time (h)
Morphology Data Set								
2004	18/05	24/07	3.0	1.6	19-36	25.5	5	1.7
2005	11/06	24/09	3.0	1.3	19-55	26.3	18	6.5
2006	22/06	23/09	3.0	1.6	19-57	32.0	27	9.0
2007	22/04	16/08	3.0	1.5	19-59	28.4	74	25.6
2008	04/05	01/08	3.0	2.2	19-34	24.7	29	5.5
2004-08	18/05	01/08	3.0	1.7	19-59	28.1	153	47.2
Spectrum Data Set								
2004	18/05	30/05	2.0	1.1	19-36	25.2	3	1.3
2005	11/06	27/08	2.0	0.7	19-55	25.3	11	5.2
2006	22/06	23/09	2.0	1.1	19-57	31.2	19	8.3
2007	18/05	16/08	2.0	1.0	19-59	28.6	50	22.0
2008	28/07	01/08	2.0	0.9	19-34	25.9	8	3.7
2004-08	18/05	01/08	2.0	1.0	19-59	28.4	91	40.4

Table 5.1 Summary of the H.E.S.S. data sets available for morphological and spectral analysis. Shown are the observation period, the maximum pointing offset angle $\theta_{\mathrm{off,max}}$ used in the run selection, the mean pointing offset angle $\langle\theta_{\mathrm{off}}\rangle$, the zenith angle range $Z_{\mathrm{min}} - Z_{\mathrm{max}}$ and the mean zenith angle $\langle Z\rangle$ of the observations together with the number of runs in the corresponding observation period and its dead time and acceptance corrected live time, normalized to an offset of 0.7°.

5.3 Analysis technique

5.3.1 Search for Steady Emission

The data was analyzed using the standard H.E.S.S. analysis chain to search for steady emission from a point-like source as described in more detail in Section 3.3. A γ-hadron separation based on the Hillas parametrization was performed on the reconstructed events using two sets of cuts, *standard selection cuts* and *hard selection cuts*. The *hard selection cuts* require a minimum amplitude of 200 photo-electrons (ph.e.) for each recorded shower image. This requirement is stricter than the one used when applying *standard selection cuts* (80 ph.e.) and leads to a higher background suppression and improved angular resolution at the expense of a higher analysis energy threshold. The *hard selection cuts* are thus well suited for the study of the morphology of the VHE γ-ray emission from the sky region of interest. In spectral studies, a looser cut on the minimum image amplitude is used that allows for an extension of the energy range to lower energies. Thus, *standard selection cuts* are used for spectral studies giving a broader energy coverage. For the mean offset and zenith angle of the spectrum data set, the corresponding analysis energy thresholds are 360 GeV for *standard selection cuts* and 650 GeV for *hard selection cuts*, respectively.

Different methods of background estimation are used for the morphological and spectral studies. Two-dimensional sky images were produced for morphological studies using the *ring background* estimation method [Berge et al., 2007]. In this method, the background is estimated at each test position in the sky from a ring surrounding the test position with an inner ring radius of 0.5° and an area which is 16 times the area of the circular signal region which has a radius of 0.11°. For spectral studies, the energy spectrum was extracted from a circular signal region of 0.11° radius and centered at the nominal position of the pulsar. The background in the signal region was estimated within the *reflected region background* model [Berge et al., 2007], where background regions of the same size and same offset to the camera center as the signal region are used. In both methods, all regions with a known γ-ray source are excluded from the background regions to avoid γ-ray contamination of the background estimates. More details of the background estimation methods can be found in the Section 3.3.4.

5.3.2 Search for Pulsed Emission

A timing analysis with phase-folding as described in Section 3.5 was applied to the selected γ-like events from the direction of the pulsar to search for hints of pulsed emission. The γ-ray events were selected with *standard selection cuts* from the same circular signal region centered on the nominal position of the pulsar that was also used for spectral studies. The search for pulsed emission has been performed on the selected γ-like events in two a-priori defined energy bands (below and above 500 GeV) and in the whole energy range.

The ephemerides used in the phase-folding procedure were taken from published timing solutions obtained with *RXTE* in the X-ray energy band [Kuiper and Hermsen, 2009,

Livingstone et al., 2011]. As already detailed in Section 5.1.3, PSR J1846−0258 showed a glitch in periodicity in 2006, followed by a recovery phase of the initial periodicity during the years 2007 and 2008. Coherent timing solutions are thus only available for limited time intervals during and after the outburst, leaving gaps of unpredictable timing behavior. For the timing analysis, the H.E.S.S. *spectrum data set* is therefore split in data sets for which contemporaneous timing solutions are available. The valid ephemerides together with the H.E.S.S. data sets are shown in Table 5.2. Apart from the H.E.S.S. observation period of 2006 where the data set is nearly halved, the H.E.S.S. *spectrum data set* of each year is fully covered by a contemporaneous timing solution. The timing analysis was first applied to each data set individually to generate pulsar light curves. The phase of each γ-like event was calculated according to the respective timing solution. The reference phase, given in Table 5.2 for each timing solution, has been subtracted from each event phase to allow for absolute phase alignment. The peak of X-ray emission is thus expected at the phase position 0.0 for each data set. The phase distribution for the total 2004-2008 data set is then the combination of the individual phase distributions (*phase coherent combination*). It should be noted, however, that the reference phase for 2008 is not given in Livingstone et al. [2011] and a value has been deduced from inspection of the light curve which is to some extent uncertain.

Timing Solution							H.E.S.S. Data Set	
Start	End	Epoch (MJD,TDB)	ν (Hz)	$\dot{\nu}$ (10^{-11}Hz/s)	$\ddot{\nu}$ (10^{-21}Hz/s^2)	Φ_0	Runs	Live time (h)
26/01/2004	05/04/2005	53030.0	3.0726185382(34)	-6.69068(3)	3.93(2)	0.5030	3	1.3
04/04/2005	23/05/2006	53464.0	3.0701124555(45)	-6.67599(4)	3.78(3)	0.8985	11	5.2
31/08/2006	25/10/2006	53997.0	3.0669883665(67)	-6.8688(7)	161(15)	0.3092	10	4.5
17/05/2007	28/08/2007	54237.0	3.065565121(15)	-6.7297(7)	15(2)	0.9120	50	22.0
27/01/2008	22/04/2010	54834.0	3.0621185502(4)	-6.664350(2)	2.725(3)	0.2	8	3.7

Table 5.2 Timing solutions for the pulsar's spin-down behavior found with *RXTE* by Kuiper and Hermsen [2009] covering the years from 2004 to 2007 and by Livingstone et al. [2011] covering 2008. Given are the epoch in units of MJD in the TDB time system, the pulsar frequency and its derivatives, and the reference phase Φ_0 where available. The reference phase denotes the phase where the peak of the pulsed signal is expected for each timing solution and can be used to combine phases calculated with the different timing solutions. As the reference phase was not given in Livingstone et al. [2011], a value of 0.2 was deduced from inspection of the pulsar light curve. A summary of the H.E.S.S. data sets available for the timing analysis is also shown. The H.E.S.S. data set equals the *spectrum data set* as introduced in Section 5.2 apart from the 2006 data set where the H.E.S.S. observation period is only partly covered by the concurrent timing solution and the amount of available data nearly halved.

5.4 Results

5.4.1 Steady Emission

Figure 5.5 shows an acceptance-corrected event excess count map within a field of view of $(0.5^\circ \times 0.5^\circ)$ and a bin size of $(0.01^\circ \times 0.01^\circ)$ surrounding the nominal pulsar position as derived from the $2004-2008$ *morphology data set* with *hard selection cuts* and the *ring background* method. The excess map was smoothed with a Gaussian kernel of width 0.04°, roughly matching the H.E.S.S. PSF of 0.07°, to reduce statistical fluctuations. The significance at each sky position was calculated with an integration radius of 0.09°, roughly matching the 0.11° radius of the signal region, and significance contours for $8\,\sigma$, $9\,\sigma$, and $10\,\sigma$ are overlaid on the H.E.S.S. excess map in Fig. 5.5. A clear excess is observed from the direction of Kes 75 with a peak statistical significance of $10.8\,\sigma$.

Figure 5.6 shows the H.E.S.S. significance contours ($8\,\sigma$, $9\,\sigma$ and $10\,\sigma$ level) overlaid on the *Chandra* $1-7\,\mathrm{keV}$ X-ray count map. Both the PWN and the SNR shell are spatially coincident with the VHE emission. A fit to the unsmoothed excess count map with a radially symmetric Gaussian profile ($\rho \propto e^{-\theta^2/(2\,\sigma_\mathrm{w}^2)}$), convolved with the H.E.S.S. PSF for this data set, was used to obtain the position and extent of the VHE emission. The best fit source position is ($\alpha = 18^\mathrm{h}46^\mathrm{m}22.67^\mathrm{s} \pm 3.1^\mathrm{s}, \delta = -2^\circ57'59.7'' \pm 43.5''$) (J2000 coordinate system) with statistical errors given for each coordinate and shown in Fig. 5.5. The probability of the fit is 26% with a reduced χ^2 of 72.9/66. The best fit position is compatible with both the nominal pulsar position and the centroid of the γ-ray emission at a $1\,\sigma$ confidence level. The intrinsic width of the Gaussian is $0.016^\circ \pm 0.022^\circ$ and is consistent with a point-like emission. The FWHM of the intrinsic width of 0.038° or 2.3' is comparable to the radio shell size of Kes 75.

The analysis of the $2004-2008$ *spectrum data set* using the *reflected region background* method with *standard selection cuts* and a circular signal region of 0.11° radius centered on the nominal pulsar position results in a clear VHE γ-ray signal of 406 ± 50 excess events corresponding to $8.5\,\sigma$ significance. The photon spectrum between 360 GeV and 20 TeV is well described by a power law ($\mathrm{dN/dE} = \Phi_0\ (\mathrm{E}/1\,\mathrm{TeV})^{-\Gamma}$) with a photon index of $\Gamma = 2.45 \pm 0.17_\mathrm{stat} \pm 0.2_\mathrm{sys}$ and a flux normalization of $\Phi_0 = (5.8 \pm 0.9_\mathrm{stat}) \times 10^{-13}\,\mathrm{TeV}^{-1}\,\mathrm{cm}^{-2}\,\mathrm{s}^{-1}$. The fit has a reduced χ^2 of 3.8/4 and a probability of 43.9%. The differential energy spectrum together with the power-law fit and the residuals are shown in Fig. 5.7. Additionally, the error contours of the fit parameters are given as an inlay in Fig. 5.7. The spectrum is within $1\,\sigma$ errors consistent with the measurement by Terrier et al. [2008]. The integral flux above 1 TeV is $F_\gamma = (4.0 \pm 0.8_\mathrm{stat} \pm 0.3_\mathrm{sys}) \times 10^{-13}\,\mathrm{erg\,cm^{-2}\,s^{-1}}$ and corresponds to 1.8% of the flux of the Crab Nebula in the same energy band.

For the comparison of the flux measurements with those found for other VHE sources, it is conventional to derive the integral flux measurements within energy bands ranging from 1 TeV to 10 TeV and from 1 TeV to 30 TeV. The integral flux measurements for the two energy bands are given in Table 5.3. The integral VHE luminosity in the energy range between 1 TeV and 10 TeV, evaluated for the distance of 6 kpc, is $L_\gamma = (5.8 \pm 0.8_\mathrm{stat}) \times 10^{33}\,\mathrm{erg\,s^{-1}}$ and the corresponding efficiency of converting the pulsar's spin-down power

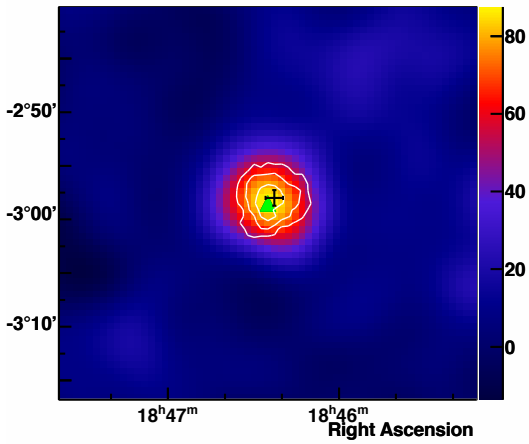

Figure 5.5 Smoothed VHE γ-ray excess map of the $0.5° \times 0.5°$ region centered on Kes 75. The size of bins is $0.01° \times 0.01°$. The map was smoothed with a 0.04° Gaussian kernel to reduce statistical fluctuations. The linear color scale is in units of excess counts integrated within the smoothing radius. The $8\,\sigma$, $9\,\sigma$ and $10\,\sigma$ significance contour levels are overlaid as white lines. The significance levels have been determined from an integration region with a radius of 0.09°. A point-like emission, HESS J1846−029, is detected at the 10σ level. The best fit position of HESS J1846−029 together with its statistical errors is shown as a black point and the position of PSR J1846−0258 is marked by a green triangle.

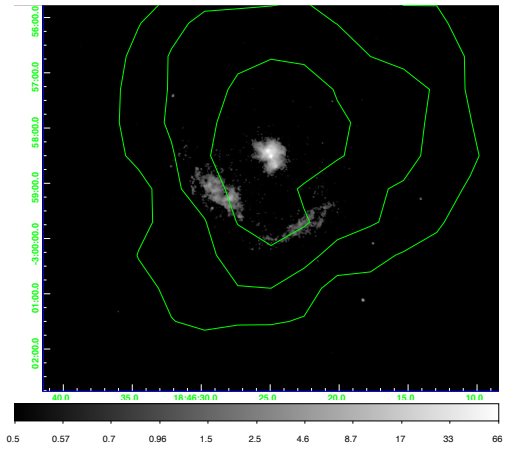

Figure 5.6 Smoothed X-ray map of the Kes 75 region as observed in the 1.0 keV to 7.0 keV energy band with *Chandra* (logarithmic intensity scale). The X-ray map was reproduced from Helfand et al. [2003] (see also Fig. 5.1 (b)) using a different smoothing radius and color scale. The H.E.S.S. significance contours at the $8\,\sigma$, $9\,\sigma$ and $10\,\sigma$ level (same as in Fig. 5.5) are overlaid as green lines. The coordinates are given in RA and Dec (J2000) on the abscissa and ordinate, respectively.

Energy Range	$> 0.36\,\mathrm{TeV}$	$1 - 10\,\mathrm{TeV}$	$1 - 30\,\mathrm{TeV}$
F_γ $(10^{-13}\,\mathrm{cm^{-2}\,s^{-1}})$	$17.5 \pm 2.9_{\mathrm{stat}}$	$3.8 \pm 0.7_{\mathrm{stat}}$	$3.9 \pm 0.8_{\mathrm{stat}}$
G_γ $(10^{-12}\,\mathrm{erg\,cm^{-2}\,s^{-1}})$	$3.0 \pm 0.4_{\mathrm{stat}}$	$1.3 \pm 0.2_{\mathrm{stat}}$	$1.6 \pm 0.3_{\mathrm{stat}}$
Distance	6 kpc		
L_γ $(10^{33}\,\mathrm{erg\,s^{-1}})$	$13.0 \pm 1.7_{\mathrm{stat}}$	$5.8 \pm 0.8_{\mathrm{stat}}$	$7.0 \pm 1.2_{\mathrm{stat}}$
η_γ (%)		$0.11 \pm 0.02_{\mathrm{stat}}$	$0.14 \pm 0.02_{\mathrm{stat}}$
Distance	10.6 kpc		
L_γ $(10^{33}\,\mathrm{erg\,s^{-1}})$	$40.7 \pm 5.4_{\mathrm{stat}}$	$17.9 \pm 2.5_{\mathrm{stat}}$	$21.8 \pm 3.6_{\mathrm{stat}}$
η_γ (%)		$0.35 \pm 0.05_{\mathrm{stat}}$	$0.43 \pm 0.07_{\mathrm{stat}}$

Table 5.3 Integral Flux measurements for the 1 TeV to 10 TeV and the 1 TeV to 30 TeV energy band as obtained from the *spectrum data set* using *standard selection cuts* and the *reflected region background* method with a 0.11° circular signal region centered on the nominal pulsar position. Shown are the integral flux F_γ and the integral energy flux G_γ together with the corresponding integral luminosity $L_\gamma = (4\pi d^2 G_\gamma)$ and apparent conversion efficiency $\eta_\gamma = L_\gamma/\dot{E}$, evaluated for a spin-down power of $\dot{E} = 8.3 \times 10^{36}\,\mathrm{erg\,s^{-1}}$ and two distances of 6 kpc and 10.6 kpc.

$\dot{E} = 8.3 \times 10^{36}\,\mathrm{erg\,s^{-1}}$ to VHE γ-ray emission is $\eta_\gamma = L_\gamma/\dot{E} = (0.11 \pm 0.02_{\mathrm{stat}})\,\%$. The VHE luminosity and conversion efficiency are also given in Table 5.3 together with those evaluated at the larger distance of 10.6 kpc.

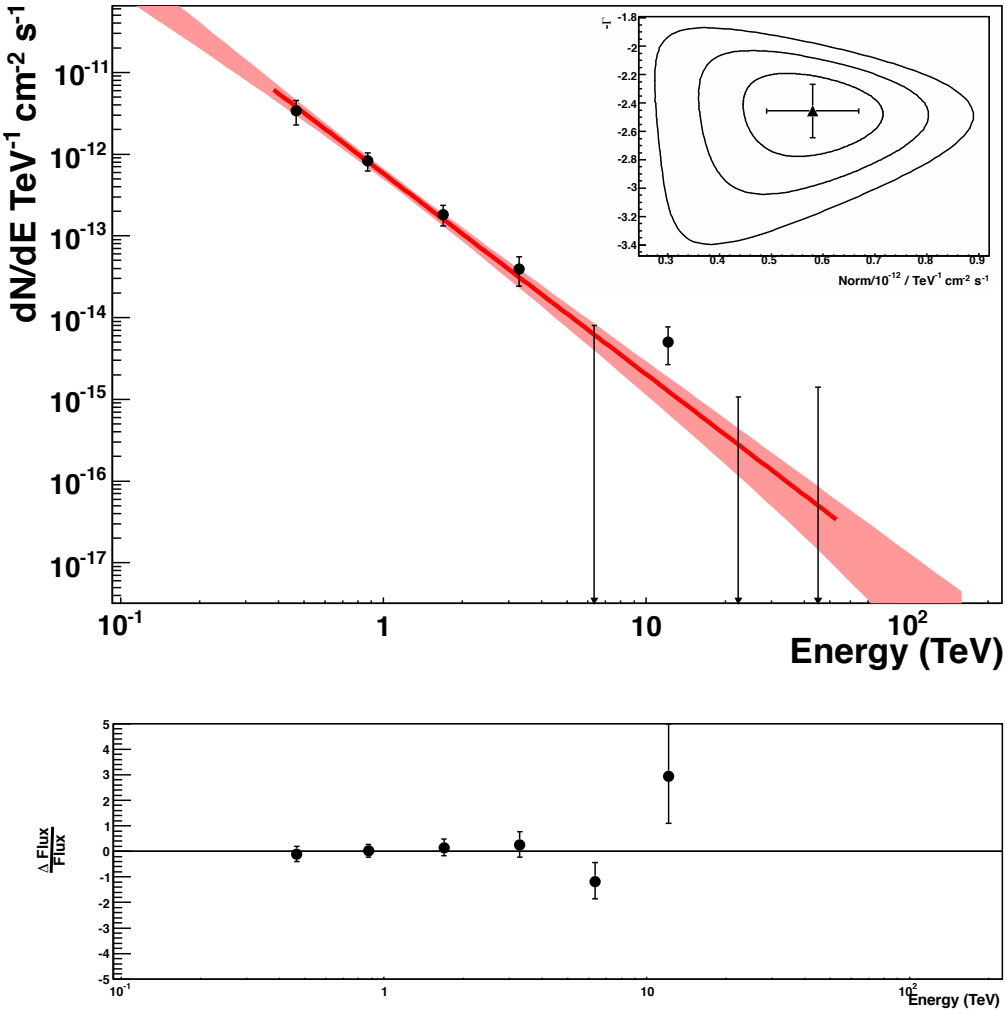

Figure 5.7 Differential energy spectrum of the TeV γ-ray source in the direction of Kes 75 as derived with H.E.S.S. (upper panel). The spectrum is well described by a power law with a photon index of $\Gamma = 2.45 \pm 0.17_{\mathrm{stat}} \pm 0.2_{\mathrm{sys}}$ and a flux normalization of $\Phi_0 = (5.8 \pm 0.9_{\mathrm{stat}}) \times 10^{-13}\,\mathrm{TeV}^{-1}\,\mathrm{cm}^{-2}\,\mathrm{s}^{-1}$. The power-law fit is shown as a solid red line and the $1\,\sigma$ error contours are indicated with a shaded band. The flux residuals, i.e the deviation of the flux points from the power-law fit, are shown in the bottom panel. The $1\,\sigma$, $2\,\sigma$ and $3\,\sigma$ error contours of the fit parameters, i.e. the photon index and normalization, are shown as an inlay.

Year	N_{on}	χ^2/ndf	P_{χ^2}	H	P_{H}	σ_{H}	$N_{3\,\sigma_{\mathrm{ul}}}$	$N_{3\,\sigma_{\mathrm{ul,cor}}}$
2004	119	6.9/9	0.64	2.4	0.39	0.9	36	40
2005	355	27/9	0.0014	19.0	0.0005	3.5	102	112
2006	146	20/9	0.016	7.9	0.04	2.0	47	52
2007	1058	18/9	0.031	8.7	0.03	2.2	131	144
2008	173	9.2/9	0.42	3.1	0.29	1.0	49	54
2004-07	1559	16/9	0.076	7.3	0.05	1.9	158	174
2004-08	1732	12/9	0.20	5.4	0.12	1.6	156	172

Table 5.4 Results of the search for periodicity in the phase distribution of γ-ray-like events from the signal region around the pulsar PSR J1846−0258 for the data sets from each year and the combined data sets, for all energies. The number of selected γ-ray-like events, N_{on}, are shown together with results of a fit of a constant to the pulsar light curve (χ^2/ndf and probability P_{χ^2} of being consistent with a uniform distribution). Additionally, the H-test value H is given with the probability of obtaining such value, P_{H}, the corresponding significance for a pulsed signal, σ_{H}, and $3\,\sigma$ upper limit on the number of pulsed events, $N_{3\,\sigma_{\mathrm{ul}}}$. In the last column, the $3\,\sigma$ upper limits are given with a 10% correction as discussed in Section 5.2.1.

5.4.2 Pulsed Emission

The pulsar light curves, obtained in each observation period for which a contemporaneous timing solution was available, are shown in Fig. 5.8 for the whole energy range. A bin width of 0.1 in phase was used for the construction of the light curves. Each light curve was aligned in absolute phase so that the position of the X-ray peak corresponds to a phase of 0.0. The light curves show various patterns of statistical fluctuations and no clear identification of a pulsed component that is present at the same phase position in all light curves from 2005 to 2008 is possible. The pulsar light curve for the total 2004-2008 data set, constructed from a phase-coherent addition of the individual light curves is also shown in Fig. 5.8 (bottom row).

To estimate any pulsed signal present in the phase distribution for each observation period, the χ^2-probability of a fit of a constant to the binned pulsar light curve (shown as a solid line in each pulsar light curve in Fig. 5.8) and the H-value calculated for the unbinned phase distribution were estimated. The results are shown in Table 5.4. The pulsar light curves for the observation periods 2004 and 2006 to 2008 are well described by a constant (the χ^2-probability of the fit is not less than 1%) and an H-value below 9 (corresponding to a significance of $\sim 2.5\,\sigma$) was found for each of these periods. Only the data set of 2005, prior to the pulsar X-ray outburst, shows some hints of pulsed emission with an H-value of 19 ($3.5\,\sigma$). The examination of the pulsar light curve of this observation period (Fig. 5.8), guided by eye, shows no peak in coincidence with the X-ray peak position, but fluctuations are present. The timing analysis for this observation period has been repeated for two restricted energy ranges $E < 500\,\mathrm{GeV}$ and $E > 500\,\mathrm{GeV}$, resulting in H-values in each of the individual analyses below 9 ($\sim 2.5\,\sigma$). Thus, no firm conclusion on any pulsed signal present within the 2005 data set can be

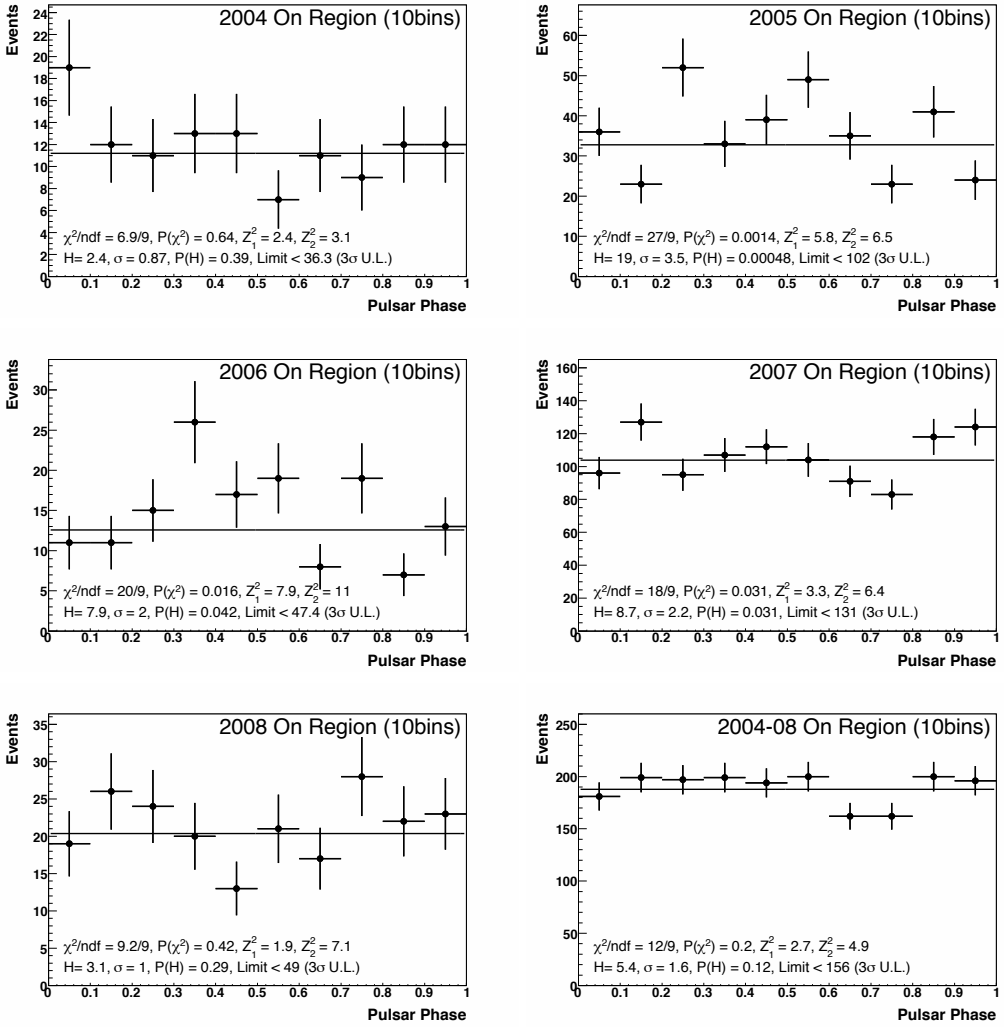

Figure 5.8 Pulsar light curves for the ON region around PSR J1846−0258 for the annual observation periods from 2004 to 2008 and the total 2004-2008 data set. The errors bars are 1σ on the measured counts. The horizontal line indicates a fit to a constant to the respective pulsar light curve.

drawn, due to limited statistics. The phase distribution for the total 2004-2007 data set, phase-coherently added using the reference phase given for each observation period in the corresponding timing solution, gives an H-value of 7.3 with significance of $1.9\,\sigma$, consistent with a uniform distribution. When combined with the 2008 data set for which the reference phase is not accurately known, the H-value reduces to 5.4 with a significance of $1.6\,\sigma$. The $3\,\sigma$ upper limit on the number of pulsed excess events is 156 (172 after the correction as described in Section 5.2.1), corresponding to $\sim 10\%$ of all γ-ray like events from the direction of PSR J1846−0258. As a cross-check, the same analysis has been applied to the events from the background regions for each data set. The resulting H-values are in the range from 0.6 ($0.3\,\sigma$) to 2.4 ($0.9\,\sigma$), consistent with the assumption of a uniform distribution of event phases.

5.5 Discussion

A range of possible counterparts can be put forward to explain the origin of the VHE emission from the direction of the composite SNR Kes 75. These scenarios include VHE emission from the PWN and/or from the SNR shell. In the following, the results found for steady VHE emission from the direction of Kes 75 will be discussed in the context of a leptonic scenario for the PWN and a hadronic scenario for the SNR origin. In a second part of this section, the results of the search for periodic emission from the pulsar will be set in context of what is known about γ-ray pulsars.

5.5.1 Steady Emission

In a viable picture of the counterpart powering the VHE emission, the counterpart has to fulfill several requirements. These are: a spatial and morphological coincidence with the VHE emission and an energy budget provided within the respective scenario that gives a viable γ-ray emission mechanism with respect to the population of accelerated particles and properties of the environment such as magnetic field distribution and ambient medium density.

PWN origin

The good spatial coincidence of the VHE source with the pulsar PSR J1846−0258 and its confirmed X-ray PWN, located at the center of Kes 75, make the PWN a good candidate to be tested as a counterpart of the γ-ray emission.

Many VHE sources with an identified PWN counterpart seen with H.E.S.S. are extended beyond the H.E.S.S. point spread function, giving typical nebula sizes of some 10 pc, and are often displaced from the pulsar position by several arc-minutes. Such extended emission is typical for VHE PWNe, e.g. HESS J1825−137 [Aharonian et al., 2006a] and HESS J0835−455 (Vela X) [Aharonian et al., 2006b], that are powered by energetic pulsars with a spin-down power of $\dot{E} \sim 10^{34-36}\,\mathrm{erg\,s^{-1}}$ and characteristic ages of $\tau_\mathrm{c} > 10^4$ years, significantly larger than the age of Kes 75. The morphological characteristics observed for Kes 75 of a point-like VHE emission in good spatial coincidence

with the nominal position of the pulsar and its surrounding X-ray PWN are typical of what is observed for VHE PWNe powered by young ($\tau_c \sim 1000$ years) and very energetic ($\dot{E} \sim 10^{36-38}\,\mathrm{erg\,s^{-1}}$) pulsars, e.g. the Crab Nebula [Aharonian et al., 2006d] and HESS J1833−105 (G21.5−0.9) [Djannati-Ataï et al., 2008]. With a spin-down power of $\dot{E} = 8.3 \times 10^{36}\,\mathrm{erg\,s^{-1}}$ and a characteristic age of $\tau_c = 723$ years, PSR J1846−0258 falls into the latter category of pulsars and would be the youngest pulsar powering a VHE PWN known to date.

A first criterion to test for a viable **pulsar energy budget** for powering the VHE source is the spin-down energy flux $\dot{E}/d^2$. In a systematic search for VHE counterparts of energetic pulsars using the H.E.S.S. Galactic Plane Survey and a sample of 435 radio pulsars selected from the ATNF Catalogue, it was found that pulsars with a high spin-down energy flux $\dot{E}/d^2 > 10^{35}\,\mathrm{erg\,s^{-1}\,kpc^{-2}}$ are viable candidates for being detectable as VHE γ-ray emitters [Carrigan et al., 2008]. The spin-down flux $\dot{E}/d^2$ of PSR J1846−0258, evaluated for a distance of 6 kpc, is $2.3 \times 10^{35}\,\mathrm{erg\,s^{-1}\,kpc^{-2}}$ and exceeds $10^{35}\,\mathrm{erg\,s^{-1}\,kpc^{-2}}$. Evaluated at the larger distance of 10.6 kpc, the spin-down flux is $7.2 \times 10^{34}\,\mathrm{erg\,s^{-1}\,kpc^{-2}}$ and is still close to $10^{35}\,\mathrm{erg\,s^{-1}\,kpc^{-2}}$. Thus, PSR J1846−0258 is a very powerful pulsar, albeit less powerful than the Crab pulsar (by a factor of 58) or the pulsar PSR J1833−1034 in HESS J1833−105 (by a factor of 4). Another criterion for a viable pulsar energy budget for powering the VHE source is the apparent efficiency, $\eta_\gamma = L_\gamma/\dot{E}$, for converting the pulsar's spin-down power to the detectable VHE emission. The VHE luminosity in the 1 TeV to 10 TeV energy band and for a distance of 6 kpc (10.6 kpc) is $L_\gamma = (5.8 \pm 0.8_{\mathrm{stat}}) \times 10^{33}\,\mathrm{erg\,s^{-1}}$ ($L_\gamma = (17.9 \pm 2.5_{\mathrm{stat}}) \times 10^{33}\,\mathrm{erg\,s^{-1}}$). The corresponding γ-ray conversion efficiency of $\eta_\gamma = (0.11 \pm 0.02_{\mathrm{stat}})\,\%$ ($\eta_\gamma = (0.35 \pm 0.05_{\mathrm{stat}})\,\%$) is in the range of the conversion efficiencies seen from other VHE γ-ray sources which are identified as VHE PWNe (see e.g. Table 1 in Hessels et al. [2008]), but smaller than the average conversion efficiency in this sample ($\sim 1\%$). It should be noted, however, that this is not unexpected as young PWNe such as the Crab Nebula ($\eta_\gamma \sim 0.009\%$) and HESS J1833−105 ($\eta_\gamma \sim 0.008\%$) are rather inefficient VHE emitters. PSR J1846−0258 is thus energetically capable of powering a VHE PWN.

Most of the detected VHE PWNe are accompanied by an X-ray PWN that is believed to be connected to the VHE γ-ray emission via the parent population of accelerated particles. The emerging sample of X-ray/VHE PWNe allowed for first correlation studies, e.g. Mattana et al. [2009] and Kargaltsev and Pavlov [2010], connecting the observed X-ray and VHE luminosities L_X and L_γ with properties such as $\dot{E}$ and τ_c of the pulsar powering these sources. In the study put forward by Mattana et al. [2009] for a sample of 14 X-ray/VHE PWNe, it was found that while the VHE PWN luminosity L_γ in the energy band of 1 TeV to 30 TeV is weakly correlated to $\dot{E}$ and τ_c, the X-ray PWN luminosity L_X in the energy band of 2 keV to 10 keV increases with increasing spin-down power ($\propto \dot{E}^{1.9}$) and decreasing characteristic age ($\propto \tau_c^{-2.5}$). Consequently, the ratio of VHE-to-X-ray flux F_g/F_X is anti-correlated with the spin-down power ($\propto \dot{E}^{-1.9}$) and is proportional to the characteristic age ($\propto \tau_c^{2.2}$). See also Section 2.2.4.

The assumption of the model of Mattana et al. [2009] that the X-ray emitting particles are in the cooled regime, while the VHE emitting particles are in the uncooled regime, might not hold for such a young PWN as Kes 75. In this system, the X-ray emission and VHE emission may be rather limited by the age of the system than by the lifetime of the emitting particles, except for strong magnetic field strengths such as that of the Crab Nebula (140 μG).

The observed X-ray and VHE PWN luminosity are compared to the predictions from the relations found by Mattana et al. [2009] and presented in Sec. 2.2.4. Kes 75, interpreted as a PWN, was already part of this study, using X-ray measurements obtained from Helfand et al. [2003] and the first H.E.S.S. measurements presented in Terrier et al. [2008]. The following comparison of measured values for $L_{\rm X}$, L_γ and $F_\gamma/F_{\rm X}$ with those estimated from the scaling laws for $\dot{E}$ and $\tau_{\rm c}$ are thus not completely independent from the correlation study. It can be noted that while the spin-down power of PSR J1846−0258 is in the middle of the range observed from the total sample of pulsars used in this study ($\dot{E} = 8.3 \times 10^{36}\,{\rm erg\,s^{-1}}$ vs $3 \times 10^{35} - 5 \times 10^{38}\,{\rm erg\,s^{-1}}$), PSR J1846−0258 is the youngest (723 years vs $1.2 - 90 \times 10^3$ years) and one of the more distant (6 kpc vs $0.3 - 6.7$ kpc) objects in the sample. Set at a distance of 10.6 kpc, it would be by a factor of ~ 2 more distant than any other pulsar used in this study. In the following, the measured values and those estimated from the scaling laws will be denoted by a superscript m and e, respectively.

Kes 75 is a strong emitter at X-ray energies with an X-ray PWN luminosity in the energy band of $2 - 10$ keV of $1.1 \times 10^{35}\,{\rm erg\,s^{-1}}$ at a distance of 6 kpc ($3.0 \times 10^{35}\,{\rm erg\,s^{-1}}$ at a distance of 10.6 kpc) that is only surpassed by that of the Crab Nebula in the same energy band (by a factor of 90 (30)). The corresponding conversion efficiency is 1.3% (3.8%) that is again similar only to that of the Crab Nebula (2%) while all other PWNe within the sample have much lower X-ray conversion efficiencies (~ 0.01%).

From the relations connecting the X-ray PWN luminosity with $\dot{E}$ and $\tau_{\rm c}$ it is found that the measurements for PSR J1846−0258 deviate more from the scaling laws than for any other pulsar in the sample. The pulsar is more luminous in the X-ray energy band than estimated from the $L^e_{\rm X} - \dot{E}$ relation (by a factor of ~ 23) and less luminous than estimated from the $L^e_{\rm X} - \tau_{\rm c}$ relation (by a factor of ~ 34). The ratio of measured to estimated X-ray PWN luminosity is not independent of the distance as $L^m_{\rm X} \propto d^2$. Thus, it is possible to estimate the distance that equalizes the measured and estimated luminosities as $d = (L^e_{\rm X}/L^m_{\rm X})^{1/2}\,6\,{\rm kpc}$. The relation for $\dot{E}$ points to a distance of ~ 1 kpc, closer than the assumed distance of 6 kpc, while the relation for $\tau_{\rm c}$ would put the pulsar at a much farther distance of ~ 35 kpc. Thus, although the distance to PSR J1846−0258 is debated in the literature with values ranging from 5 kpc up to 20 kpc, it is not possible to reconcile the discrepancies found for the $L^e_{\rm X} - \dot{E}$ and $L^e_{\rm X} - \tau_{\rm c}$ relations by rescaling the pulsar distance.

The ratio of VHE-to-X-ray PWN luminosity $L_\gamma/L_{\rm X} = F_\gamma/F_{\rm X}$ is independent of the distance. The value of this ratio is 1/11 for Kes 75 and is smaller than unity only for PWNe powered by young pulsars such as the Crab Nebula with a ratio of 1/262, HESS J1833−105 with 1/17 and MSH 15−52 with 1/1.4. The measured ratio is larger

than the ratio estimated from the $(L_\gamma/L_\mathrm{X})^e - \tau_\mathrm{c}$ relation by a factor of 2. It is within the scatter observed for the rest of the sample of pulsars. In contrast to what is observed for the sample of detected PWNe, the measured ratio is by a factor of ~ 60 smaller than what is estimated from the scaling law for $(L_\gamma/L_\mathrm{X})^e - \dot{E}$ and deviates more from this relation than any other PWN in the sample. Given its $\dot{E}$, PSR J1846−0258 should be less luminous in the X-ray band and/or more luminous in the VHE energy band than observed. Besides the large scatter and uncertainties that are inherent to such correlation studies using a limited sample of objects, the relations might not hold for Kes 75 due to its peculiarities as being the youngest and most distant object within a sample of PWNe that collects PWNe of different evolutionary stage, age and magnetic field strength.

In the following, the leptonic scenario is further tested with general equations as described in more detail in Section 2.2.4, connecting the X-ray and VHE emission via the parent population of electrons. Thereby, the strength of the magnetic field within the nebula and the total energy in electrons is estimated.

A rough estimate of the strength of the magnetic field can be derived assuming equipartition of particle and magnetic field energy in the PWN and an equipartition value of $B_\mathrm{eq} = 40\,\mu$G has been found from X-ray measurements [Ng et al., 2008]. Another estimate of the magnetic field can be derived from the ratio of the VHE-to-X-ray flux. This ratio is, under the assumption of isotropic pitch angles and a uniform distribution of the magnetic field within the nebula, determined by the ratio of the energy density in the magnetic field and in the IC photon target field according to Eq. 2.25.

The CMB provides a uniformly distributed minimum target photon density for IC. The measured ratio of X-ray-to-VHE flux of $L_\gamma/L_\mathrm{X} = 1/11$ corresponds to a magnetic field of $B \sim f_\mathrm{KN}^{1/2}\,11\,\mu$G, where f_KN is the Klein-Nishina (KN) suppression factor. The magnetic field slightly reduces to $9\,\mu$G when a suppression factor of (2/3) is used for transition to the KN regime in the H.E.S.S. energy range (see also Aharonian et al. [2006a]). The derived value for the magnetic field is three to four times larger than the average magnetic field strength in the ISM ($3\,\mu$G) and lower than the magnetic field of the Crab nebula of $140\,\mu$G and lower than the value of $100\,\mu$G as estimated by Morton et al. [2007].

A higher magnetic field can be deduced when probing photon radiation fields with higher photon target energy, where the IC process is more efficient as lower electron energies are needed for the same level of IC flux. As pointed out by Bucciantini et al. [2011], a stronger radiation field than provided by the CMB is also supported by the steeper photon index of $\Gamma = 2.45 \pm 0.17_\mathrm{stat} \pm 0.2_\mathrm{sys}$ as measured by H.E.S.S. when compared to the index of the X-ray flux of 1.9. Such steepening is not expected for standard cooling scenarios. Furthermore, Bucciantini et al. [2011] modeled the spectral energy distribution of Kes 75 as observed from the radio through the VHE waveband using the first H.E.S.S. measurements by Terrier et al. [2008] in a time-dependent leptonic model tracing the evolution of the PWN inside the SNR. They concluded that a local enhancement in the IR energy range is needed to correctly reproduce the VHE γ-ray flux. In the case of Kes 75, the infrared component of the interstellar (dust) field, provided by the

SNR shell or nearby molecular clouds, can provide such an enhanced target photon field and its energy density is estimated from Spitzer measurements [Morton et al., 2007] as $0.8\,\mathrm{eV\,cm^{-3}}$ at the center of Kes 75 (R. Terrier, private communication). The IC losses on the diffuse infrared radiation field are strongly suppressed in the KN regime and a KN suppression factor of (1/3) is used for the H.E.S.S. energy range. The resulting energy density in the radiation field is $f_{\mathrm{KN}}\,U_{\mathrm{CMB+IR}} = ((2/3)\times 0.26 + (1/3)\times 0.8)\,\mathrm{eV\,cm^{-3}}$. The magnetic field is then $14\,\mu$G, still well below the equipartition value B_{eq}. The PWN of PSR J1846−0258 is thus particle-dominated (see also Chevalier [2005]).

The total energy in electrons can be deduced from the integral γ-ray luminosity above the threshold energy $L_\gamma(>0.36\,\mathrm{TeV}) = (13.0\pm 1.7_{\mathrm{stat}})\times 10^{33}\,\mathrm{erg\,s^{-1}}$. A rough estimate of the total energy is

$$W_{\mathrm{e,tot}}(>E_{\mathrm{e}}) \sim t \times L_\gamma, \tag{5.1}$$

where t is the characteristic cooling timescale of the system. Under the assumption that all VHE photons are produced in a leptonic scenario via IC on CMB, the electrons responsible for the VHE emission have energies $E_{\mathrm{e}} > 10\,\mathrm{TeV}$ (see also Eq. 2.19). Using the SR cooling timescale of ~ 6000 years (evaluated according to Eq. 2.23 for a photon energy of 0.36 TeV and a magnetic field of $15\,\mu$G) as the maximum lifetime of the electrons responsible for the VHE emission, the total energy in electrons is $(2.3\pm 0.3)\times 10^{45}$ erg ($(7.2\pm 0.9)\times 10^{45}$ erg) for a distance of 6 kpc (10.6 kpc). This value is already higher by a factor of 10 than the energy contained in the magnetic field of 2×10^{44} erg as estimated by [Ng et al., 2008] for a magnetic field of $15\,\mu$G, confirming the notion of the PWN being particle-dominated. As so far only those electrons responsible for the observed VHE γ-ray emission have been considered the ratio of total electron to magnetic field energy is thus likely higher.

As proposed by de Jager [2008], the total energy in electrons can be compared with the total energy released by the pulsar since birth according to

$$W_{\mathrm{e,tot}} = \epsilon\, E_{\mathrm{rot,tot}}, \tag{5.2}$$

where ϵ denotes the conversion efficiency of spin-down power into electron energy, and $E_{\mathrm{rot,tot}}$ the total energy release according to Eq. 2.2. This expression contains several factors that are unknown or highly uncertain. $W_{\mathrm{e,tot}}$ has been derived for the H.E.S.S. energy range only and without detailed modeling, little is known about the underlying spectral energy distribution of electrons and an extrapolation to the full energy range of electrons is not possible. van der Swaluw and Wu [2001] used the relative size of the PWN and the SNR region as observed in the X-ray energy band to derive a birth period of the pulsar of $P_0 = 82\,\mathrm{ms}$. The released energy is then $E_{\mathrm{rot,tot}} = 2.8\times 10^{48}\,\mathrm{erg}$ and larger by three orders of magnitude than $W_{\mathrm{e,tot}}$. Thus, PSR J1846−0258 is energetically capable of powering the observed VHE emission.

The VHE particles are expected to leave the production site by diffusion, governed by

scattering of the particles off the ambient magnetic field. The size of the VHE-emitting region can be limited by the timescale set by the cooling time or age of the system and propagation speed of the particles. In case of a point-like particle injection from a central source such as the pulsar, the size of the source is given by

$$R_{\mathrm{PWN}} \sim (2\,D\,\tau)^{1/2}\,, \tag{5.3}$$

where D denotes the diffusion coefficient and τ the age of the particles. The slowest possible diffusion in an isotropic medium is Bohm diffusion and, assuming a uniform ambient medium and VHE γ-ray production via IC on CMB, the diffusion coefficient is $D = 10^{26}\,(E_{\mathrm{e}}/1\,\mathrm{TeV})\,(B/1\,\mu\mathrm{G})^{-1}\,\mathrm{cm}^2\,\mathrm{s}^{-1}$ [Hinton and Hofmann, 2009], where E_{e} is the energy of the emitting electrons in units of 1 TeV. The size of the VHE PWN is then

$$R = 0.02\,\left(\left(\frac{t}{1\,\mathrm{year}}\right)\,\left(\frac{E_{\mathrm{e}}}{1\,\mathrm{TeV}}\right)\,\left(\frac{B}{1\,\mu\mathrm{G}}\right)^{1/2}\right)\,\mathrm{pc}, \tag{5.4}$$

where t is the timescale in units of 1 year. In the case of Kes 75, the SR cooling timescale is larger than the age of the system of 800 years and the latter is used for the calculation of the size of the PWN. Taking a maximum electron energy of 80 TeV, corresponding to an IC photon energy of 20 TeV for IC on CMB in a magnetic field of $10\,\mu$G, the calculated physical radius of the VHE PWN is 1.6 pc, corresponding to a source width of 0.03° for an assumed distance of 6 kpc. Such a source appears point-like for observations with H.E.S.S., as expected, and is compatible with a compact VHE emission region for a young PWN. Please note that a larger magnetic field than $10\,\mu$G would result in a lower diffusion coefficient and consequently in more compact nebula sizes. However, for energy-dependent diffusion coefficients, due to e.g. non-uniform magnetic fields within the nebula, electrons may be able to escape faster from the production site and form a larger nebula.

SNR Origin

The γ-ray emission detected with H.E.S.S. in the direction of Kes 75 is unresolved and is within boundaries of the radio SNR shell. Given the small diameter of the shell and the H.E.S.S. angular resolution, the SNR shell cannot be excluded as a viable candidate source for the observed VHE γ-ray emission based on the VHE morphology. Possible scenarios for VHE emission from the SNR shell will be discussed based on the energetics.

In the hadronic scenario, protons are accelerated in the SN shock front to relativistic energies and, in inelastic scattering with the ambient interstellar matter upstream and downstream the shock, produce π^0-mesons. These mesons subsequently decay into γ-rays producing the observed VHE emission (see e.g. Reynolds [2008]). The VHE emission thereby traces the target material. The high density region in the southern direction of Kes 75 as found by Morton et al. [2007] could serve as high density target material. The $1 - 10$ TeV photons are then typically produced by $10 - 100$ TeV protons [Mori, 1997].

The energy content of the proton population responsible for the VHE flux is

$$W_{\mathrm{pp}}(10-100\,\mathrm{TeV}) = t_{\mathrm{pp}\rightarrow\pi_0} \times L_\gamma(1-10\,\mathrm{TeV}) \tag{5.5}$$

where $t_{\mathrm{pp}\rightarrow\pi_0}$ is the proton cooling time and L_γ is the VHE luminosity in the energy range of 1 TeV to 10 TeV. Substituting the proton cooling time in the $1-10\,\mathrm{TeV}$ energy band of $t_{\mathrm{pp}\rightarrow\pi_0} \sim 5\times10^{15}\,(\mathrm{n/cm^{-3}})^{-1}\mathrm{s}$ [Aharonian, 2004] and the $1-10\,\mathrm{TeV}$ VHE luminosity in Eq. 5.5, the total energy in protons is

$$W_{\mathrm{p}}(10-100\,\mathrm{TeV}) = 3\times10^{49}\left(\frac{n}{\mathrm{cm^{-3}}}\right)^{-1}\left(\frac{d}{6\,\mathrm{kpc}}\right)^2\,\mathrm{erg}. \tag{5.6}$$

The energy content of the protons depends on the density of the surrounding medium and the distance to the emitting region. For a distance of 6 kpc and a density of $1\,\mathrm{cm^{-3}}$, lower than the typical ISM density, the above estimate is small compared to the total kinetic energy of the SN explosion of $E_0 = 1.4\times10^{51}\,d_{6\,\mathrm{kpc}}^{9/2}\,\mathrm{erg}$ as estimated by Leahy and Tian [2008].

It should be noted, however, that the proton population responsible for the observed VHE flux represents only a fraction of the total proton population. The extrapolation to lower energies is highly sensitive on the assumed spectral index of the proton population and leads to large uncertainties of the derived total energy in protons. While it is expected that the proton spectrum follows a power law which has the same slope as the observed VHE γ-ray spectrum, i.e. a photon index of ~ 2.45 in the case of Kes 75, a typical index close to 2.0 is expected from diffusive shock acceleration theory. Therefore, different indices in the range from 2.0 (the theoretical value) to 2.6 (observed spectral slope with $1\,\sigma$-error) will be tested. Assuming that the proton population follows a power-law spectrum that continues to GeV energies (the rest mass of the proton is $\sim 1\,\mathrm{GeV}$) with a spectral index of $\Gamma = 2.4$, the total energy W_{tot} in protons can be written as

$$W_{\mathrm{p,tot}} = W_{\mathrm{p}}(10\,\mathrm{GeV}-100\,\mathrm{TeV}) \tag{5.7}$$

$$= \left(\frac{(0.001\,\mathrm{TeV})^{2-\Gamma}-(100\,\mathrm{TeV})^{2-\Gamma}}{(10\,\mathrm{TeV})^{2-\Gamma}-(100\,\mathrm{TeV})^{2-\Gamma}}\right)\times W_{\mathrm{p}}(10-100\,\mathrm{TeV}) \tag{5.8}$$

$$= 97\;\times\; W_{\mathrm{p}}(10-100\,\mathrm{TeV}) \tag{5.9}$$

$$= 3\times10^{51}\left(\frac{n}{\mathrm{cm^{-3}}}\right)^{-1}\left(\frac{d}{6\,\mathrm{kpc}}\right)^2\,\mathrm{erg}. \tag{5.10}$$

The total energy in protons for $\Gamma = 2.4$ exceeds the estimated SN explosion energy E_0 by a factor of 2 for a density of the ambient medium close to the ISM value of $3\,\mathrm{cm^{-3}}$. The conversion efficiency $\eta_{\mathrm{p}} = (W_{\mathrm{p,tot}})/(E_0)$ of converting the SN explosion energy (E_0) into accelerated protons with a total energy W_{tot} as calculated in Eq. 5.8 is shown in Fig. 5.9 for a distance of 6 kpc and in Fig. 5.10 for a distance of 10.6 kpc as a function of

the density of the ambient medium and for different indices. The conversion efficiency is unusually large for $\Gamma > 2.2$, unless the SNR is located at a large distance, or the VHE γ-ray emission is produced in very dense regions.

The density of the swept-up and shocked CSM/ISM can be estimated from X-ray measurements of the two southern hot-spots of the SNR. It should be noted that the available estimates cover a large range of densities as the estimates depend sensitively on the choice of the extraction region for the X-ray emitting gas as well as on the background subtraction region. In addition, the local density may vary within the SNR shell and deviate from the values derived from the two hot-spot regions. The densities found by Morton et al. [2007] are $65\,d_{6\,\mathrm{kpc}}^{-1/2}\,\mathrm{cm}^{-3}$ and $105\,d_{6\,\mathrm{kpc}}^{-1/2}\,\mathrm{cm}^{-3}$ for the SE and SW clump and are unusually large compared to the typical ISM density of $3\,\mathrm{cm}^{-3}$, but not unreasonable in the presence of molecular clouds in the vicinity of Kes 75. Lower densities of $7.1\,d_{6\,\mathrm{kpc}}^{-1/2}\,\mathrm{cm}^{-3}$ and $1.9\,d_{6\,\mathrm{kpc}}^{-1/2}\,\mathrm{cm}^{-3}$ as well as $7.4\,d_{6\,\mathrm{kpc}}^{-1/2}\,\mathrm{cm}^{-3}$ and $4.1\,d_{6\,\mathrm{kpc}}^{-1/2}\,\mathrm{cm}^{-3}$ for the SE and SW clump, respectively, have been estimated by Su et al. [2009] and Temim et al. [2012] using the same data but different signal and background extraction regions. The mean density from the two clumps from the measurement of Temim et al. [2012] is $5.7\,d_{6\,\mathrm{kpc}}^{-1/2}\,\mathrm{cm}^{-3}$. Substituting this density in Eq. 5.10, one derives an efficiency for converting the kinetic energy of the SN explosion into proton particle acceleration of $\eta_\mathrm{p} = 36\,d_{6\,\mathrm{kpc}}^{-2}\%$, which is in reasonable agreement with the theoretical expectation that a significant fraction of the SN explosion energy is released in relativistic protons. For a larger distance of 10.6 kpc, the conversion efficiency becomes even smaller, $\eta_\mathrm{p} = 11\%$. For a mean density of $85\,d_{6\,\mathrm{kpc}}^{-1/2}\,\mathrm{cm}^{-3}$ as estimated from Morton et al. [2007], the conversion efficiency is only $\eta_\mathrm{p} = 2\,d_{6\,\mathrm{kpc}}^{-2}\%$ and Kes 75 would be an inefficient VHE γ-ray source.

Despite the large uncertainties of the shape of the proton spectrum, it can be concluded that the SNR of Kes 75 is energetically capable of powering the VHE γ-ray source for certain combinations of distance and density.

To conclude, both the PWN and SNR of Kes 75 are viable candidates for generating the VHE γ-ray emission as seen from HESS J1846−029. With instruments that provide a higher angular resolution such as CTA, it might be possible to disentangle the contributions from each counterpart. Furthermore, with observations at lower energies with H.E.S.S. II it might be possible to measure any turnover of the VHE γ-ray spectrum, thus providing important input for the broad-band modeling of this source.

5.5.2 Pulsed Emission

The search for pulsed emission did not result in any detection for the total data set and the annual data sets covering the pre- and post-outburst phase of the pulsar. Given the lack of detection of any pulsed emission in the radio and HE waveband, detailed modeling of pulsed emission within the PC or OG/TPC scenario is uninformative.

It can be noted that any pulsed emission from within the pulsar's magnetosphere must come from higher altitudes above the neutron star surface as absorption processes such

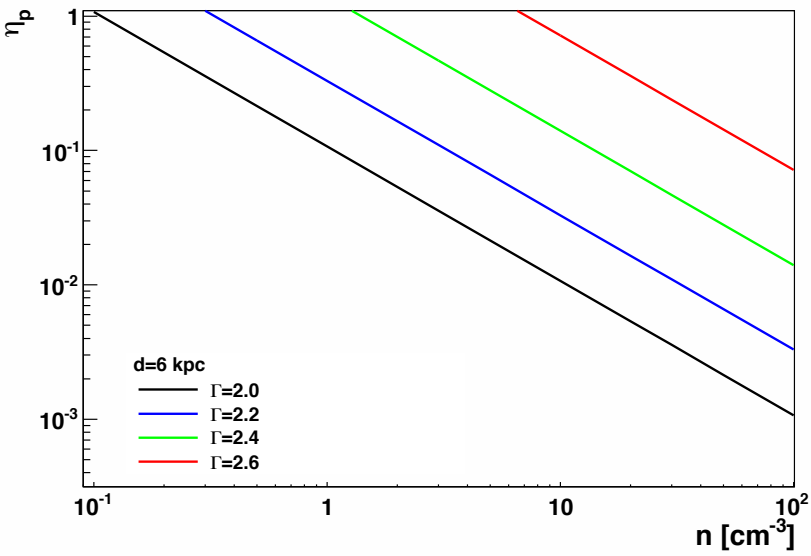

Figure 5.9 Efficiency for converting the kinetic explosion energy of the SN of $E_0 = 1.4 \times 10^{51}\, d^{9/2}_{6\,\mathrm{kpc}}$ erg into acceleration of protons in the energy range of > 1 GeV, assuming a distance of $d = 6$ kpc and for different indices of the proton spectrum.

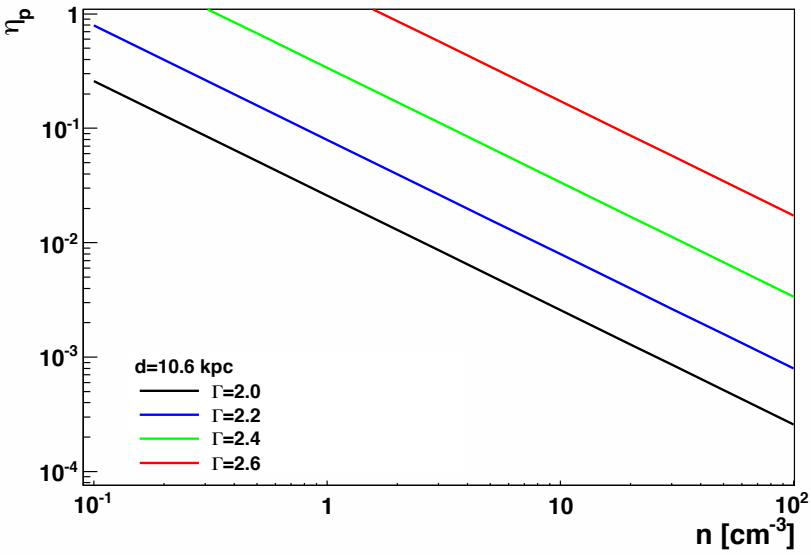

Figure 5.10 Efficiency for converting the kinetic explosion energy of the SN of $E_0 = 1.4 \times 10^{51}\, d^{9/2}_{6\,\mathrm{kpc}}$ erg into acceleration of protons in the energy range of > 1 GeV, assuming a distance of $d = 10.6$ kpc and for different indices of the proton spectrum.

as magnetic photon absorption hinders the passage of high energy photons through the strong inner magnetosphere of the pulsar, limiting the maximum reachable energies of the accelerated particles.

In addition, the geometry of PSR J1846−0258 may be unfavorable for detection of pulsed emission from within the pulsar's magnetosphere. While Livingstone et al. [2011] deduced a magnetic inclination angle of 10° using the model of an oblique rotator, the modeling of the torus of the PWN [Ng et al., 2008] implies an observer angle of $62° \pm 5°$. The resulting large impact angle suggests a low energy cutoff for any pulsed emission within the PC or OG/TPC scenario.

Pulsed VHE γ-ray emission up to 400 GeV has been seen so far from only one pulsar, the young and energetic Crab pulsar, by VERITAS [VERITAS Collaboration et al., 2011] and MAGIC [Aleksić et al., 2012].

Several scenarios have been proposed to explain the observed pulsed emission. In a synchrotron self-Compton (SSC) model as proposed by Lyutikov et al. [2012], the VHE γ-ray emission is produced in the outer magnetosphere by inverse Compton scattering (IC) of secondary and tertiary electron-positron pairs on magnetospheric UV and X-ray target photon fields. In this scenario, a photon spectrum in the form of a power law, extending from energies of a few tens of GeV up to TeV is expected. In the following, a possible VHE component from IC within the simplified SSC model by Lyutikov et al. [2012] for the Crab pulsar will be discussed for PSR J1846−0258.

The maximum energy of IC photons produced by the secondary electron pairs is given in Lyutikov et al. [2012] and reads

$$\epsilon_{\max} = (3\pi)^{1/4} \frac{m_{\mathrm{e}} c^{7/4}}{e^{1/4}} \eta^{1/4} \xi^{1/2} \lambda^{-1} \frac{B_{\mathrm{surf}}^{1/4} R_{\mathrm{NS}}^{3/4}}{P^{1/4}} = 150 \, (\eta_{-2}^{1/4} \xi^{1/2} \lambda_2^{-1}) \, \mathrm{GeV}. \tag{5.11}$$

where B_{surf} denotes the surface magnetic field strength, R_{NS} the neutron star radius, η the acceleration efficiency, ξ the radius of curvature of the magnetic field lines in units of the radius of the light cylinder R_{LC} and λ the multiplicity factor of secondary particles. An order-of-magnitude estimate of the maximum energy of IC photons for the Crab pulsar can be attained substituting the pulsar's surface magnetic field B_{surf} and period P as well as scaling the acceleration efficiency ($\eta_{-2} = 100\,\eta$) and multiplicity factor ($\lambda_2 = 0.01\,\lambda$) to typical values. It can be seen that the maximum energy of IC photons can reach well beyond 100 GeV.

The surface magnetic field B_{surf} and period P enter the calculations for the IC component. Additionally, the radius of curvature ξ in units of R_{LC} scales with P. The maximum energy finally scales as $B_{\mathrm{surf}}^{1/4} P^{1/2}$. The Crab pulsar's surface magnetic field of 4×10^{12} G and its period of 0.033 s are lower by a factor of ~ 10 from what is known for PSR J1846−0258 (4.86×10^{13} G, 324 ms). The resulting maximum energy of IC photons from the magnetosphere of PSR J1846−0258 is thus larger by a factor of ~ 6 and from the presented calculations it is possible that pulsed radiation produced in this model might attain energies within reach of observations with H.E.S.S..

The corresponding peak luminosity of the IC component from scattering off UV pho-

tons in the Klein-Nishina limit is

$$L_{\mathrm{IC}} = 4 \times 10^{35} \eta_{-1} \epsilon_{\mathrm{UV}}^{-2} \lambda_2 \,\mathrm{erg\,s^{-1}} \tag{5.12}$$

where $\eta_{-1} = 10\,\eta$ is the scaled acceleration efficiency, $\epsilon = (1\,\mathrm{eV})\,\epsilon_{\mathrm{UV}}$ the typical target photon energy and $\lambda_2 = 0.01\,\lambda$ the scaled multiplicity factor of secondary particles. The luminosity is independent of the magnetic field and/or period of the pulsar, but depends on the target photon field. It can be noted that two effects might hinder any observable pulsed emission within this scenario. Given a spin-down energy of PSR J1846−0258 that is at least one order of magnitude smaller than that of the Crab pulsar, the density of target photons fields from UV photons is expected to be correspondingly smaller. In addition, the multiplicity of secondary particles is expected to be greatly reduced for a pulsar of such high magnetic field as pointed out by Baring and Harding [2001]. Thus it might not be surprising that no pulsed emission from PSR J1846−0258 has been found.

A detailed modeling of the γ-ray emission from PSR J1846−0258 within the model used for the Crab pulsar [Aleksić et al., 2012] may provide further insights into the acceleration and radiation mechanisms at work in such high magnetic fields as found for Kes 75. Given the non-detection of pulsed emission at GeV energies by *Fermi*-LAT and at GeV-to-TeV energies as presented in this work, however, little constraints are provided for the large parameter space inherent in the most recent and highly sophisticated models.

6 Summary

In this work, the analysis and interpretation of a search for pulsed and steady VHE γ-ray emission from the direction of three pulsars, the two millisecond pulsars PSR J0437−4715 and PSR J1824−2452 as well as the pulsar PSR J1846−0258 in the composite SNR Kes 75, have been presented.

The analysis of H.E.S.S. observations conducted on the two MSPs PSR J0437−4715 and PSR J1824−2452 in 2004 and 2005, partially taken with a special trigger setup (the topological trigger with a convergent pointing) to lower the energy threshold of the instrument, and resulting in a live time of 22.2 hours and 6.3 hours, respectively, showed no hints of pulsed or steady VHE γ-ray emission. The search for a steady point-source like emission from PSR J0437−4715 and from PSR J1824−2452 resulted in a total significance $0.4\,\sigma$ and $-0.5\,\sigma$, respectively. A limiting VHE γ-ray luminosity of $2.65 \times 10^{30}\,\mathrm{erg\,s^{-1}}$ was found for PSR J0437−4715 in the $1 - 30\,\mathrm{TeV}$ energy band with a corresponding spin-down conversion efficiency smaller than 0.09%. The upper limit on the γ-ray luminosity in the same energy band for PSR J1824−2452 is $3.65 \times 10^{33}\,\mathrm{erg\,s^{-1}}$ with a spin-down conversion efficiency of less than 0.17 %.

Differential upper limits on the pulsed VHE γ-ray flux in the energy range from 100 GeV to 10 TeV have been compared to model predictions within polar cap models for PSR J0437−4715 and PSR J1824−2452, that where available at the time of this thesis. For PSR J0437−4715, the H.E.S.S. upper limits on the pulsed γ-ray flux cannot be used to constrain any model predictions for curvature radiation and have an energy threshold well above the cut-off energy of several GeV as measured by *Fermi*-LAT. For PSR J1824−2452, some polar cap models predict high-energy cutoffs exceeding 100 GeV when the geometry is favorable, i.e. for small impact angles when the line of sight crosses the narrow beam of radiation. To be consistent with the derived H.E.S.S. upper limits, the models require large impact angles where the observer angle is significantly different from the magnetic inclination angle. For both millisecond pulsars, the level of the inverse Compton emission as predicted within the available polar cap models is one to two orders of magnitude below the lowest H.E.S.S. upper limit at TeV energies. In order to resolve the open questions, updated model calculations, both within the outer gap and polar cap model, are needed. The H.E.S.S. upper limits can be used to give valuable input for the level of the predicted inverse Compton component.

In the second part of this thesis, the analysis and interpretation of H.E.S.S. observations of the composite SNR Kes 75, conducted between the years 2004 to 2008 and amounting to a total live time of 67.4 hours, have been presented. A clear signal at the significance level of $10\,\sigma$ of a point-like emission, positionally coincident at the $1\,\sigma$

level with the position of PSR J1846−0258 and the supernova remnant shell of Kes 75, was found. The energy spectrum of the emission is well described with a power law with a photon index of $\Gamma = 2.45 \pm 0.17_{\mathrm{stat}} \pm 0.2_{\mathrm{sys}}$ and the integral flux above 1 TeV is $F_\gamma = (4.0 \pm 0.8_{\mathrm{stat}} \pm 0.3_{\mathrm{sys}}) \times 10^{-13}\,\mathrm{erg\,cm^{-2}\,s^{-1}}$, corresponding to 1.8% of the flux of the Crab Nebula in the same energy band.

Two emission scenarios have been discussed. Both the pulsar wind nebula (PWN) and the supernova remnant (SNR) shell of Kes 75 are found to be viable candidates for powering the VHE γ-ray source. Assuming a PWN origin of the VHE γ-ray emission, the small extension of the VHE source can be explained with the very low age and large distance of PSR J1846−0258. Indeed, PSR J1846−0258 would be the youngest and one of the most distant pulsars to power a VHE PWN known to date. In a leptonic scenario, the VHE γ-ray emission stems from inverse Compton radiation of electrons up-scattering ambient photon fields. For different radiation fields, an estimate of the magnetic field in the range of $10 - 15\,\mu$G, well below the equipartition value of $B_{\mathrm{eq}} = 40\,\mu$G, is derived. The total energy in electrons responsible for the VHE γ-ray emission is estimated and larger by a factor of 10 than the magnetic field energy. The PWN of Kes 75 is thus particle-dominated. Some discrepancies of VHE and X-ray emission of the PWN have been found in context of studies correlating the VHE and X-ray emission of PWNe with pulsar properties such as its spin-down power and age. Although PSR J1846−0258 is a very powerful pulsar, it is with a γ-ray conversion efficiency in the energy band of 1 TeV to 10 TeV of $\eta_\gamma = (0.11 \pm 0.02_{\mathrm{stat}})\,\%$ ($\eta_\gamma = (0.35 \pm 0.05_{\mathrm{stat}})\,\%$) for an assumed distance of 6 kpc (10.6 kpc) an inefficient VHE γ-ray emitter. The ratio of VHE-to-X-ray luminosity of the PWN is 1/11. According to the correlation study relating the VHE and X-ray emission of PWNe with its spin-down power, PSR J1846−0258 should be less luminous in the X-ray band and/or more luminous in the VHE energy band than observed.

In an hadronic scenario, the VHE γ-ray emission is generated in interaction of protons with ambient interstellar material. The total energy in protons is estimated from the observed γ-ray flux for various spectral indices of the proton spectrum. Assuming the proton spectrum follows a power law with an index of 2.0, only a small fraction of the supernova explosion energy is converted into the total energy in protons. If, however, the proton spectrum follows a power law with a similar shape as that of the observed γ-ray spectrum, a dense medium and/or a large distance are required for an acceptable conversion efficiency of SN explosion energy into proton particle acceleration. Such large densities have been measured for Kes 75 and are not unreasonable in the presence of molecular clouds in the vicinity of Kes 75.

No hint for pulsed emission from the pulsar PSR J1846−0258 has been found and several aspects such as its high magnetic field, its low spin-down energy compared to the Crab pulsar and its unfavorable viewing geometry are presented to explain the lack of detection.

Future Cherenkov telescope experiments with a lower energy threshold and a higher sensitivity such as H.E.S.S. II or CTA will give more insight into the physics of pulsars. In addition, the higher resolution of CTA will help to resolve the VHE γ-ray emission

of composite SNRs such as Kes 75 and thus to understand the nature of the source of the VHE emission.

Bibliography

A. A. Abdo, M. Ackermann, M. Ajello, et al. A Population of Gamma-Ray Millisecond Pulsars Seen with the Fermi Large Area Telescope. *Science*, 325:848, Aug. 2009.

A. A. Abdo, M. Ackermann, M. Ajello, et al. A population of gamma-ray emitting globular clusters seen with the Fermi Large Area Telescope. *A&A*, 524:A75, Dec. 2010a.

A. A. Abdo, M. Ackermann, M. Ajello, et al. Detection of the Energetic Pulsar PSR B1509-58 and its Pulsar Wind Nebula in MSH 15-52 Using the Fermi-Large Area Telescope. *ApJ*, 714:927–936, May 2010b.

A. A. Abdo, M. Ackermann, M. Ajello, et al. Discovery of Pulsed γ-Rays from PSR J0034−0534 with the Fermi Large Area Telescope: A Case for Co-Located Radio and γ-Ray Emission Regions. *ApJ*, 712:957–963, Apr. 2010c.

A. A. Abdo, M. Ackermann, M. Ajello, et al. The First Fermi Large Area Telescope Catalog of Gamma-ray Pulsars. *ApJS*, 187:460–494, Apr. 2010d.

M. Ackermann, M. Ajello, L. Baldini, et al. Fermi-LAT Search for Pulsar Wind Nebulae Around Gamma-ray Pulsars. *ApJ*, 726:35, Jan. 2011.

F. Aharonian, A. Akhperjanian, M. Beilicke, et al. The Crab Nebula and Pulsar between 500 GeV and 80 TeV: Observations with the HEGRA Stereoscopic Air Cerenkov Telescopes. *ApJ*, 614:897–913, Oct. 2004a.

F. Aharonian, A. G. Akhperjanian, K.-M. Aye, et al. Calibration of cameras of the H.E.S.S. detector. *Astroparticle Physics*, 22:109–125, Nov. 2004b.

F. Aharonian, A. G. Akhperjanian, K.-M. Aye, et al. Very high energy gamma rays from the composite SNR G 0.9+0.1. *A&A*, 432:L25–L29, Mar. 2005.

F. Aharonian, A. G. Akhperjanian, A. R. Bazer-Bachi, et al. Energy dependent γ-ray morphology in the pulsar wind nebula HESS J1825-137. *A&A*, 460:365–374, Dec. 2006a.

F. Aharonian, A. G. Akhperjanian, A. R. Bazer-Bachi, et al. First detection of a VHE gamma-ray spectral maximum from a cosmic source: HESS discovery of the Vela X nebula. *A&A*, 448:L43–L47, Mar. 2006b.

F. Aharonian, A. G. Akhperjanian, A. R. Bazer-Bachi, et al. The H.E.S.S. Survey of the Inner Galaxy in Very High Energy Gamma Rays. *ApJ*, 636:777–797, Jan. 2006c.

F. Aharonian, A. G. Akhperjanian, A. R. Bazer-Bachi, et al. Observations of the Crab nebula with HESS. *A&A*, 457:899–915, Oct. 2006d.

F. Aharonian, A. G. Akhperjanian, A. R. Bazer-Bachi, et al. Search for pulsed VHE gamma-ray emission from young pulsars with HESS. *A&A*, 466:543–554, May 2007.

F. A. Aharonian. *Very high energy cosmic gamma radiation : a crucial window on the extreme Universe*. World Scientific Publishing, 2004.

F. A. Aharonian, A. M. Atoyan, and T. Kifune. Inverse Compton gamma radiation of faint synchrotron X-ray nebulae around pulsars. *MNRAS*, 291:162–176, Oct. 1997.

J. Aleksić, E. A. Alvarez, L. A. Antonelli, et al. Phase-resolved energy spectra of the Crab pulsar in the range of 50-400 GeV measured with the MAGIC telescopes. *A&A*, 540:A69, Apr. 2012.

E. Aliu, H. Anderhub, L. A. Antonelli, et al. Observation of Pulsed γ-Rays Above 25 GeV from the Crab Pulsar with MAGIC. *Science*, 322:1221, Nov. 2008.

M. A. Alpar, A. F. Cheng, M. A. Ruderman, and J. Shaham. A new class of radio pulsars. *Nature*, 300:728–730, Dec. 1982.

A. M. Archibald, V. M. Kaspi, M. A. Livingstone, and M. A. McLaughlin. No Detectable Radio Emission from the Magnetar-Like Pulsar in Kes 75. *ApJ*, 688:550–554, Nov. 2008.

A. M. Archibald, I. H. Stairs, S. M. Ransom, et al. A Radio Pulsar/X-ray Binary Link. *Science*, 324:1411, June 2009.

J. Arons. Pair creation above pulsar polar caps - Geometrical structure and energetics of slot gaps. *ApJ*, 266:215–241, Mar. 1983.

J. Arons. Theory of pulsar winds. In *34th COSPAR Scientific Assembly*, volume 34 of *COSPAR Meeting*, 2002.

J. Arons and E. T. Scharlemann. Pair formation above pulsar polar caps - Structure of the low altitude acceleration zone. *ApJ*, 231:854–879, Aug. 1979.

W. B. Atwood, M. Ziegler, R. P. Johnson, and B. M. Baughman. A Time-differencing Technique for Detecting Radio-quiet Gamma-Ray Pulsars. *ApJL*, 652:L49–L52, Nov. 2006.

W. B. Atwood, A. A. Abdo, M. Ackermann, et al. The Large Area Telescope on the Fermi Gamma-Ray Space Telescope Mission. *ApJ*, 697:1071–1102, June 2009.

W. Baade and F. Zwicky. Cosmic Rays from Super-novae. *Proceedings of the National Academy of Science*, 20:259–263, May 1934.

D. C. Backer and S. T. Sallmen. Polarimetry, Peculiar Mode and X-Ray Alignment of PSR B1821-24. *Astron. J.*, 114:1539, Oct. 1997.

M. G. Baring and A. K. Harding. Photon Splitting and Pair Creation in Highly Magnetized Pulsars. *ApJ*, 547:929–948, Feb. 2001.

R. H. Becker and D. J. Helfand. New radio observations of the composite supernova remnant G29.7-0.3. *ApJ*, 283:154–157, Aug. 1984.

W. Becker and C. Y. Hui. A search for X-ray counterparts of the millisecond pulsars in the globular cluster M28 (NGC 6626). *ArXiv Astrophysics e-prints, arXiv:astro-ph/0705.0119*, May 2007.

W. Becker and J. Trümper. Detection of Pulsed X-Rays from the Binary Millisecond Pulsar J:0437-4715. *Nature*, 365:528, Oct. 1993.

W. Becker, D. A. Swartz, G. G. Pavlov, et al. Chandra X-Ray Observatory Observations of the Globular Cluster M28 and Its Millisecond Pulsar PSR B1821-24. *ApJ*, 594:798–811, Sept. 2003.

W. Becker, H. H. Huang, and T. Prinz. X-ray Counterparts of Millisecond Pulsars in Globular Clusters. *ArXiv Astrophysics e-prints, arXiv:astro-ph/1006.0335*, June 2010.

W. Bednarek and M. Bartosik. Gamma-rays from the pulsar wind nebulae. *A&A*, 405: 689–702, July 2003.

J. F. Bell, M. Bailes, and M. S. Bessell. Optical detection of the companion of the millisecond pulsar J0437 - 4715. *Nature*, 364:603–605, Aug. 1993.

J. F. Bell, M. Bailes, R. N. Manchester, J. M. Weisberg, and A. G. Lyne. The proper motion and wind nebula of the nearby millisecond pulsar J0437-4715. *ApJL*, 440: L81–L83, Feb. 1995.

D. Berge, S. Funk, and J. Hinton. Background modelling in very-high-energy γ-ray astronomy. *A&A*, 466:1219–1229, May 2007.

K. Bernlöhr, O. Carrol, R. Cornils, et al. The optical system of the H.E.S.S. imaging atmospheric Cherenkov telescopes. Part I: layout and components of the system. *Astropart. Phys.*, 20:111–128, Nov. 2003.

D. Bhattacharya and E. P. J. van den Heuvel. Formation and evolution of binary and millisecond radio pulsars. *Phys. Rep.*, 203:1–124, 1991.

R. Blandford and S. A. Teukolsky. Arrival-time analysis for a pulsar in a binary system. *ApJ*, 205:580–591, Apr. 1976.

G. R. Blumenthal and R. J. Gould. Bremsstrahlung, Synchrotron Radiation, and Compton Scattering of High-Energy Electrons Traversing Dilute Gases. *Reviews of Modern Physics*, 42:237–271, 1970.

D. C.-J. Bock and B. M. Gaensler. Measurement of Spectral Breaks in Pulsar Wind Nebulae with Millimeter-Wave Interferometry. *ApJ*, 626:343–349, June 2005.

S. Bogdanov, M. van den Berg, M. Servillat, et al. Chandra X-ray Observations of 12 Millisecond Pulsars in the Globular Cluster M28. *ApJ*, 730:81, Apr. 2011.

O. Bolz. Absolute Energiekalibration der abbildenden Cherenkov-Teleskope des H.E.S.S. Experiments und Ergebnisse erster Beobachtungen des Supernovaueberrests RX J1713.7-3946. *Ph.D. Thesis, MPI fuer Kernphysik, Heidelberg*, 2004.

K. T. S. Brazier. Confidence Intervals from the Rayleigh Test. *MNRAS*, 268:709, June 1994.

R. Buccheri, K. Bennett, G. F. Bignami, et al. Search for pulsed gamma-ray emission from radio pulsars in the COS-B data. *A&A*, 128:245–251, Nov. 1983.

N. Bucciantini, E. Amato, and L. Del Zanna. Relativistic MHD simulations of pulsar bow-shock nebulae. *A&A*, 434:189–199, Apr. 2005.

N. Bucciantini, J. Arons, and E. Amato. Modelling spectral evolution of pulsar wind nebulae inside supernova remnants. *MNRAS*, 410:381–398, Jan. 2011.

T. Bulik, B. Rudak, and J. Dyks. Spectral features in gamma-rays expected from millisecond pulsars. *MNRAS*, 317:97–104, Sept. 2000.

S. Carrigan. Pulsar Wind Nebulae with H.E.S.S.: Establishing a Connection between high-power Pulsars and very-high-energy gamma-ray Sources. *Ph.D. Thesis, MPI fuer Kernphysik, Heidelberg*, 2007.

S. Carrigan, J. A. Hinton, W. Hofmann, et al. Establishing a connection between high-power pulsars and very-high-energy gamma-ray sources. In *International Cosmic Ray Conference*, volume 2 of *International Cosmic Ray Conference*, pages 659–662, 2008.

J. L. Caswell, J. D. Murray, R. S. Roger, et al. Neutral hydrogen absorption measurements yielding kinematic distances for 42 continuum sources in the galactic plane. *A&A*, 45:239–258, Dec. 1975.

P. M. Chadwick, K. Lyons, T. J. L. McComb, et al. Very High Energy Gamma Rays from Young Pulsars and Supernova Remnants in the Southern Hemisphere. *ApJ*, 537: 414–421, July 2000.

K. S. Cheng, C. Ho, and M. Ruderman. Energetic radiation from rapidly spinning pulsars. I - Outer magnetosphere gaps. II - VELA and Crab. *ApJ*, 300:500–539, Jan. 1986.

K. S. Cheng, R. E. Taam, and W. Wang. Pulsar Wind Nebulae and the Nonthermal X-Ray Emission of Millisecond Pulsars. *ApJ*, 641:427–437, Apr. 2006.

R. A. Chevalier. Young Core-Collapse Supernova Remnants and Their Supernovae. *ApJ*, 619:839–855, Feb. 2005.

R. Cornils, S. Gillessen, I. Jung, et al. The optical system of the H.E.S.S. imaging atmospheric Cherenkov telescopes. Part II: mirror alignment and point spread function. *Astropart. Phys.*, 20:129–143, Nov. 2003.

J. W. Cronin, K. G. Gibbs, and T. C. Weekes. The search for discrete astrophysical sources of energetic gamma radiation. *Annual Review of Nuclear and Particle Science*, 43:883–926, 1993.

T. Damour and N. Deruelle. General relativistic celestial mechanics of binary systems - II. The post-Newtonian timing formula. *Ann. Inst. Henri Poincaré Phys. Théor.*, 44: 263–292, 1986.

I. J. Danziger, D. Baade, and M. della Valle. Optical Spectroscopy and Photometry of the Companion of the Bright Millisecond Pulsar J:0437-4715. *A&A*, 276:382, Sept. 1993.

J. K. Daugherty and A. K. Harding. Gamma-Ray Pulsars: Emission from Extended Polar CAP Cascades. *ApJ*, 458:278, Feb. 1996.

J. M. Davies and E. S. Cotton. Design of the quartermaster solar furnace. *Solar Energy*, 1(2-3):16–22, 1957.

O. C. de Jager. On periodicity tests and flux limit calculations for gamma-ray pulsars. *ApJ*, 436:239–248, Nov. 1994.

O. C. de Jager. Estimating the Birth Period of Pulsars through GLAST LAT Observations of Their Wind Nebulae. *ApJL*, 678:L113–L116, May 2008.

O. C. de Jager and I. Büsching. The H-test probability distribution revisited: improved sensitivity. *A&A*, 517:L9, July 2010.

O. C. de Jager and A. Djannati-Ataï. Implications of H.E.S.S. Observations of Pulsar Wind Nebulae. In W. Becker, editor, *Astrophysics and Space Science Library*, volume 357 of *Astrophysics and Space Science Library*, page 451, 2009.

O. C. de Jager and C. Venter. Ground-based Gamma-Ray Observations of Pulsars and their Nebulae: Towards a New Order. In *International Cosmic Ray Conference*, volume 2 of *International Cosmic Ray Conference*, pages 707–710, Mar. 2008.

O. C. de Jager, B. C. Raubenheimer, and J. W. H. Swanepoel. A powerful test for weak periodic signals with unknown light curve shape in sparse data. *A&A*, 221:180–190, Aug. 1989.

O. C. de Jager, S. E. S. Ferreira, A. Djannati-Ataï, M. Dalton, C. Deil, K. Kosack, M. Renaud, U. Schwanke, and O. Tibolla. Unidentified Gamma-Ray Sources as Ancient Pulsar Wind Nebulae. *ArXiv Astrophysics e-prints, arXiv:astro-ph/0906.2644*, June 2009.

R. De los Reyes, W. Bednarek, M. Camara, M. Lopez, and for the MAGIC collaboration. Upper limits for pulsars with MAGIC (2005/2006 observations). *ArXiv Astrophysics e-prints, arXiv:astro-ph/0907.1168*, July 2009.

M. de Naurois and H.E.S.S. Collaboration. The Galactic Sky seen by H.E.S.S. *Adv. Space Res.*, 51:258–267, Jan. 2013.

M. de Naurois, J. Holder, R. Bazer-Bachi, et al. Measurement of the Crab Flux above 60 GeV with the CELESTE Cerenkov Telescope. *ApJ*, 566:343–357, Feb. 2002.

A. T. Deller, J. P. W. Verbiest, S. J. Tingay, and M. Bailes. Extremely High Precision VLBI Astrometry of PSR J0437-4715 and Implications for Theories of Gravity. *ApJL*, 685:L67–L70, Sept. 2008.

A. J. Deutsch. The electromagnetic field of an idealized star in rigid rotation in vacuo. *Annales d'Astrophysique*, 18:1, Jan. 1955.

A. Djannati-Ataï, O. C. de Jager, R. Terrier, et al. New Companions for the lonely Crab? VHE emission from young pulsar wind nebulae revealed by H.E.S.S. In *International Cosmic Ray Conference*, volume 2 of *International Cosmic Ray Conference*, pages 823–826, 2008.

M. Doro and CTA Consortium. CTA − A project for a new generation of Cherenkov telescopes. *Nuclear Instruments and Methods in Physics Research A*, 630:285–290, Feb. 2011.

R. C. Duncan and C. Thompson. Formation of very strongly magnetized neutron stars - Implications for gamma-ray bursts. *ApJL*, 392:L9–L13, June 1992.

J. Dyks and B. Rudak. Two-Pole Caustic Model for High-Energy Light Curves of Pulsars. *ApJ*, 598:1201–1206, Dec. 2003.

J. Edelstein, R. S. Foster, and S. Bowyer. Extreme Ultraviolet Emission from the Millisecond Pulsar J0437-4715. *ApJ*, 454:442, Nov. 1995.

R. T. Edwards, G. B. Hobbs, and R. N. Manchester. TEMPO2, a new pulsar timing package - II. The timing model and precision estimates. *MNRAS*, 372:1549–1574, Nov. 2006.

L. Fairhead and P. Bretagnon. An analytical formula for the time transformation TB-TT. *A&A*, 229:240–247, Mar. 1990.

G. J. Feldman and R. D. Cousins. Unified approach to the classical statistical analysis of small signals. *Phys. Rev. D*, 57:3873–3889, Apr. 1998.

J. M. Fierro, Z. Arzoumanian, M. Bailes, et al. EGRET High-Energy gamma -Ray Pulsar Studies. II. Individual Millisecond Pulsars. *ApJ*, 447:807, July 1995.

M. Frąckowiak and B. Rudak. Modeling gamma radiation from millisecond pulsars. *Adv. Space Res.*, 35:1152–1157, 2005a.

M. Frąckowiak and B. Rudak. Numerical high energy radiation modeling of selected millisecond pulsars. *Memorie della Societa Astronomica Italiana*, 76:523, 2005b.

P. C. C. Freire. Pulsars in Globular Clusters. *http://www.naic.edu/~pfreire/GCpsr.html*, 2011.

P. C. C. Freire, A. A. Abdo, M. Ajello, et al. Fermi Detection of a Luminous γ-Ray Pulsar in a Globular Cluster. *Science*, 334:1107, Nov. 2011.

M. Fuessling. Convergent observation mode with a topological trigger for H.E.S.S.. *Diploma Thesis, Humboldt-Universität zu Berlin, Berlin*, 2006.

S. Funk, G. Hermann, J. Hinton, et al. The trigger system of the H.E.S.S. telescope array. *Astropart. Phys.*, 22:285–296, Nov. 2004.

B. M. Gaensler. Bow shocks around pulsars and neutron stars. *Adv. Space Res.*, 35: 1116–1122, 2005.

B. M. Gaensler and P. O. Slane. The Evolution and Structure of Pulsar Wind Nebulae. *ARA&A*, 44:17–47, Sept. 2006.

F. P. Gavriil, M. E. Gonzalez, E. V. Gotthelf, V. M. Kaspi, M. A. Livingstone, and P. M. Woods. Magnetar-Like Emission from the Young Pulsar in Kes 75. *Science*, 319:1802, Mar. 2008.

V. L. Ginzburg. *Theoretical physics and astrophysics*. Pergamon Press, 1979.

T. Gold. Rotating Neutron Stars as the Origin of the Pulsating Radio Sources. *Nature*, 218:731–732, 1968.

P. Goldreich and W. H. Julian. Pulsar Electrodynamics. *ApJ*, 157:869, Aug. 1969.

E. V. Gotthelf, G. Vasisht, M. Boylan-Kolchin, and K. Torii. A 700 Year-old Pulsar in the Supernova Remnant Kesteven 75. *ApJL*, 542:L37–L40, Oct. 2000.

B. M. S. Hansen and E. S. Phinney. The pulsar kick velocity distribution. *MNRAS*, 291:569, Nov. 1997.

A. K. Harding. Pulsar High-Energy Emission From the Polar Cap and Slot Gap. *ArXiv Astrophysics e-prints, arXiv:astro-ph/0710.3517*, 710, Oct. 2007.

A. K. Harding and A. G. Muslimov. Particle Acceleration Zones above Pulsar Polar Caps: Electron and Positron Pair Formation Fronts. *ApJ*, 508:328–346, Nov. 1998.

A. K. Harding, E. Tademaru, and L. W. Esposito. A curvature-radiation-pair-production model for gamma-ray pulsars. *ApJ*, 225:226–236, Oct. 1978.

A. K. Harding, V. V. Usov, and A. G. Muslimov. High-Energy Emission from Millisecond Pulsars. *ApJ*, 622:531–543, Mar. 2005.

W. E. Harris. A Catalog of Parameters for Globular Clusters in the Milky Way. *Astron. J.*, 112:1487, Oct. 1996.

J. D. Hart. On the choice of a truncation point in fourier series density estimation. *Journal of Statistical Computation and Simulation*, 21(2):95–116, 1985.

D. J. Helfand, B. F. Collins, and E. V. Gotthelf. Chandra X-Ray Imaging Spectroscopy of the Young Supernova Remnant Kesteven 75. *ApJ*, 582:783–792, Jan. 2003.

J. W. T. Hessels, S. M. Ransom, I. H. Stairs, P. C. C. Freire, V. M. Kaspi, and F. Camilo. A Radio Pulsar Spinning at 716 Hz. *Science*, 311:1901–1904, Mar. 2006.

J. W. T. Hessels, D. J. Nice, B. M. Gaensler, et al. PSR J1856+0245: Arecibo Discovery of a Young, Energetic Pulsar Coincident with the TeV γ-Ray Source HESS J1857+026. *ApJL*, 682:L41–L44, July 2008.

A. Hewish, S. J. Bell, J. D. H. Pilkington, P. F. Scott, and R. A. Collins. Observation of a Rapidly Pulsating Radio Source. *Nature*, 217:709–713, Feb. 1968.

A. M. Hillas. Cerenkov light images of EAS produced by primary gamma. In F. C. Jones, editor, *International Cosmic Ray Conference*, volume 3 of *International Cosmic Ray Conference*, pages 445–448, Aug. 1985.

J. A. Hinton and W. Hofmann. Teraelectronvolt Astronomy. *ARA&A*, 47:523–565, Sept. 2009.

K. Hirotani. High Energy Emission from Rotation-Powered Pulsars: Outer-gap vs. Slot-gap Models. *ArXiv Astrophysics e-prints, arXiv:astro-ph/0809.1283*, Sept. 2008.

K. Hirotani and S. Shibata. One-dimensional electric field structure of an outer gap accelerator - I. gamma-ray production resulting from curvature radiation. *MNRAS*, 308:54–66, Sept. 1999.

G. Hobbs, A. Faulkner, I. H. Stairs, et al. The Parkes multibeam pulsar survey - IV. Discovery of 180 pulsars and parameters for 281 previously known pulsars. *MNRAS*, 352:1439–1472, Aug. 2004.

S. Hoppe. Emitters of VHE γ-radiation as revealed by the H.E.S.S. Galactic plane survey. *Ph.D. Thesis, MPI fuer Kernphysik, Heidelberg*, 2008.

D. Horan and S. Wakely. TeV Source Catalogue (TeVCat). *http://tevcat.uchicago.edu*, 2012.

D. Horns, F. Aharonian, A. Santangelo, A. I. D. Hoffmann, and C. Masterson. Nucleonic gamma-ray production in Vela X. *A&A*, 451:L51–L54, June 2006.

IERS. IERS. *http://www.iers.org*, 2012.

S. Johnston, D. R. Lorimer, P. A. Harrison, et al. Discovery of a very bright, nearby binary millisecond pulsar. *Nature*, 361:613–615, Feb. 1993.

JPL Solar System Dynamics Group. JPL Solar System Dynamics. *http://ssd.jpl.nasa.gov*, 2012.

O. Kargaltsev and G. G. Pavlov. Pulsar Wind Nebulae in the Chandra Era. In C. Bassa, Z. Wang, A. Cumming, & V. M. Kaspi, editor, *40 Years of Pulsars: Millisecond Pulsars, Magnetars and More*, volume 983 of *American Institute of Physics Conference Series*, pages 171–185, Feb. 2008.

O. Kargaltsev and G. G. Pavlov. Pulsar-wind nebulae in X-rays and TeV γ-rays. In A. Comastri, L. Angelini, & M. Cappi, editor, *American Institute of Physics Conference Series*, volume 1248 of *American Institute of Physics Conference Series*, pages 25–28, July 2010.

C. F. Kennel and F. V. Coroniti. Confinement of the Crab pulsar's wind by its supernova remnant. *ApJ*, 283:694–709, Aug. 1984.

M. J. L. Kesteven. A catalogue of galactic radio sources. *Australian Journal of Physics*, 21:369, June 1968.

M. Kramer, C. Lange, D. R. Lorimer, D. C. Backer, K. M. Xilouris, A. Jessner, and R. Wielebinski. The Characteristics of Millisecond Pulsar Emission. III. From Low to High Frequencies. *ApJ*, 526:957–975, Dec. 1999.

L. Kuiper and W. Hermsen. High-energy characteristics of the schizophrenic pulsar PSR J1846-0258 in Kes 75. Multi-year RXTE and INTEGRAL observations crossing the magnetar-like outburst. *A&A*, 501:1031–1046, July 2009.

L. Kuiper, W. Hermsen, F. Verbunt, D. J. Thompson, I. H. Stairs, A. G. Lyne, M. S. Strickman, and G. Cusumano. The likely detection of pulsed high-energy gamma-ray emission from millisecond pulsar PSR J0218+4232. *A&A*, 359:615–626, July 2000.

H. S. Kumar and S. Safi-Harb. Variability of the High Magnetic Field X-Ray Pulsar PSR J1846-0258 Associated with the Supernova Remnant Kes 75 as Revealed by the Chandra X-Ray Observatory. *ApJL*, 678:L43–L46, May 2008.

H. Lampeitl, W. Hofmann, and HEGRA Collaboration. "Convergent observations" with stereoscopic HEGRA CT system. In B. L. Dingus, M. H. Salamon, & D. B. Kieda, editor, *American Institute of Physics Conference Series*, volume 515 of *American Institute of Physics Conference Series*, pages 328–332, June 2000.

M. I. Large, A. E. Vaughan, and B. Y. Mills. A Pulsar Supernova Association? *Nature*, 220:340–341, Oct. 1968.

J. M. Lattimer and M. Prakash. The Physics of Neutron Stars. *Science*, 304:536–542, Apr. 2004.

D. A. Leahy and W. W. Tian. The distance of the SNR Kes 75 and PWN PSR J1846-0258 system. *A&A*, 480:L25–L28, Mar. 2008.

R. W. Lessard, I. H. Bond, S. M. Bradbury, et al. Search for Pulsed TEV Gamma-Ray Emission from the Crab Pulsar. *ApJ*, 531:942–948, Mar. 2000.

T.-P. Li and Y.-Q. Ma. Analysis methods for results in gamma-ray astronomy. *ApJ*, 272:317–324, Sept. 1983.

M. A. Livingstone, V. M. Kaspi, E. V. Gotthelf, and L. Kuiper. A Braking Index for the Young, High Magnetic Field, Rotation-Powered Pulsar in Kesteven 75. *ApJ*, 647: 1286–1292, Aug. 2006.

M. A. Livingstone, V. M. Kaspi, F. P. Gavriil, et al. New phase-coherent measurements of pulsar braking indices. *Astrophys. Space Sci.*, 308:317–323, Apr. 2007.

M. A. Livingstone, V. M. Kaspi, and F. P. Gavriil. Timing Behavior of the Magnetically Active Rotation-Powered Pulsar in the Supernova Remnant Kesteven 75. *ApJ*, 710: 1710–1717, Feb. 2010.

M. A. Livingstone, C.-Y. Ng, V. M. Kaspi, F. P. Gavriil, and E. V. Gotthelf. Post-outburst Observations of the Magnetically Active Pulsar J1846-0258. A New Braking Index, Increased Timing Noise, and Radiative Recovery. *ApJ*, 730:66, Apr. 2011.

D. R. Lorimer. Binary and Millisecond Pulsars. *Living Reviews in Relativity*, 11:8, Nov. 2008.

F. Lucarelli, A. Konopelko, F. Aharonian, W. Hofmann, A. Kohnle, H. Lampeitl, and V. Fonseca. Observations of the Crab Nebula with the HEGRA system of IACTs in convergent mode using a topological trigger. *Astroparticle Physics*, 19:339–350, June 2003.

A. G. Lyne, A. Brinklow, J. Middleditch, S. R. Kulkarni, and D. C. Backer. The discovery of a millisecond pulsar in the globular cluster M28. *Nature*, 328:399–401, July 1987.

M. Lyutikov, N. Otte, and A. McCann. The Very High Energy Emission from Pulsars: A Case for Inverse Compton Scattering. *ApJ*, 754:33, July 2012.

R. N. Manchester. Private communication, 2005.

R. N. Manchester and S. Johnston. Polarization properties of two pulsars. *ApJL*, 441: L65–L68, Mar. 1995.

R. N. Manchester, G. B. Hobbs, A. Teoh, and M. Hobbs. The Australia Telescope National Facility Pulsar Catalogue. *Astron. J.*, 129:1993–2006, Apr. 2005.

F. Mattana, M. Falanga, D. Götz, et al. The Evolution of the γ- and X-Ray Luminosities of Pulsar Wind Nebulae. *ApJ*, 694:12–17, Mar. 2009.

M. Mayer, J. Brucker, I. Jung, K. Valerius, and C. Stegmann. Implications on the X-ray emission of evolved pulsar wind nebulae based on VHE gamma-ray observations. *ArXiv Astrophysics e-prints, arXiv:astro-ph/1202.1455*, Feb. 2012.

V. A. McBride, A. J. Dean, A. Bazzano, et al. INTEGRAL detection of the pulsar wind nebula in PSR J1846-0258. *A&A*, 477:249–253, Jan. 2008.

Meinberg Funkuhren GmbH and Co. KG. GPS167 Meinberg GPS receiver. *http://www.meinberg.de/german/products/gps167.htm*, 2012.

T. Mineo, G. Cusumano, E. Massaro, W. Becker, and L. Nicastro. Spectral and timing properties of the X-ray emission from the millisecond pulsar PSR B1821-24. *A&A*, 423:1045–1050, Sept. 2004.

M. Mori. The Galactic Diffuse Gamma-Ray Spectrum from Cosmic-Ray Proton Interactions. *ApJ*, 478:225, Mar. 1997.

T. D. Morton, P. Slane, K. J. Borkowski, S. P. Reynolds, D. J. Helfand, B. M. Gaensler, and J. P. Hughes. Observations of X-Rays and Thermal Dust Emission from the Supernova Remnant Kes 75. *ApJ*, 667:219–225, Sept. 2007.

A. G. Muslimov and A. K. Harding. Extended Acceleration in Slot Gaps and Pulsar High-Energy Emission. *ApJ*, 588:430–440, May 2003.

A. G. Muslimov and A. I. Tsygan. General relativistic electric potential drops above pulsar polar caps. *MNRAS*, 255:61–70, Mar. 1992.

C.-Y. Ng and V. M. Kaspi. High Magnetic Field Rotation-powered Pulsars. In E. Göğüş, T. Belloni, and Ü. Ertan, editors, *American Institute of Physics Conference Series*, volume 1379 of *American Institute of Physics Conference Series*, pages 60–69, Sept. 2011.

C.-Y. Ng, P. O. Slane, B. M. Gaensler, and J. P. Hughes. Deep Chandra Observation of the Pulsar Wind Nebula Powered by Pulsar PSR J1846-0258 in the Supernova Remnant Kes 75. *ApJ*, 686:508–519, Oct. 2008.

J. P. Ostriker and J. E. Gunn. On the Nature of Pulsars. I. Theory. *ApJ*, 157:1395, Sept. 1969.

F. Pacini. Rotating Neutron Stars, Pulsars and Supernova Remnants. *Nature*, 219: 145–146, 1968.

D. Parent, M. Kerr, P. R. den Hartog, et al. Observations of Energetic High Magnetic Field Pulsars with the Fermi Large Area Telescope. *ApJ*, 743:170, Dec. 2011.

A. Pellizzoni, M. Pilia, A. Possenti, et al. Discovery of New Gamma-Ray Pulsars with AGILE. *ApJL*, 695:L115–L119, Apr. 2009.

A. Pellizzoni, A. Trois, M. Tavani, et al. Detection of Gamma-Ray Emission from the Vela Pulsar Wind Nebula with AGILE. *Science*, 327:663, Feb. 2010.

M. Punch and H.E.S.S. Collaboration. The HESS project camera, tests, and status. In *International Cosmic Ray Conference*, volume 7 of *International Cosmic Ray Conference*, page 2814, Aug. 2001.

S. M. Ransom. Twenty Years of Searching for (and Finding) Globular Cluster Pulsars. In C. Bassa, Z. Wang, A. Cumming, and V. M. Kaspi, editors, *40 Years of Pulsars: Millisecond Pulsars, Magnetars and More*, volume 983 of *American Institute of Physics Conference Series*, pages 415–423, Feb. 2008.

P. S. Ray and P. M. S. Parkinson. Pulsar Results with the Fermi Large Area Telescope. In D. F. Torres & N. Rea, editor, *High-Energy Emission from Pulsars and their Systems*, page 37, 2011.

M. J. Rees and J. E. Gunn. The origin of the magnetic field and relativistic particles in the Crab Nebula. *MNRAS*, 167:1–12, Apr. 1974.

S. P. Reynolds. Supernova Remnants at High Energy. *ARA&A*, 46:89–126, Sept. 2008.

R. W. Romani. Gamma-Ray Pulsars: Radiation Processes in the Outer Magnetosphere. *ApJ*, 470:469, Oct. 1996.

R. W. Romani and K. P. Watters. Constraining Pulsar Magnetosphere Geometry with γ-ray Light Curves. *ApJ*, 714:810–824, May 2010.

M. Ruderman, J. Shaham, and M. Tavani. Accretion turnoff and rapid evaporation of very light secondaries in low-mass X-ray binaries. *ApJ*, 336:507–518, Jan. 1989.

M. A. Ruderman and P. G. Sutherland. Theory of pulsars - Polar caps, sparks, and coherent microwave radiation. *ApJ*, 196:51–72, Feb. 1975.

Y. Saito, N. Kawai, T. Kamae, S. Shibata, T. Dotani, and S. R. Kulkarni. Detection of Magnetospheric X-Ray Pulsation from Millisecond Pulsar PSR B1821-24. *ApJL*, 477: L37, Mar. 1997.

S. Schwanke and M. Fuessling. Confidence Intervals from the Rayleigh, Z_2^2 and Cosine Test. *H.E.S.S. internal note*, 2007.

I. I. Shapiro. Fourth Test of General Relativity. *Physical Review Letters*, 13:789–791, Dec. 1964.

I. S. Shklovskii. Possible Causes of the Secular Increase in Pulsar Periods. *Soviet Astronomy*, 13:562, Feb. 1970.

D. A. Smith. Review of the Solar Array Telescopes. *ArXiv Astrophysics e-prints, arXiv:astro-ph/0608251*, Aug. 2006.

D. H. Staelin and E. C. Reifenstein, III. Pulsating Radio Sources near the Crab Nebula. *Science*, 162:1481–1483, Dec. 1968.

I. H. Stairs. Pulsars in Binary Systems: Probing Binary Stellar Evolution and General Relativity. *Science*, 304:547–552, Apr. 2004.

E. M. Standish, Jr. Orientation of the JPL Ephemerides, DE200/LE200, to the dynamical equinox of J2000. *A&A*, 114:297–302, Oct. 1982.

S. J. Sturner, C. D. Dermer, and F. C. Michel. Magnetic Compton-induced pair cascade model for gamma-ray pulsars. *ApJ*, 445:736–755, June 1995.

Y. Su, Y. Chen, J. Yang, B.-C. Koo, X. Zhou, I.-G. Jeong, and C.-G. Zhang. Discovery of Molecular Shells Associated with Supernova Remnants. II. Kesteven 75. *ApJ*, 694: 376–386, Mar. 2009.

T. M. Tauris. Spin-Down of Radio Millisecond Pulsars at Genesis. *Science*, 335:561, Feb. 2012.

M. Tavani, G. Barbiellini, A. Argan, et al. The AGILE Mission. *A&A*, 502:995–1013, Aug. 2009.

T. Temim, P. Slane, R. G. Arendt, and E. Dwek. Infrared and X-Ray Spectroscopy of the Kes 75 Supernova Remnant Shell: Characterizing the Dust and Gas Properties. *ApJ*, 745:46, Jan. 2012.

R. Terrier, A. Djannati-Ataï, S. Hoppe, et al. H.E.S.S. Observations of the Young Composite SNR Kes 75. In F. A. Aharonian, W. Hofmann, & F. Rieger, editor, *American Institute of Physics Conference Series*, volume 1085 of *American Institute of Physics Conference Series*, pages 316–319, Dec. 2008.

D. J. Thompson. Gamma ray pulsars. In K. S. Cheng and G. E. Romero, editors, *Cosmic Gamma-Ray Sources*, volume 304 of *Astrophysics and Space Science Library*, page 149, Oct. 2004.

E. van der Swaluw. MHD interaction of pulsar wind nebulae with SNRs and with the ISM. *Adv. Space Res.*, 35:1123–1128, 2005.

E. van der Swaluw and Y. Wu. Inferring Initial Spin Periods for Neutron Stars in Composite Remnants. *ApJL*, 555:L49–L53, July 2001.

E. van der Swaluw, A. Achterberg, Y. A. Gallant, and G. Tóth. Pulsar wind nebulae in supernova remnants. Spherically symmetric hydrodynamical simulations. *A&A*, 380: 309–317, Dec. 2001.

E. van der Swaluw, T. P. Downes, and R. Keegan. An evolutionary model for pulsar-driven supernova remnants. A hydrodynamical model. *A&A*, 420:937–944, June 2004.

C. Venter. Millisecond Pulsars and Pulsar Wind Nebulae as Sources of Gamma Rays and Cosmic Rays. *Ph.D. Thesis, North-West University, Potchefstroom Campus*, 2008.

C. Venter and O. C. Jager. Spectral Constraints for Millisecond Pulsars Due to General Relativistic Frame Dragging. *Astrophys. Space Sci.*, 297:399–407, June 2005.

C. Venter, A. K. Harding, and L. Guillemot. Probing Millisecond Pulsar Emission Geometry Using Light Curves from the Fermi/Large Area Telescope. *ApJ*, 707:800–822, Dec. 2009.

J. P. W. Verbiest, M. Bailes, W. van Straten, et al. Precision Timing of PSR J0437-4715: An Accurate Pulsar Distance, a High Pulsar Mass, and a Limit on the Variation of Newton's Gravitational Constant. *ApJ*, 679:675–680, May 2008.

VERITAS Collaboration, E. Aliu, T. Arlen, et al. Detection of Pulsed Gamma Rays Above 100 GeV from the Crab Pulsar. *Science*, 334:69, Oct. 2011.

P. Vincent. H.E.S.S. Phase II. In *International Cosmic Ray Conference*, volume 5 of *International Cosmic Ray Conference*, page 163, 2005.

P. Vincent, J.-P. Denanca, J.-F. Huppert, and H.E.S.S. collaboration. Performance of the H.E.S.S. Cameras. In *International Cosmic Ray Conference*, volume 5 of *International Cosmic Ray Conference*, page 2887, July 2003.

F. Weber. Strange quark matter and compact stars. *Progress in Particle and Nuclear Physics*, 54:193–288, Mar. 2005.

T. C. Weekes. Very high energy gamma-ray astronomy. *Phys. Rep.*, 160:1–121, 1988.

D. M. Wei, K. S. Cheng, and T. Lu. Pulsed and Unpulsed Gamma-Ray Emission from Millisecond Pulsars. *ApJ*, 468:207, Sept. 1996.

E. d. O. Wilhelmi. Cherenkov telescopes results on pulsar wind nebulae and pulsars. In D. F. Torres and N. Rea, editors, *High-Energy Emission from Pulsars and their Systems*, Astrophysics and Space Science Proceedings, pages 435–452. Springer Berlin Heidelberg, 2011. ISBN 978-3-642-17251-9.

V. E. Zavlin. XMM-Newton Observations of Four Millisecond Pulsars. *ApJ*, 638:951–962, Feb. 2006.

V. E. Zavlin. Studying millisecond pulsars in X-rays. *Astrophys. Space Sci.*, 308:297–307, Apr. 2007.

V. E. Zavlin. Theory of Radiative Transfer in Neutron Star Atmospheres and Its Applications. In W. Becker, editor, *Astrophysics and Space Science Library*, volume 357 of *Astrophysics and Space Science Library*, page 181, 2009.

V. E. Zavlin, G. G. Pavlov, D. Sanwal, et al. X-Radiation from the Millisecond Pulsar J0437-4715. *ApJ*, 569:894–902, Apr. 2002.

L. Zhang and K. S. Cheng. X-ray and gamma-ray emission from millisecond pulsars. *A&A*, 398:639–646, Feb. 2003.

L. Zhang, J. Fang, and S. B. Chen. High-Energy Properties of Pulsed Emission from Millisecond Pulsars. *ApJ*, 666:1165–1173, Sept. 2007.

Danksagung

Ich danke meinem Doktorvater Prof. Dr. Thomas Lohse für die Möglichkeit zur Promotion am H.E.S.S. Experiment innerhalb der Berliner H.E.S.S.-Gruppe. Diese Arbeit hätte nicht ohne seinen lang anhaltenden Rückhalt entstehen können. Sein Wissen und Umgang mit Physik, Datenanalyse und Statistik waren für mich bei dieser Arbeit von unschätzbarem Wert und sind für mich Vorbild über diese Arbeit hinaus.

Darüberhinaus möchte ich mich bei den weiteren Mitgliedern der Prüfungskommission, dem Vorsitzenden Prof. Dr. Heiko Lacker und den Mitgliedern Dr. Alexander Kappes, Prof. Dr. Christopher van Eldik und Prof. Dr. Ulli Wolf, bedanken. Durch die Mitglieder dieser Kommission empfand ich das gesamte Verfahren der Verteidigung als sehr bereichernd.

Bei Dr. Christo Venter und Prof. Dr. Okkie de Jager möchte ich mich für die vielen Diskussionen und Erklärungen zu Pulsaren und deren Modellierung bedanken. Insbesondere möchte ich Christo meinen Dank dafür aussprechen, dass er seine Modellspektren für diese Arbeit zur Verfügung gestellt hat.

Viel Unterstützung habe ich in der Berliner H.E.S.S.-Gruppe erfahren, besonders jedoch von Dr. Ulli Schwanke. Seine Ratschläge waren bei der Konzeption und Bearbeitung der Fragestellungen dieser Arbeit wesentlich. Nicht zuletzt seine Geduld beim genauen Lesen und Kommentieren dieses Manuskriptes, vom allerersten bis zum allerletzten Tag des Entstehungsprozesses, haben mir sehr geholfen.

Bei Veronika Fetting möchte ich mich sehr für die Unterstützung bei meinem Weg durch Bürokratie und Organisation bedanken, vor allen Dingen jedoch für den immensen Rückhalt, den sie mir mit den richtigen Kommentaren zur richtigen Zeit ("Hol dicht die Großschot!") geboten hat.

Viele Leute haben meinen Weg in der Berliner Arbeitsgruppe begleitet und von jedem von ihnen habe ich eine Menge lernen und für meinen weiteren Weg mitnehmen können. Besonderen Dank gilt dabei Dr. Stefan Schlenker, Dr. Nukri Komin, Dr. Matthias Kerschhaggl, Dr. Matthew Dalton, Dr. Iurii Sushch, Manuel Paz Arribas und Olf Epler.

Bei Prof. Dr. Christian Stegmann möchte ich mich dafür bedanken, mein Interesse an der Betreuung und Weiterentwicklung des Datennahme- und zentralen Kontrollsystems von H.E.S.S. geweckt zu haben, für das ich während meiner Promotionszeit zunehmend verantwortungsvolle Aufgaben übernehmen durfte. Die Arbeit an einem so komplexen Aufgabengebiet ist interessant, aber auch überaus fordernd. Diese Arbeit wäre nicht möglich ohne die Unterstützung all der vielen Leute in der H.E.S.S. Kollaboration, die ihre Zeit und Arbeit dem laufenden Experiment zur Verfügung stellen. Ihnen gilt mein Dank ebenso wie den Leuten am Experiment in Namibia, Toni Hanke, Eben Tjingaete, Maveipi Kandjii und Albert Jahnke.

Allen Mitgliedern der H.E.S.S. Kollaboration und der Astroteilchenphysikgemeinde möchte ich für die spannende und herausfordernde Zeit danken, die ich mit ihnen verbringen durfte, oft an nicht minder spannenden Orten von Mérida bis Krakau. Dabei denke ich besonders an Dr. Svenja Carrigan, Dr. Karl Kosack, Dr. Rolf Bühler, Dr. Kathrin Egberts, Dr. Dominik Hauser, Dr. Stefan Ohm, Dr. Daniil Nekrassov, Heike Prokoph, Dr. Sebastian Böser und Dr. Stefan Klepser.

Zuletzt möchte ich all jenen in meiner engsten Umgebung danken, die meinen Weg während dieser Arbeit begleitet haben, und all jenen, die diesen Weg leider nicht mit mir bis zum Ende gehen konnten.